

Coupled 3D Dislocation Modeling at Nano- and Micro-Scales

THÈSE N° 7598 (2017)

PRÉSENTÉE LE 28 FÉVRIER 2017

À LA FACULTÉ DE L'ENVIRONNEMENT NATUREL, ARCHITECTURAL ET CONSTRUIT
LABORATOIRE DE SIMULATION EN MÉCANIQUE DES SOLIDES
PROGRAMME DOCTORAL EN MÉCANIQUE

ÉCOLE POLYTECHNIQUE FÉDÉRALE DE LAUSANNE

POUR L'OBTENTION DU GRADE DE DOCTEUR ÈS SCIENCES

PAR

Jaehyun CHO

acceptée sur proposition du jury:

Prof. D. Pioletti, président du jury
Prof. J.-F. Molinari, Dr G. Anciaux, directeurs de thèse
Prof. D. Rodney, rapporteur
Dr L. Pastewka, rapporteur
Prof. W. Curtin, rapporteur



ÉCOLE POLYTECHNIQUE
FÉDÉRALE DE LAUSANNE

Suisse
2017

Acknowledgements

In completing this thesis I have received help from many people over the past four and half years. I would not have been able to finish this thesis without their support and I would like to express my appreciations to them.

First of all I wish to thank my thesis supervisor, Professor Jean-François Molinari, Head of the Computational Solid Mechanics Laboratory EPFL. He has not only given me the opportunity to pursue my PhD study on a very interesting topic, but also provided me freedom to explore and research in my own way. His strong confidence and clear vision of my PhD research was one of the most important motivating factors for me.

I would also like to express my sincere gratitude to Dr. Guillaume Anciaux, my thesis co-advisor, for his patience and immense knowledge. With his deep understanding of mechanics and physics he provided valuable guidance for my PhD research. Furthermore, his guidance with respect to writing in English has helped me to considerably improve my scientific-paper writing skills.

I would particularly like to thank to Professor William Curtin for providing me a very interesting research environment. I was fortunate to be contacted by him when I was looking for a PhD position at EPFL. Furthermore, he has always encouraged me and provided me with invaluable advice and feedback.

My deep appreciation also goes out to all members of the lab LSMS. I really enjoyed my time in here thanks to the great atmosphere you provided. Especially, I would like thank Dr. Till Junge and Dr. Nicolas Richart. Their support and productive discussions regarding physics and computer skills helped me to finish my thesis. Furthermore, I also received a lot of help and tips about enjoying life in Lausanne!

During my PhD period I was financially supported by the Swiss National Science Foundation (grant No. 200021-140506/1). I am very thankful for this support and the opportunities provided to me.

A heartfelt thanks to the my band Kambé members Alex, Yohan, Frank and Kwihee. Our several rehearsals and concerts in various places in Europe truly refreshed my mind and emotions. I would particularly like to thank to the lovely couple Kwihee and Alex for their kindness and friendship.

A special thanks to my family and especially my parents, who have always believed and supported my enthusiasm, no matter what it was. I would like to also express appreciation to my sister living in Zürich. Her house has always been my small shelter whenever I have been homesick since arriving in Stuttgart in 2010. Finally, I want to thank my partner Dong-Eun

Acknowledgements

Kim for her countless support at every moment of my PhD. You are always in my heart.

February 13, 2017, Lausanne
Jaehyun Cho

Abstract

The performance of crystalline materials varies depending on the considered scale. To understand the size dependence of materials properties, the interaction and evolution of defects are essential. As such, the role played by dislocations is crucial for modeling metallic materials. In essence, a dislocation is a default in the crystalline periodicity that creates long-range stress fields, which makes the modeling of dislocation dynamics a challenging problem.

This thesis concentrates on the development of a novel multiscale method, which couples concurrently dislocation dynamics at nano- and micro-scales. A version of this method, the *Coupled Atomistic and Discrete Dislocations* (CADD), exists for two-dimensional problems. Its three-dimensional extension (CADD3d) is developed theoretically, and then implemented including the necessary parallel computing aspects. The proposed model requires two main building blocks, which are linked to general dislocation properties.

The first component is the correction field of the linear elasticity solution for dislocation cores. The core structures are pre-computed by modeling straight dislocations with arbitrary mixed angles using atomistic simulations. The obtained results are validated by extending the variational Peierls-Nabarro method. Finally, the templates including the core correction field are generated from the calculated core structures.

The second building block is the mobility law of dislocations. The dislocation mobilities for several orientations and temperatures are studied with atomistic simulations, and validated by comparisons to theoretical models. The mobility law is characterized by two damping mechanisms, the phonon viscosity and the phonon radiation effects.

CADD3d is then examined by studying several benchmark problems, which prove that the CADD3d method is a valid approach to couple atomistic and discrete dislocation dynamics including when multiple curved dislocations dynamics have to be considered.

Furthermore, to highlight the applicability of CADD3d for material plasticity problems, a Frank-Read source in an aluminum alloy is studied. The application result provides interesting insights on the mechanisms of solid-solution strengthening and grain-hardening effects at the nano and micro scales.

Key words: Computational Materials Science, Concurrent Multiscale Modeling, Plasticity, Size Effects, Dislocations, CADD, Molecular Dynamics, Discrete Dislocation Dynamics

Résumé

Les performances des matériaux cristallins varient en fonction de l'échelle considérée. Pour comprendre comment les propriétés des matériaux dépendent de la taille, l'étude de l'interaction et de l'évolution des défauts est essentielle. En tant que tel, le rôle joué par les dislocations est crucial pour la modélisation des matériaux métalliques. Une dislocation est un défaut dans la périodicité cristalline qui crée des champs de contraintes à longue portée, ce qui rend difficile la modélisation de la dynamique de dislocations un problème.

Cette thèse se concentre sur le développement d'une nouvelle modélisation numérique, qui associe simultanément les échelles nano et microscopique. Une version de cette méthode, *Coupled Atomistic and Discrete Dislocations* (CADD), existe pour des problèmes à deux dimensions. Une version en trois dimensions de la méthode CADD (CADD3d) est développée théoriquement, puis mise en œuvre, en incluant les aspects de calcul distribué nécessaires. Le modèle proposé nécessite deux constituants principaux, qui sont liés aux propriétés générales des dislocations.

La première composante est le champ de correction de la solution d'élasticité linéaire pour le cœur des dislocations. Les structures sont pré-calculées par la modélisation de dislocations droites avec des angles mixtes arbitraires en utilisant des simulations atomiques. Les résultats obtenus sont validés par l'extension de la méthode variationnelle Peierls-Nabarro. Enfin, des modèles comprenant le champ de correction des cœurs de dislocation sont construits à partir du calcul de cœur structures.

Le deuxième bloc de construction est la loi de mobilité des dislocations. Les mobilités de dislocations avec plusieurs orientations et températures sont étudiées avec des simulations atomiques, et validées par comparaisons avec des modèles théoriques. La loi de mobilité se caractérise par deux effets d'amortissement : la viscosité des phonons et la radiation des phonons.

La méthode CADD3d est ensuite examinée en étudiant plusieurs problèmes de référence, qui prouvent qu'il s'agit d'une approche valable pour coupler des simulations de dynamiques de dislocation atomiques et discrètes, y compris lorsque plusieurs dislocations courbes doivent être considérées.

En outre, pour mettre en évidence l'applicabilité de CADD3d pour des problèmes de plasticité, des sources Frank-Read dans un alliage d'aluminium sont étudiées. Les résultats d'application fournissent des indications intéressantes sur les mécanismes de renforcement de la solution solide et des effets de durcissement des grains aux échelles nano et microscopique.

Acknowledgements

Mots clefs : science computationnelle des matériaux, modélisation concurrente multi-échelles, plasticité, effets de taille, dislocations, CADD, dynamique moléculaire, dynamique de dislocation discrète

Contents

Acknowledgements	i
Abstract	iii
Résumé	v
List of figures	xi
List of tables	xix
1 Introduction	1
1.1 Multiscale Modeling of Materials Strength	1
1.2 Organization of Thesis	4
2 Experimental Studies on Size Effects	7
2.1 Crystal Structure	7
2.2 Size dependent strengths	10
2.2.1 Geometrically-Necessary-Dislocations	10
2.2.2 Dislocation Starvation	11
2.2.3 Intrinsic Material Structures	12
3 Computer Simulation Methods employed to study Size Effects	15
3.1 Finite Element Analysis	15
3.1.1 Strain-Gradient Plasticity	17
3.1.2 Stress-Gradient Plasticity	18
3.2 Discrete Dislocation Dynamics (DDD)	19
3.2.1 2d DDD	20
3.2.2 3d DDD	21
3.3 Classical Molecular Dynamics	23
3.4 Coupling Atomistic to Continuum Methods	25
3.5 Coupled Atomistic and Discrete Dislocation Method in 2d (CADD2d)	26
4 Coupled Atomistic and Discrete Dislocation Method in 3d (CADD3d)	29
4.1 Differences between CADD2d and CADD3d	29
4.1.1 Infinite Straight Dislocations	29

Contents

4.1.2	Hybrid Dislocations	30
4.2	CADD3d	31
4.2.1	Coupling Engine	32
4.2.2	Coupling Algorithm	33
4.2.3	Coupling Procedure	33
5	Dislocation Core Structures, Peierls Stresses and Core Templates with Several Character Angles in Aluminum	39
5.1	Core templates	40
5.2	Atomistic Dislocation Modeling	41
5.3	Method: Variational Peierls -Nabarro Method	45
5.4	Results and Discussion: Comparison between the MD and PN Models Core Structures	50
5.5	Peierls Stresses	51
5.6	Generation of Core Templates	56
5.7	Summary	58
6	Mobility law of dislocations in Aluminum	59
6.1	Atomic dislocation modeling	60
6.2	Eshelby-Olmsted approach	63
6.3	Discussion: critical velocity	66
6.4	Implementation of mobility law	68
6.5	Summary	70
7	Validation of CADD3d: Hybrid Dislocations	71
7.1	Hybrid Straight Dislocations	71
7.1.1	Displacements of Pad Atoms	73
7.1.2	Results	74
7.1.3	Sensitiveness of the Coupling Parameters	76
7.2	Hybrid Dislocation Loops	78
7.2.1	Additional Features of CADD3d for Curved Dislocations	79
7.2.2	Results	80
7.3	Interactions between Multiple Dislocations	82
7.4	Contraction of hybrid dislocation loop	83
7.5	Summary	83
8	Frank-Read Source Dynamics in Al and Al-5%Mg	87
8.1	Frank-Read source in crystalline materials	87
8.2	A Double Frank-Read Source in CADD3d	88
8.3	Core Templates, Peierls Stress and Mobility Law of Dislocations in Al and Al-5%Mg	90
8.4	Definition of Pad Domain	92
8.5	Dislocation Coarsening	95
8.6	Dislocation Nucleation from Frank-Read Source	96

8.7 Strain Hardening Effects with Frank-Read Source	97
8.7.1 A Frank-Read Source in Al-5%Mg Alloy	97
8.7.2 Hardening Effects	100
8.7.3 Coupling Performances	101
8.8 Summary	102
9 Concluding Remarks and Outlook	103
9.1 Summary	103
9.2 Outlook	105
9.3 Final Remark	106
Bibliography	121
Curriculum Vitae	123

List of Figures

1.1	Stress-strain curves obtained from tension testing with submicro-sized gold specimens. Figure from [Kim and Greer (2009)]	2
1.2	Schematic of defect configurations for several of length and time scales. Figure from [Roters et al. (2010)]	3
2.1	(a) Schematic of a crystalline structure including multiple grains and defects. The gray region depicts the grain boundaries. (b) A Burgers circuit enclosing the dislocation. (c) The same Burgers circuit in a perfect reference lattice. The special vector needed for closing the circuit is the Burgers vector \vec{b}	8
2.2	Three dimensional views of an edge (a) and a screw (b) dislocations. The Burgers vectors \vec{b} are described with the red arrows, and the dislocation line directions $\vec{\xi}$ are depicted with the blue arrows.	9
2.3	Sequences of slip by movement of an edge dislocation under an external shear load $\bar{\sigma}$. Shift of the upper half of the crystal is emerged after the edge-dislocation traveling.	10
2.4	The indentation size effect and the density of geometrically necessary dislocations (GNDs). (a) An experimental observation of a specimen with four indents. (b) The distribution of the GNDs density below and around indents. Figures from [Zaafarani et al. (2006)]	11
2.5	(a) A compression test of a nano-sized pillar. (b) Strain-stress curves with different pillar sizes. The strength increases with decreasing of the specimen size. These figures are taken from [Greer and Hosson (2011)].	12
2.6	(a) Schematic of a pileup of edge dislocations against a grain boundary. (b) An experimental observation of piled-up mixed dislocations in a titanium alloy. Figure from [Britton et al. (2015)]	13
3.1	Dislocations are emitted from a source ($x = 0$), and are piled-up against obstacles ($\pm L_{obs}/2$) under a shear stress σ_{app} . Figure from [Chakravarthy and Curtin (2011)].	19
3.2	Schematic of a single crystal system including multiple slip systems and dislocations. Figure from [Van der Giessen and Needleman (1995)].	20

List of Figures

3.3	(a) A snapshot of discrete dislocation dynamics simulation with a BCC metal of $10 \mu m^3$. Dislocations are colored by the Burgers vectors. Figure from [Arsenlis et al. (2007)]. (b) A dislocation network is composed of a set of nodes (empty circles) interconnected by straight lines. Figure from [Bulatov and Cai (2006)].	22
3.4	(a) A perspective view of a MD system including an edge dislocation. Only the atoms below the slip plane are depicted, and are colored by the Y coordinate. Figure from [Cho et al. (2015)]. (b) The dislocation structure in the top view of the slip plane. The misfit stacking-fault sequence represents the edge dislocation structure in a FCC crystalline material. Figure from [Cho et al. (2015)]. (c) A snapshot of dislocation nucleation process during a nano-scratch simulation. Figure from [Junge (2014)]	24
3.5	An indentation study with CADD2d. (a) A close-up view at the indented surface in the MD domain. (b) A view of the complete CADD2d domain. Multiple dislocations nucleated under the indenter in MD are successfully transferred into DDD. Figures from [Miller et al. (2004)].	27
4.1	The procedure of the detection/passing scheme of CADD2d. (a) An infinite straight dislocation approaches the DDD domain. The non-linear core region is shown as the grey circular area. This dislocation can be detected in the detection zone near the interface. (b) A repulsive spurious force applies on the MD dislocation because the DDD mesh cannot sustain the highly distorted core structure. (c) A successful dislocation passing from MD to DDD. This is done by introducing a DDD dislocation after the MD dislocation detection. The MD dislocation can disappear at the interface by adding the displacement field of a dislocation with the opposite sign.	30
4.2	CADD3d-domain decomposition. The MD region contains a dislocation source, while the remaining region is handled with DDD. Several dislocations are plotted. There is one dislocation loop which is partly in the MD domain and partly in the DDD zone. Such dislocation is the so-called <i>hybrid dislocation</i>	31
4.3	Three simulation engines are plugged-in LibMultiScale, which is currently being maintained and developed in house [Anciaux et al. (2006); LibMultiScale (2006)]. For the molecular dynamics domain, Lammmps, developed by Sandia national laboratory, is chosen [Plimpton (1995); Lammmps (1995)]. The plug-in for the discrete dislocation dynamics domain is ParaDiS, which is maintained by Lawrence Livermore national laboratory [Arsenlis et al. (2007); ParaDiS (2007)]. The last plug-in Akantu is chosen to describe the finite element domain, and is maintained in house [Richart et al. (2010); Akantu (2007)].	32

4.4	Algorithm of the CADD3d method. MD and DDD processors are shown with the red and blue solid lines, respectively, and their implementation components are surrounded by the orange and the dark-blue dashed lines, respectively. The components of the CADD3d implementation are placed inside the cyan dashed-dot-lines. Each of them are run on processor subsets handling either MD or DDD. The components running on the different processors communicate with each other through the two steps labeled <i>Coupling-Communication 1</i> and <i>Coupling-Communication 2</i>	34
4.5	Hybrid straight dislocation dynamics with the update of the reciprocal boundary conditions. (a) At an initial stage, the MD and DDD boundary conditions are consistent with each other. (b) By applying a shear load, the two dislocation sub-parts move, which lead to mismatched boundary conditions. The update of the reciprocal boundary conditions consists of the two steps: (c) update of the slaved DDD nodes and (d) update of the pad atoms.	35
4.6	A straight hybrid dislocation approaches the DDD domain. (a) The hybrid dislocation moves forward, and needs to update the boundary conditions of MD and DDD. (b) The reciprocal boundary conditions are updated. The MD sub-part will be completely impeded by the pad atoms in front. (c) To migrate the hybrid dislocation to DDD, new DDD nodes are introduced at the cores in the insertion (MD+DDD) zone. (d) The dislocation escapes the MD domain, and the MD dislocation leaves a step at the outer-surface of the pad region.	37
5.1	Schematic of a dislocation core in the pad. For most of the pad, the linear elasticity displacement solution \vec{u}_e is adequate. However, in the vicinity of the dislocation line (non-linear core region), it is necessary to add the correction field $\Delta\vec{u}_c$ obtained from the core template to minimize spurious forces.	40
5.2	(a) Schematic modeling of a straight dislocation with an arbitrary character angle. (b) Top view of the slip plane. Lattice coordinate in y axis is $[111]$, while the coordinates of x and z axes vary with the character angle θ as shown in Table 5.1.	41
5.3	(a) Procedure to find lattice coordinates for a mixed dislocation based on the atomistic representation used for edge dislocation ($x = [11\bar{2}]$, $y = [111]$ and $z = [1\bar{1}0]$). (b) Result of the procedure ($x'[\bar{1}5\bar{4}]$, $y = [111]$ and $z' = [3\bar{1}\bar{2}]$). The 49.107° mixed dislocation can be created by choosing x' as the dislocation line direction. The full black circles are the minimal number of atoms under the given coordinate system, and empty black circles are the result of replications.	42
5.4	Deformation of the simulation box after imposing the Volterra fields. (a) front view and (b) top view. The initial configuration is denoted by the gray dot lines, and the box after inserting the dislocation is described with the black solid lines. The dashed black lines in (b) are the boundary of the bottom side in the y direction.	44

List of Figures

5.5	Atomistic structure of the edge (90°) and mixed (49.107°) dislocation in FCC Al. (a) compact core structures after imposing the Volterra field / before the relaxation. (b) core structures after relaxations. The atoms are colored by coordinates of the y axis. Red, yellow, cyan, and blue atoms are placed on top, 2nd, 3rd and 4th layers in the y axis from the slip plane. The initial compact dislocation lines dissociate into two Shockley partial dislocation lines indicated by the black arrows.	46
5.6	(a) Periodic γ -surface in the x and z directions of the Mendeleev et al. EAM potential [Mendeleev et al. (2008)]. (b) GSF energy curves in $\langle 112 \rangle$ direction of several Al EAM potentials [Angelo et al. (1995); Voter and Chen (1987); Oh and Johnson (1988); Mishin et al. (1999)] and DFT computations Hartford et al. (1998) (figure was taken with agreement of copyright by author [Zimmerman et al. (2000); Ercolessi and Adams (1994)] and IOP publishing). The blue curve shows results obtained with the Mendeleev et al. potential [Mendeleev et al. (2008)]. We reproduce one of author's results shown by the red curve with Mishin and Farkas potential [Mishin et al. (1999)].	49
5.7	The displacements u_z (edge direction), u_x (screw direction) over the z coordinate (normalized by Burgers vector length) obtained from MD and PN methods for different character angles (some MD atoms are excluded for better visibility).	50
5.8	Comparison between MD with PN results with atomistic representation on the slip plane (49.107° mixed dislocation).	51
5.9	The strains (du_z/dz and du_x/dz) along z axis (normalized by Burgers vector length) measured by MD and PN for the representative eight angles.	52
5.10	Variation of stacking fault widths for the eight angles.	52
5.11	(a) Dislocation displacements and (b) energy variations with respect to top surface displacement of the edge (90°) and mixed (40.893°) dislocation.	54
5.12	Variation of Peierls stresses for several angles with respect to the density of atoms in the gliding direction. The corresponding Peierls stress value and the character angle are denoted next to each marker.	55
5.13	The differences between the atomistic displacements and the linear elasticity displacements around the dislocation cores (0, 0) for the eight character angles.	56
5.14	Computation procedure of the core template of the edge 90° dislocation. (a) Atoms around dislocation core. (b) The projected atoms on the y - z plane. (c) Two dimensional mesh, the so-called core template, based on the projected atoms.	57
6.1	Schematic modeling of a straight dislocation with an arbitrary character angle θ . The length of the simulation box along y axis is $\sim 200\text{\AA}$, while the dimensions along x and z axes vary around 70\AA and 350\AA , respectively, with the lattice orientations determined by the character angle θ [Cho et al. (2015)]. A finite temperature is imposed by Langevin thermostats and a shear stress is applied on the free surfaces in the direction of the Burgers vector $\vec{b} = \frac{1}{2}[1\bar{1}0]$.	60

6.2	(a) Evolution of temperatures at the vicinity of the slip plane of the edge dislocation with various shear stresses. The target temperature is 100K. (b) Velocity of dislocations (49.107° and 90°) at 100K and 300K under 300MPa. (c) Variations of effective stresses around the slip plane during edge dislocation motion. (d) Differences between the applied and effective stresses as function of the dislocation velocity. (e) Variations of steady-state velocities for 49.107° and 90° dislocations as a function of shear force at 100K and 300K.	62
6.3	Dislocation mobility for the various character angles and temperatures. The MD results are described by the markers and the fits using Equation 6.2 are depicted by the solid lines. For the 100K, 200K and 300K cases, the simulations and fits are denoted with the red, blue and green colors. The critical velocities v_0 are notified by the black-dashed lines.	65
6.4	(a) Variation of the damping parameter A multiplied by the magnitude of Burgers vector $ \vec{b} $ for the various character angles. (b) Variations of damping constant D with respect to character angle. The constants for 100K, 200K and 300K cases are represented by red circles, blue squares and green triangles, respectively. (c) The fitted critical velocity v_0 and the minimum phase velocity v_p^{min} in the dislocation propagation direction of the various character angles.	66
6.5	Dispersion curves in the propagation direction of screw 0° , mixed 40.893° and edge 90° dislocations. Three phonon branches exist for each wave number k . For each angle, the minimum phase velocity v_p^{min} corresponds to the slope of the black dashed line.	67
6.6	Schematic modeling of a dislocation loop in a discrete dislocation simulation. Infinite boundary conditions are employed in all directions. A constant shear stress $\sigma_{yz} = 700\text{MPa}$ activates the dislocation loop expansion.	69
6.7	Snapshots of dislocation loop dynamics at 0, 2.5, 5 and 10ps with three different dislocation mobility laws: (a) A linear relation (A_{90} and A_0) between dislocation velocity and shear loading is considered and interpolated linearly from edge (90°) to screw (0°) angles. (b) The linear and supersonic asymptotic regimes are considered by considering the mobility parameters A_{90} , D_{90} and A_0 , D_0 for edge (90°) and screw (0°) dislocations. Intermediate angles are interpolated linearly from edge to screw. (c) The new mobility law proposed, which accounts for the linear and supersonic regimes and a total of 8-mixed angles.	70
7.1	(a) A schematic modeling of a hybrid straight dislocation. At the center of the domain, a MD system is introduced. A DDD domain is used in the remaining region. A periodic boundary condition is applied in the x direction, while infinite boundary conditions are employed in the other directions. (b) The hybrid dislocation from a top view of the slip plane. The two dislocation subparts are coupled by imposing the reciprocal boundary conditions with the pad atoms and the two constrained DDD nodes.	72

List of Figures

- 7.2 The external boundary of the DDD nodes are closed by the two fictitious nodes shown with the cross markers. The internal boundary regions of the two hybrid straight dislocations are connected by (a) a straight line between the two slaved DDD nodes and (b) the result of the MD dislocation detection. 74
- 7.3 Evolutions of (a) the displacement and (b) the velocity of the hybrid dislocations with the selected eight character angles and the two shear stresses (100MPa and 500MPa). The results of the MD sub-part of the hybrid dislocations are represented by the (red and blue) circle-lines, and the (orange and cyan) dashed lines represent the results of the DDD sub-part of the hybrid dislocations. . . . 75
- 7.4 (a) Snapshots of the dynamics of a mixed 30° hybrid dislocation with 100MPa in a perspective view (reference case). Only the atoms around the bottom slip plane are shown, and are colored by the magnitude of the displacement. The DDD nodal points are shown as big spheres. (b) Top view of the slip plane shown in (a) where the DDD nodes and the atoms violating centro-symmetry are plotted. (c) Simulation result obtained with $B_\theta = \frac{1}{2}B_\theta$. (d) Simulation result obtained with a small cut-off radius $r_c = |\vec{b}|$. for the core correction. This leads to smaller stacking fault widths as can be observed near the coupling interface. 77
- 7.5 Sensitiveness studies of the coupling scheme with the five different simulation settings (change of core template cut-off radius r_c , of the damping parameter B_θ , of the effective mass m and of the update step t_{update}). The dislocation displacements are shown as functions of time. These results can be compared to the reference results denoted by the red circle-line and the black dashed line. . . 77
- 7.6 (a) A schematic modeling of a hybrid dislocation loop in a perspective view. Infinite boundary conditions are applied in all directions. (b) The hybrid dislocation is shown from a top view of the slip plane. 78
- 7.7 (a) Application of multiple core templates within the pad zone. The pad region is decomposed to match each DDD segment. Based on this decomposition, the core templates with three different angles (θ_1 , θ_2 and θ_3) are applied on the red, blue and orange colored atoms, respectively. (b) Two strategies to close the loop between the two constrained DDD end nodes of the hybrid dislocation loop. The first strategy is to connect the two nodes by using a straight line as shown by the blue dashed line. The second strategy is to connect them by employing a discrete line consisting of the MD dislocation cores. 79

7.8	Comparison of the hybrid dislocation loop motions at 0ps, 1ps, 4.5ps and 5.5ps. The DDD nodes are represented by the red circle markers, and the atomistic dislocations are described by the small circles. (a) Snapshots of the simulation with a straight line-connection strategy are shown in a perspective view. Only the atoms around the slip plane and the DDD nodes are shown. The colors applied on the atoms represent the displacement magnitude in the Burgers vector direction (z). (b) The same simulation (a) from a top view of the slip plane. Only the atoms violating centro-symmetry and the DDD nodes are shown. (b) Simulation with the discrete line consisting of the MD dislocation detection solution between the two constrained node. (c) Simulation with the hybrid dislocation loop and the two fixed DDD networks.	81
7.9	A schematic modeling of a hybrid dislocation loop and two fixed dislocation loops. The Burgers vectors of these loops are same.	82
7.10	Displacement and velocity evolutions of the dislocation loops with the three different simulation setting. The first two problems are the hybrid dislocation loops with the two different connection strategies. The third problem is the hybrid dislocation loop with the two fixed DDD networks.	83
7.11	Contraction of the hybrid dislocation loop. As the loop contracts, the curvature increases, and the spacing between the two core templates reduces.	84
7.12	Displacement evolution of the MD and DDD parts of the dislocation loop. As the loop contracts, the difference in behavior between the two sub-parts of the loop increases with time.	84
8.1	(a) Configuration of a Frank-Read source composing to two sessile dislocations A and B. The segment between A and B is a dislocation on the glide plane. (b) A nucleation process of a dislocation loop from the Frank-Read source.	88
8.2	An experimental observation of a Frank-Read source and nucleated dislocation loops in an Al-Mg alloy. Figure from [Amelinckx (1964)].	89
8.3	(a) A double Frank-Read source modeling in the CADD3d domain in a perspective view. The MD domain boundary is shown with the red solid lines, and the DDD boundary is indicated in the blue solid lines. The atomistic FR source consists of the two planar dislocations connected with the two sessile dislocations. 5% of the MD atoms are defined as the Mg substitution. (b) At each end of the planar dislocations, a cylindrical void is created to prevent gliding motions of the sessile dislocations.	89
8.4	The strains du_z/dz (edge direction), du_x/dz (screw direction) over the gliding direction z . The results derived from the aluminum are shown with the red and blue solid lines, and the calculations obtained from the homogenized alloy are indicated in the green and orange solid lines.	91
8.5	Variations of Peierls stresses for several character angles in Al and Al-5%Mg with respect to the density of atoms in the gliding direction. The corresponding Peierls stress value and the character angle are denoted next to each marker. . .	92

List of Figures

8.6	Dislocation mobilities of several character angles in Al and Al-5%Mg. The aluminum results are depicted in the red circle-lines, and the alloy outcomes are shown with the blue lines. Continuous lines are fitted using the Eshelby-Olmsted equation.	93
8.7	Schematic of the evolution of the MD box during the evolution of a single Frank-Read source. (a) The MD and DDD domains are shown from a top view of the slip plane. The two DDD dislocation loops (blue circles) have been emitted previously from the FR source (orange line) in the MD region. (b) Front view of the MD domain. The step is due to the two dislocation loops that previously crossed the interface. (c) The FR source displaced sufficiently to contact the pad atoms. (d) The atom re-insertion scheme action during the FR source evolution. (e) Re-definition of the MD box to center the FR source. (f) Continuous FR evolution as the result of the (d) re-insertion and (e) re-definition schemes in CADD3d.	94
8.8	Simplification of the DDD dislocation network. (a) The original dislocation loop. (b) Segments within low curvature regions merged into longer straight segments.	95
8.9	Modeling of a single Frank-Read source with (a) MD and (b) DDD.	96
8.10	Snapshots of the simulations at 5ps, 10ps, 17.5ps, 20ps, 25.5ps and 50ps. The MD and DDD domain boundaries are shown with the red and blue solid lines, respectively. The MD atoms are depicted by the small red spheres, and the DDD nodes are plotted by the large blue spheres. (a) and (b): single scale MD and DDD simulations, respectively. (c) and (d): the CADD3d coupling simulations with the two different MD-box sizes.	98
8.11	(a) Multiple dislocation loops nucleated from the atomistic FR source are shown with a perspective view. The MD box (red line) is located in the middle and the DDD boundary ($0.5\mu\text{m}$) is shown with the blue lines. (b) A zoom of the MD domain. The MD atoms and DDD nodes are colored by their Y coordinates. The magnesium atoms are shown with small and transparent gray spheres.	99
8.12	Variations of numbers of the nucleated dislocation loops with different grain sizes and the material types. (a) Grain hardening effect: small grains yield fewer dislocation loops. (b) Solid solution hardening effect: the alloy emits less dislocation loops than for the aluminum.	100
8.13	Evolution of a total number of the DDD nodes is shown by the blue circles. The considered DDD points after the coarsening strategy for the coupling is shown with the red circles. In this example, the coarsening strategy reduces the number of the DDD points considered by 88% at most.	101
9.1	Modeling of a double Frank-Read source with multiple MD sub-domains in CADD3d.	106

List of Tables

- 5.1 Selected eight angles, lattice coordinates, number of replicas and atoms of each simulation box. 43
- 8.1 Comparison between the full MD and CADD3d performances for the pre-validation problem given in Section 8.6. We only compare the degrees of freedom employed in the MD domains are compared between the full MD and CADD3d simulations. For CADD3d, the averaged CPU time includes all the calculation times (for MD, DDD and CADD3d coupling). 102

1 Introduction

Multiscale Modeling of Materials Strength

By increasing the performance (e.g. strength and ductility) of metals, more durable metallic products can be obtained. High performance materials can be effectively designed, and the developments of material-design techniques consequently permit applications for a high quality of life, for instance in the domain of security and environment. During the last decades, material-design techniques have been developed. Specifically, those techniques focus on designing the composition of materials, and such a designing process starts from the characterization of material performances, for which several measurement methodologies exist. The most popular analysis is the tensile testing [Banabic (2000)]: a strip or cylinder specimen is anchored at one end and subjected to an axial load at the other end. Several mechanical properties are directly measured such as Young's modulus and yield strength. These mechanical parameters allow to select a material for a given application device.

The development of methods for the production of miniaturized mechanical devices allows a wide range of new applications for transportation and communication systems: Micro- and Nano-Electro-Mechanical Systems (MEMS and NEMS). In NEMS and MEMS, it is possible to assemble complex shapes, such as levers, gears and pinwheels. At these small scales, the loading conditions can be extreme. For instance, a cantilever acceleration sensor, which is used as automotive airbag actuator, can experience severe stresses caused by a traffic accident. Therefore, designing materials for such small-scales applications should be considered carefully. However, the mechanical properties at these scales are poorly understood if compared to the mainstream knowledge of meter-scale metallic objects. Thus, controlling the stability of so small systems becomes extremely difficult.

One of the striking findings with nano- and micro-sized specimens is the size dependent performance of materials. Specifically, as the intrinsic (i.e. micro-structural) or extrinsic (i.e. sample size) length of the specimen decreases, the material strength increases [Wang et al. (2006); Nix and Gao (1998); Greer et al. (2008); Gao et al. (1999)]. Those experimental observations lead to the famous adage: *smaller is stronger* [Wang et al. (2006)]. As an example,

Chapter 1. Introduction

Figure 1.1 shows the measured tensile stresses for different specimen sizes at the submicron-scale [Kim and Greer (2009)]. We observe an increase of the tensile strength with the decrease of the specimen size. The main reason behind such a size-dependent behavior is that, at the

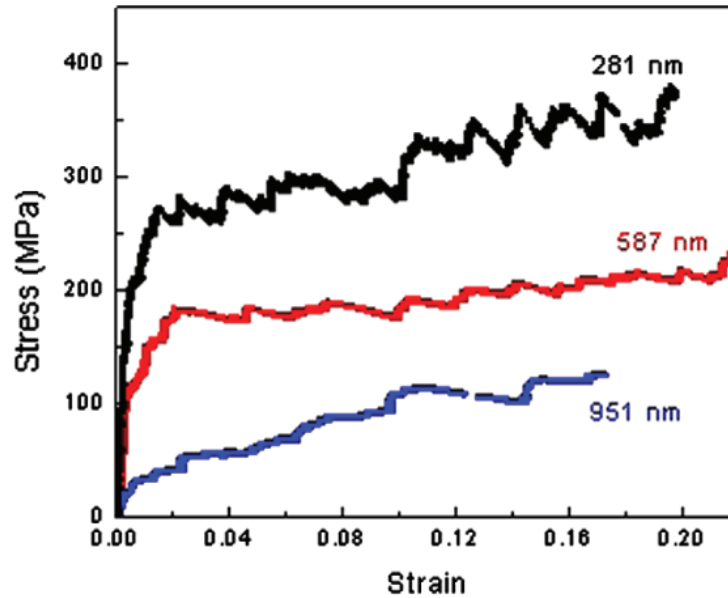


Figure 1.1 – Stress-strain curves obtained from tension testing with submicro-sized gold specimens. Figure from [Kim and Greer (2009)]

small scales (from nanometer to micrometer), plastic deformations are strongly governed by crystalline structures and defect dynamics. Accordingly, to characterize the mechanical behaviors of small specimens, it is required to consider crystalline defects and their movements. Various defects exist, and these defects can be categorized by their spatial dimensions. For example, voids, dislocations and grain boundaries can be represented as zero, one and two dimensional defects, respectively. They show very different behaviors, and they are all interacting with each other [Hirth and Lothe (1992); Hull and Bacon (2011); Hall (1951)].

There are many experimental observations of the size effects, and several theoretical models have been proposed to describe defect dynamics. These models can be employed in material-design processes to predict material behaviors. Conventionally, creating new materials rely on a trial-and-error approach with a wide range of parameters. The number of these parameters can be reduced by predicting material performance from theoretical models. In general, the employed models are based on partial differential equations (PDEs), and their solution can be evaluated by means of iterative methods. However, the solution of a PDEs with a complex geometry is difficult to find in general. Classically, complex geometries are subdivided into simpler parts, and the associated set of PDEs is assembled and solved. Because such discretizations yield a large number of degrees of freedom, computational resources have to be employed to find a solution. This methodology is the *computational modeling of materials*.

1.1. Multiscale Modeling of Materials Strength

Figure 1.2 presents different defects observable at several length and time scales [Roters et al. (2010)]. Depending on the scale, the defects can be described differently. This is clearly

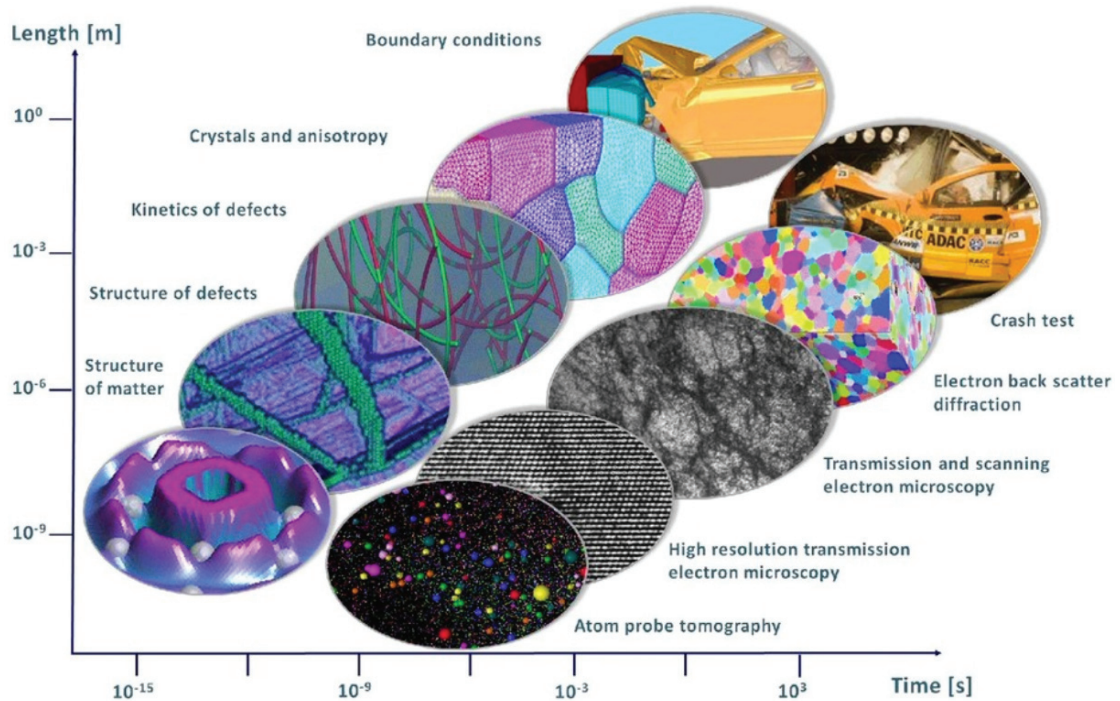


Figure 1.2 – Schematic of defect configurations for several of length and time scales. Figure from [Roters et al. (2010)]

illustrated by Figure 1.2, where we can see that at the nano-meter scale (10^{-9} m) a material is described by a set of atoms whereas at the macroscopic scale a continuum representation is usually preferred. Such differences lead to theories as well as computer simulation methods often restricted to a single scale and specialized for specific defect types. This is a major limitation of computer simulations for material modeling.

In fact, experimental observations of defect behaviors cannot be scale separated in general. Accordingly, the information obtained from experiments cannot be compared directly to simulation results. To palliate this issue, the computational modeling techniques should consider different scales within a single framework. This is called a "multiscale" approach which allows to obtain material behaviors including fundamental physics at several scales. The difficulty lies in the difference between the employed physical models, making their connection a tedious process that should be considered carefully. Depending on the types of inter-relation, such multiscale methods can be divided into two groups: indirect and direct multiscale methods.

In an indirect multiscale model, the coupling is considered sequentially. More precisely, several material parameters can be evaluated at the small/fine scales. These values are then used as input parameters for larger scale models [Haghighat et al. (2011); Segurado and

Lorca (2010); Wang and Beyerlein (2011); Martínez et al. (2008)]. For example, void formation energies can be precisely measured by ab-initio calculations (10^{-9}m), and can be used as the critical energy to introduce new vacancies in a higher scale model. The indirect approach is simple and accurate if only a weak/localized relation exists between the coupled models. On the other hand, a direct multiscale model concurrently couples the different scale models. For instance, this is crucial when various defects are strongly interacting with each other over large distances/scales [Shilkrot et al. (2004); Shiari et al. (2005); Zhang et al. (2013)]. Because any direct multiscale method requires to treat distinct theoretical models simultaneously, it is generally more complicated than the indirect methods.

According to several experimental observations [Greer and Hosson (2011); Arzt (1998)], the behavior of defects, which is important to understand the size effects, is strongly coupled between the nano- and micro-scales (from 10^{-9}m to 10^{-6}m). One of the famous experimental observations showing such fully conjugated behaviors is the grain boundary strengthening, and it can be explained as follows: dislocations can be generated in a grain from several nucleation sources, and these dislocations are trapped by the grain boundary. The tangled dislocations create stresses inside the grain which may prevent further nucleation. Consequently, having smaller grains limits the plastic flow and increases the yield strengths. In fact, the nucleation process is a local and atomistic phenomenon, while the long-range interactions between the trapped dislocations and the nucleation sources occur beyond the micro-scale. To the best of my knowledge, there is no satisfactory multiscale method directly coupling the defects at these two scales.

In this thesis, a new concurrent multiscale methodology and its computer simulation method for 3d dislocation dynamics will be developed and implemented. This thesis focuses mainly on two of the necessary building components, which will be constructed by studying general dislocation properties. With such constructed components, the multiscale methodology will be validated and calibrated through several benchmark problems in cases where a constant shear stress is imposed. Finally, a size effect due to the dislocation evolution occurring at atomistic- and micro-scales will be studied with the proposed multiscale method.

Organization of Thesis

This thesis mostly focuses on dislocations in FCC crystalline materials among the other types of defects and materials. Within this scope, this thesis is organized as follows.

Chapter 2 - *Experimental Studies on Size Effects* - presents several experiments demonstrating size dependent performances. For each experimental observation, the main mechanism, which is related to dislocation dynamics, will be discussed. Moreover, the theories proposed to describe such experimental observations will be briefly introduced.

Then, Chapter 3 - *Computer Simulation Methods employed to study Size Effects* - reviews the computer simulation methods useful to study size effects. The main methods (finite-

element method, discrete dislocation dynamics and molecular dynamics) as well as multiscale methods are briefly presented. Their capabilities and limitations for describing size effects are included. This part greatly motivates the development of the new 3d dislocation dynamics multiscale method developed during my Ph.D work.

Chapter 4 - *Coupled Atomistic and Discrete Dislocation Method in 3d (CADD3d)* - describes the new 3d multiscale model. The main development challenge will be stated while highlighting the needed innovations if compared to the existing 2d multiscale model. Then, the coupling strategies and the detailed description of the implementation (code architecture) will be discussed.

Two of the principal components of CADD3d are presented in the following two chapters (Chapter 5 - *Dislocation Core Structures, Peierls Stresses and Core Templates with Several Character Angles in Aluminum* - and Chapter 6 - *Mobility law of dislocations in Aluminum*). A detailed description of their inclusion into the CADD3d framework will be provided. Furthermore, these components based on atomistic calculations, which will be validated thanks to other theoretical models.

In Chapter 7 - *Validation of CADD3d: Hybrid Dislocations*, several 3d dislocation dynamic simulations will be made with CADD3d in order to validate the coupling methodology. The first test problem is a hybrid straight dislocation, made partly with atoms and partly with discrete dislocation dynamics segments. The analysis of the results will allow us to evaluate the sensitiveness of the coupling components of CADD3d. The second problem considers the expansion of an hybrid dislocation loop due to homogeneous shear loading. For the third test problem, CADD3d is put to the test for when a large number of dislocations are interacting. Lastly, the evolution of a hybrid dislocation loop under a small shear loading is studied. This result allows us to study the limitations of the CADD3d coupling scheme.

In Chapter 8 - *Frank-Read Source Dynamics in Al and Al-5%Mg*, CADD3d will be applied on one interesting plasticity problem: a double Frank-Read source in Al and Al-5%Mg. The simulation results show two material strengthening effects: solute hardening and grain-boundary strengthening. These results will highlight the potential usage of CADD3d for studying many aspects of nano/micro scale plasticity including naturally size effects.

This thesis will be concluded with summary and outlook of the CADD3d method in Chapter 9 - *Concluding Remarks and Outlook*.

2 Experimental Studies on Size Effects

Among the three different types of defect described in the previous section, dislocations are specially important to understand the size-dependent material behaviors. There is a vast literature about the size effects occurring due to dislocation dynamics [Wang et al. (2006); Nix and Gao (1998); Greer et al. (2008); Gao et al. (1999)], and several experimental observations have been summarized in multiple recent reviews [Arzt (1998); Greer and Hosson (2011)]. In this chapter, we begin our discussion by presenting the common terminology used to describe crystal structures and dislocations. After such a brief introduction, we shall discuss the relationship between size effects and dislocations by reviewing several experiments. Furthermore, a proposed theoretical model explaining the experimental observations will be described for each of the size effects.

Crystal Structure

A crystal is an ordered arrangement of atoms determined by the force field due to electrons and nuclei interactions. The three most common close-packed structures are:

1. FCC: Face-centered cubic (Aluminum, Copper, Gold)
2. BCC: Body-centered cubic (Chromium, Iron)
3. HCP: Hexagonal-closed-packed (Magnesium, Zinc).

Many crystallites may exist in a poly-crystalline material. The interface between two grains (or crystallites) is called a grain boundary [Banabic (2000)]. More generally, a crystal may be distorted by the presence of defects. Figure 2.1 is a schematic of a generic crystal structure including several defects highlighted with red symbols. Depending on their spatial dimensions, the defects can be categorized into three types as follows:

1. Zero dimension: point defects (vacancies, interstitial and substitutional atoms)

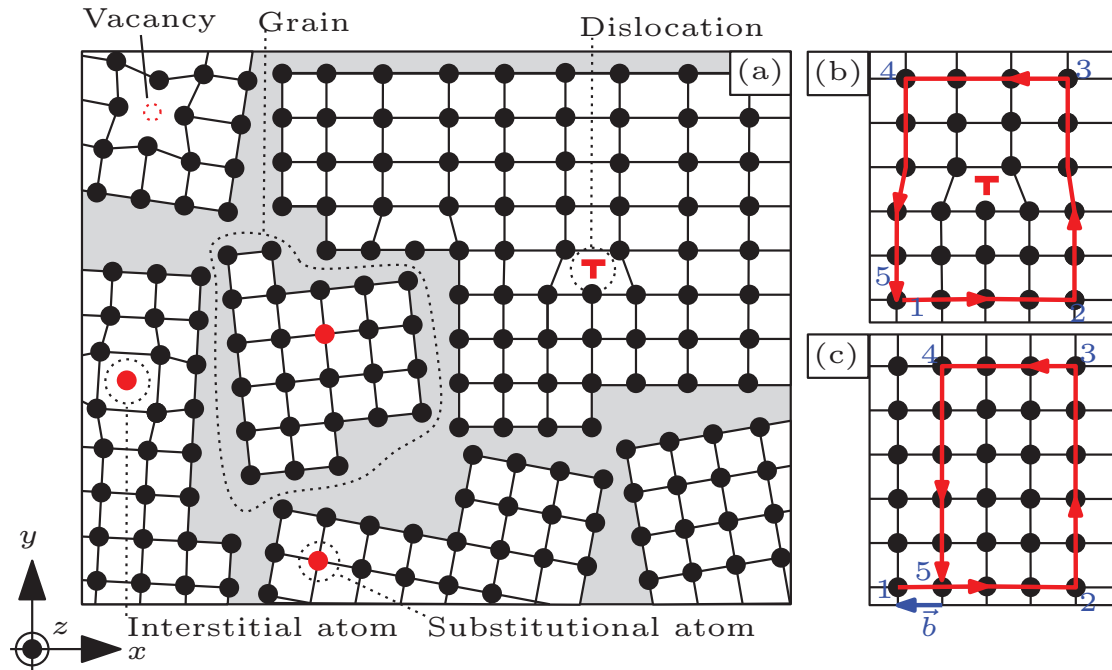


Figure 2.1 – (a) Schematic of a crystalline structure including multiple grains and defects. The gray region depicts the grain boundaries. (b) A Burgers circuit enclosing the dislocation. (c) The same Burgers circuit in a perfect reference lattice. The special vector needed for closing the circuit is the Burgers vector \vec{b} .

2. One dimension: line defect (dislocations)
3. Two dimension: plane defect (grain boundaries, stacking faults)

Among these three different types, let us focus on the line defect called dislocation. A lattice structure around the dislocation is shown in Figure 2.1 (b) (shown with T). Around the dislocation, a closed circuit (the red solid line with the arrows), i.e. 1→2→3→4→5, is illustrated. If the same atom-to-atom sequence is made in a perfect crystal (Figure 2.1 (c)), the circuit is not closed because the lattice including the dislocation has one more half atomic plane. The vector required to complete the circuit is called the Burgers vector \vec{b} [Hull and Bacon (2011)].

Depending on the angle between a line direction $\vec{\xi}$ and the Burgers vector \vec{b} direction, a dislocation can be categorized. The two most distinct dislocation types are shown in Figure 2.2: (a) an edge dislocation and (b) a screw dislocation. The Burgers vectors \vec{b} and the line directions $\vec{\xi}$ are given by the red and blue arrows, respectively. The angle between Burgers and line directions is the character angle θ , which takes the values 0° and 90° degrees for the screw and edge dislocations respectively. Character angles in the range $0^\circ < \theta < 90^\circ$ lead to mixed dislocations.

The application of an external shear stress $\overline{\sigma}$ (caused by any deformation, including the

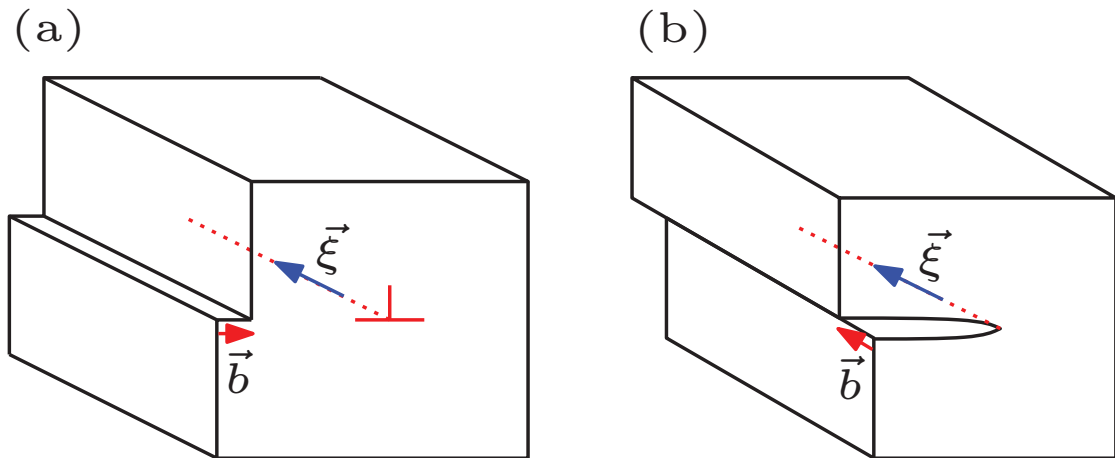


Figure 2.2 – Three dimensional views of an edge (a) and a screw (b) dislocations. The Burgers vectors \vec{b} are described with the red arrows, and the dislocation line directions $\vec{\xi}$ are depicted with the blue arrows.

presence of other defects) may induce the motion of a dislocation. The effective force acting on a dislocation is always perpendicular to the dislocation line and is linked with the shear stress component aligned with the Burgers vector direction $\vec{\sigma}_r = \vec{\sigma} \cdot \vec{b}$ (so-called the resolved shear stress). The relationship between the force \vec{f} per unit dislocation length and the resolved shear stress $\vec{\sigma}_r$ can be determined by the Peach-Köhler formulation [Peach and Köhler (1950)]:

$$\vec{f} = \vec{\sigma} \cdot \vec{b} \times \vec{\xi} = \vec{\sigma}_r \times \vec{\xi} \quad (2.1)$$

The minimum external stress required to move a dislocation is the so-called Peierls stress $\vec{\sigma}_p$. The Peierls stress is determined by the details of the dislocation atomistic core structure, and consequently varies with the character angle.

A dislocation motion can be better understood with Figure 2.3, which shows an example of edge dislocation motion. The movement of the dislocation is the consequence of the additional plane of atoms (in blue) moving to the right. The final picture of the movement shows a macroscopic plastic step of one atomic distance ($|\vec{b}|$). In real metals, a dislocation motion is more complicated than the simplistic view illustrated in Figure 2.3, because a distorted crystal lattice structure supporting a dislocation interacts with every other defects at long distance through the elastic field of deformation. Thus, dislocations may glide, or be pinned because of the presence of voids, dislocations, grain boundaries and with the applied loads. Therefore, materials can become harder during their plastic flow, which is the source of all strain hardening effects.

In general, dislocation movements yield various strengthening effects, and consequently lead to size dependent plastic deformations (size effect) as discussed in the previous chapter. In the next section, we will briefly review several experimental observations of such size effects

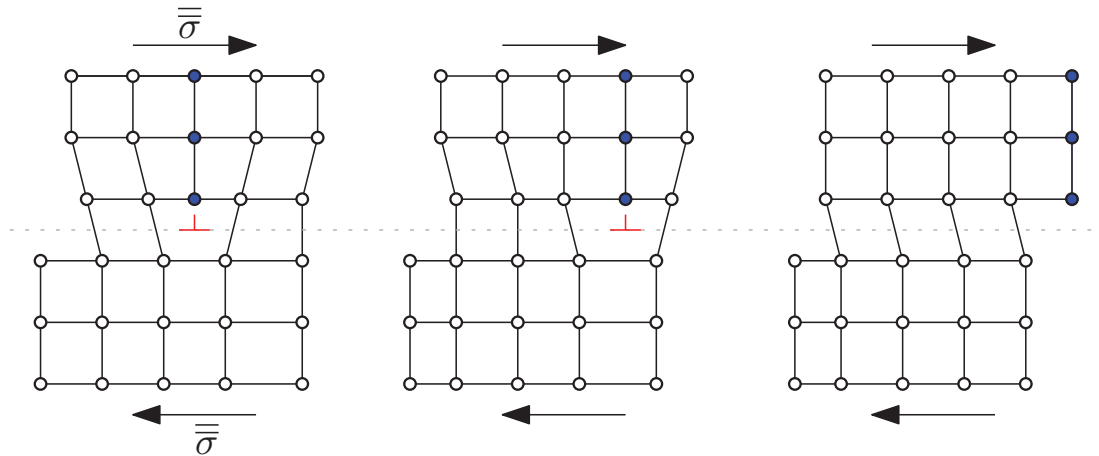


Figure 2.3 – Sequences of slip by movement of an edge dislocation under an external shear load $\bar{\sigma}$. Shift of the upper half of the crystal is emerged after the edge-dislocation traveling.

with a focus on their links with dislocation motions. Moreover, the corresponding theoretical models, which have been proposed to describe the experimental observations, will also be discussed.

Size dependent strengths

Over the past decades, many experiments allowed to observe at the nano- and micro-scales, that the crystalline strengths are inversely proportional to the sample sizes. Such size dependent mechanical behaviors are observed for various material types (pure and alloy metals), crystalline structures (single and poly-crystalline), and loading conditions (torsion, indentation and compression). Those experiments have revealed that such size effects occur as consequences of dislocation dynamics, and have tried to characterize their observations by proposing theoretical models. In the following sub-sections, the three most important mechanisms and models explaining the size effects are discussed.

Geometrically-Necessary-Dislocations

The first mechanism is a local mis-orientation effect. For example, in micro-indentation experiments, scale-dependent material behaviors [Nix and Gao (1998); Zaafarani et al. (2006)] are observed. In general, indentation size effects are due to the two factors: the decrease of indentation depth or of the indenter size lead to a decrease of hardness. Figure 2.4 (a) shows a specimen submitted to several indentations. The dislocation densities associated with the deformations are shown in Figure 2.4 (b). We observe a high dislocation density under the indented regions. These dislocations are due to non inhomogeneous strains and are called geometrically necessary dislocations (GNDs) [Nye (1953)]. Such highly deformed localized regions include many GNDs by necessity to accommodate for the volume of material

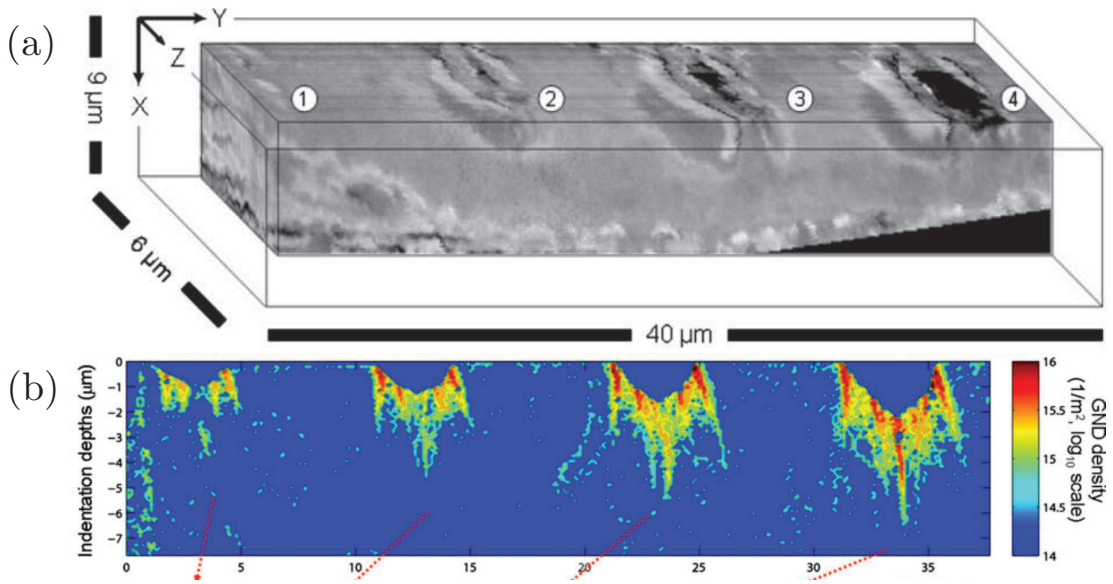


Figure 2.4 – The indentation size effect and the density of geometrically necessary dislocations (GNDs). (a) An experimental observation of a specimen with four indents. (b) The distribution of the GNDs density below and around indents. Figures from [Zaafarani et al. (2006)]

displaced by the indenter. These GNDs can also be found with other types of loading, such as bending and torsion, where inhomogeneous strains are created.

Based on multiple experimental observations of strain gradients and GNDs, Fleck et al. [Fleck et al. (1994)] proposed to introduce a length-scale parameter accounting for the size of the region where the GNDs are nucleated. By carefully associating this parameter to the loading types or the specimen dimensions, size effects due to GNDs can be better predicted. For instance, in bending, the scale parameter can be related to half the thickness of the beam, while it can be also related to the radius of the indenter in case of an indentation. By considering this parameter in the crystal plasticity formalism, the so-called Strain Gradient Plasticity theory (ϵ GP) has emerged [Nye (1953); Ashby (1970)]. It has been implemented within the Finite Element Method (FEM) to solve problems including complex boundary conditions [Fleck et al. (1994); Gao et al. (1999)], and to successfully recover experimental size effects. Details of the computational method ϵ GP will be discussed in the next chapter.

Dislocation Starvation

Size effects can be also observed even without any significant strain gradient. When there are only few defects (sources for dislocation emission), it can be brought closer to a mechanism called the dislocation starvation effect. Because the total number of dislocation sources is in general linked to the extrinsic material structure (specimen size), such a dislocation starvation effect is frequently observed in experiments considering nano-scaled specimens [Wang et al. (2006); Kim and Greer (2009); Greer and Hosson (2011)].

Figure 2.5 (a) shows a nano-sized pillar, which includes multiple significant slipped planes due to the employed homogeneous-compression loading. Figure 2.5 (b) shows the

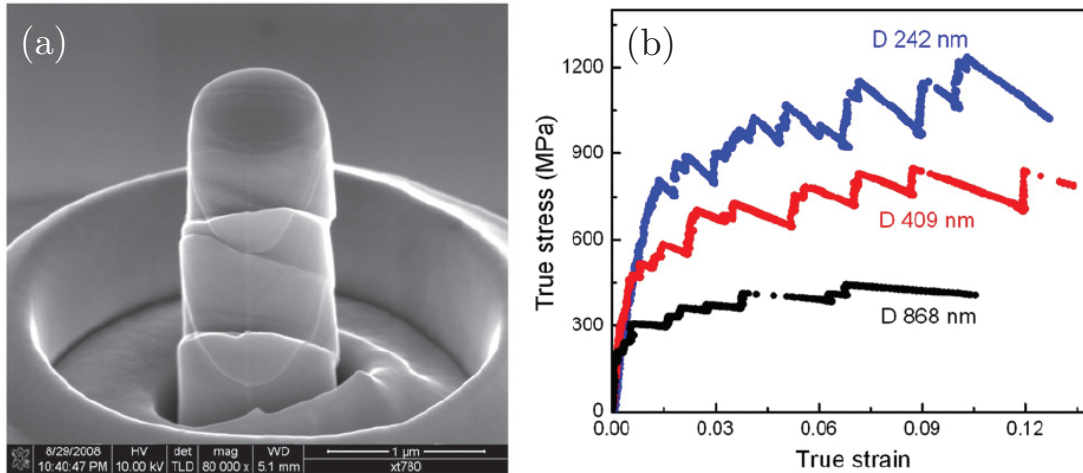


Figure 2.5 – (a) A compression test of a nano-sized pillar. (b) Strain-stress curves with different pillar sizes. The strength increases with decreasing of the specimen size. These figures are taken from [Greer and Hosson (2011)].

stress-strain curves obtained with different sizes for the nano-pillar. We clearly observe that the smallest nano-pillar shows the highest compressive strength. Greer and Hosson [Greer and Hosson (2011)] interpret this size effect with the following mechanism: when a specimen is small, initially existing dislocations annihilate easily at the free surfaces, and let the crystal sample starve for dislocations. In order to sustain higher loads, new dislocations have to be nucleated requiring significantly higher stresses than when compared to nucleation stresses from existing defects. The stress drop steps visible in Figure 2.5 reflect the creations of new dislocations, which are attracted to the close free surfaces. This is the starvation-nucleation effect.

To study this size effect, the dislocation nucleation process has to be accurately described. Such a process can be studied by describing the atomistic nature of the specimen with Molecular Dynamics (MD) and a proper set of inter-atomic potentials. Such size effect studies realized with MD will be discussed in Chapter 3.

Intrinsic Material Structures

Size effects can be also observed when the material has micro structures. We have to consider that voids, substituted atoms in alloys, sessile dislocations and grain boundaries may act as obstacles to dislocation motion. Figure 2.6 (a) shows a 2D schematic of a chain of dislocations piling-up at a grain boundary, while an experimental observation of the dislocation piling-up is presented in Figure 2.6 (b). The process is the following: during material deformation multiple dislocations are nucleated at dislocation sources, and driven by the loads they

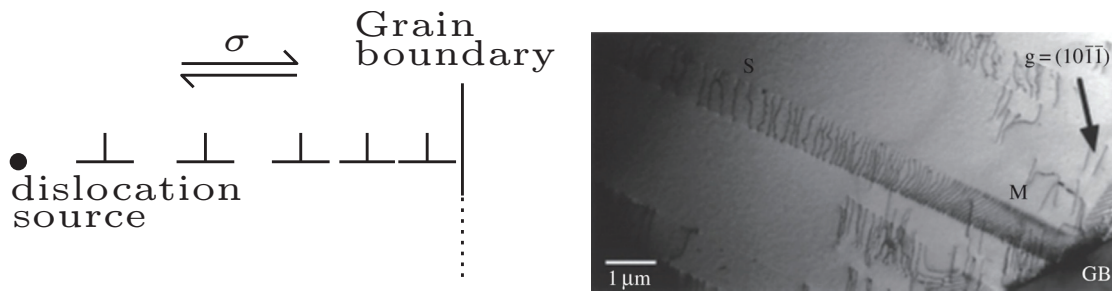


Figure 2.6 – (a) Schematic of a pileup of edge dislocations against a grain boundary. (b) An experimental observation of piled-up mixed dislocations in a titanium alloy. Figure from [Britton et al. (2015)]

approach grain boundaries. They eventually get arrested and are forced to pile-up against the grain boundaries. Each of these piled-up dislocations create a long range stress field, and the sum of them increases the backstress consequently, which is proportional to a number of the piled-up dislocations. This backstress reciprocally interacts with the dislocation-nucleation process. More precisely, the resolved stress acting on any dislocation source can decrease with the increase of backstress. The backstress can be large enough to prevent the dislocation sources to emit further dislocations: macroscopic hardening effect. Accordingly, with this mechanism, we can explain the classical Hall-Petch effect: the increase of yield strength with the decrease of grain size. This concept of anchored dislocation can be also used to understand the size effect occurring due to any type of obstacle for dislocation motion [Fleck et al. (1994); Greer and Hosson (2011); Arzt (1998)].

Conversely, nano-crystalline solids with nano-scale grains show an inverse hardening effect (softening) which is due to the motion of grains (i.e. grain-boundary sliding and partial dislocation emissions) rather than dislocations pile-up. In this thesis, we do not consider this softening effect, and the interested reader should refer to the literature [Schiotz et al. (1998); Jang and Greer (2011)].

Based on the experimental observation of dislocation-obstacle interactions, the Stress Gradient Plasticity (σ GP) has been proposed [Chakravarthy and Curtin (2011); Bai et al. (2014)]. This theory includes a material length scale parameter that considers the backstress applied as a restriction on dislocation nucleation sources. Unlike for ϵ GP, the length scale parameter is chosen to match a structural dimension: the average size of the material intrinsic structures (grains). On the other hand, this size effect can also be studied by considering individual dislocation motions instead of employing such a length scale parameter. To that end, one can use Discrete Dislocation Dynamics (DDD), which has successfully predicted several complex dislocation interactions for various material intrinsic structures. The detailed implementation of σ GP and DDD will be given in Chapter 3.

In this chapter, we have reviewed the size effects with the three distinct mechanisms: GNDs, dislocation starvation/nucleation and intrinsic material structures. To model those

Chapter 2. Experimental Studies on Size Effects

mechanisms, the four theories have been proposed: ϵ GP, σ GP, DDD and MD. In fact, there are many experimental observations showing size effects as consequences of combinations of these mechanisms. For example, when nano-scale pyramidal structures are compressed, GNDs and starvation/nucleation processes are strongly associated to the observed size effects [Wang et al. (2006)]. Therefore, complementary applications of the proposed models are necessary to fully describe size dependent material behaviors. For this reason, in the next chapter, we review these four models (ϵ GP, σ GP, DDD and MD) as well as multiscale methods with respect to their application and limitations.

3 Computer Simulation Methods employed to study Size Effects

In the previous chapter, we have presented various theoretical models that aim to account for size dependent material behaviors. Each of these theories acknowledges the dislocation contribution to strain hardening at a specific length scale. For instance, continuum plasticity models were extended by introducing material length scale parameters, and more refined mechanical descriptions were used to explicitly represent dislocations. To apply these models on problems involving complex geometries and boundary conditions, several computer-based approaches have been developed and employed during the last decades. Through numerical approaches, researchers can analyze and predict the relationship between dislocation dynamics and material plasticity. This chapter gives a brief non-exhaustive list of such computer simulation methods. However, we state again that these simulations and models apply only to the scale they were designed for. Describing the range of experimentally observed plastic behaviors requires a numerical model that considers several scales: a multiscale method. We will present such methods with a focus on one model, which was developed prior to this Ph.D work. After reviewing all these methods, the development of our new multiscale method for 3d dislocation dynamics will be motivated.

Finite Element Analysis

One of the most used numerical methods for plasticity modeling is the Finite Element Analysis (FEA) method [Hughes (1987)]. It finds approximated solutions of differential equations for a given spatial discretization. More precisely, a continuum domain is discretized into small elements for which the differential equation is solved approximately. The main advantage of such a discretization approach is to give the ability to solve mechanical problems under complicated boundary conditions. This feature enables us to study various interesting plastic-deformation problems.

To correctly describe plastic behaviors, several plasticity models have been incorporated into FEA. Those models need constitutive equations, which relate strains ϵ and stresses σ , such that hardening behaviors are effectively described. The first building stone is to decompose the

Chapter 3. Computer Simulation Methods employed to study Size Effects

strain rate in its elastic and plastic contributions as for instance in small deformations [Huang et al. (2004)]:

$$\dot{\epsilon}_{ij} = \dot{\epsilon}_{ij}^e + \dot{\epsilon}_{ij}^p \quad (3.1)$$

with $\dot{\epsilon}_{ij}^e$ the elastic strain rate and $\dot{\epsilon}_{ij}^p$ the plastic strain rate. These two rates can be defined by the conventional J_2 -flow theory [Mises (1913)]:

$$\begin{aligned} \dot{\epsilon}_{ij}^e &= \frac{1}{2\mu} \dot{\sigma}'_{ij} + \frac{1}{9K} \dot{\sigma}_{kk} \delta_{ij} \\ \dot{\epsilon}_{ij}^p &= \frac{3\dot{\epsilon}^p}{2\sigma_e} \sigma'_{ij}, \end{aligned} \quad (3.2)$$

where μ is the shear modulus, K is the bulk modulus, $\dot{\sigma}'_{ij} = \dot{\sigma}_{ij} - \frac{1}{3} \dot{\sigma}_{kk} \delta_{ij}$ is the deviatoric stress rate, $\sigma_e = \sqrt{\frac{3}{2} \sigma'_{ij} \sigma'_{ij}}$ is the von Mises effective stress, and $\dot{\epsilon}^p = \sqrt{\frac{3}{2} \dot{\epsilon}_{ij}^p \dot{\epsilon}_{ij}^p}$ is the equivalent plastic strain rate. According to the power-law visco-plastic model, the equivalent plastic strain rate $\dot{\epsilon}^p$ can be defined as [Hutchinson (1976); Pan and Rice (1983); Kok et al. (2002)]:

$$\dot{\epsilon}^p = \dot{\epsilon} \left[\frac{\sigma_e}{\sigma_{flow}} \right]^m, \quad (3.3)$$

where $\dot{\epsilon} = \sqrt{\frac{2}{3} \dot{\epsilon}'_{ij} \dot{\epsilon}'_{ij}}$ is the effective strain rate, σ_{flow} is the plastic flow stress, and m is the rate-sensitivity exponent. Consequently, the visco-plastic constitutive law can be written as [Huang et al. (2004)]:

$$\dot{\epsilon}_{ij} = \frac{1}{2\mu} \dot{\sigma}'_{ij} + \frac{1}{9K} \dot{\sigma}_{kk} \delta_{ij} + \frac{3\dot{\epsilon}}{2\sigma_e} \left[\frac{\sigma_e}{\sigma_{flow}} \right]^m \sigma'_{ij} \quad (3.4)$$

Equation 3.4 can account for various strain hardening effects through the choice of the plastic flow stress σ_{flow} .

In fact, the elasto-plastic deformation occurs as the consequence of crystallographic slip mechanisms. Therefore, by associating crystalline textures (i.e. Burgers vector and slip system) with the plastic flow stress σ_{flow} , more realistic hardening behaviors can be realized. This approach is the so-called crystal plasticity, and it has been implemented into FEA framework [Peirce et al. (1982)]. The classical crystal plasticity method considers dislocation slip as the only deformation mechanism [Roters et al. (2010)]. When it is applied on small-scale deformations, its constitutive equation is insufficient to describe size dependent material behaviors.

Size effects can be introduced into the crystal plasticity framework by employing additional theories to model σ_{flow} . In the last decades, two phenomenological theories have been proposed: the strain-gradient plasticity ϵ GP [Nye (1953)] and the stress-gradient plasticity

σ_{GP} [Chakravarthy and Curtin (2011)]. These two models are briefly reviewed in the following sub-sections with a special focus on the modeling of the plastic flow stress σ_{flow} .

Strain-Gradient Plasticity

The first model is the strain-gradient plasticity (ϵGP) proposed by Fleck et al. [Fleck et al. (1994)]. As discussed in sub-Section 2.2.1, the physical motivation of this method is the geometrically-necessary dislocations (GNDs), where local lattice distortions (i.e. strain gradients) are observed [Nye (1953); Ashby (1970)]. Therefore, Fleck et al. acknowledged its associated hardening contribution into σ_{flow} by introducing a material length scale l . Although this theory was inspired by concepts in dislocation mechanics, the original theory was isotropic and did not include any crystalline structure [Fleck et al. (1994)]. It has been recently extended to refine the formalism to include crystallographic systems [Gao et al. (1999); Huang (2000)], and the basic concept can be explained as follows.

The flow stress σ_{flow} in terms of the dislocation density ρ is expressed as:

$$\sigma_{flow} = C' \mu \vec{b} \sqrt{\rho} = C' \mu \vec{b} \sqrt{\rho_S + \rho_G} \quad (3.5)$$

where ρ_S is the density of statistically stored dislocations (SSDs)¹, ρ_G is the density of geometrically necessary dislocations (GNDs), μ is the shear modulus, C' is an empirical constant, and \vec{b} is the Burgers vector. Nye [Nye (1953)] showed that the density of GNDs ρ_G is related to the curvature of plastic deformation (i.e. the strain gradient η):

$$\rho_G = \frac{\eta}{\vec{b}} \quad (3.6)$$

Its substitution into Equation 3.5 yields

$$\sigma_{flow} = C' \mu \vec{b} \sqrt{\rho_S + \frac{\eta}{\vec{b}}} \quad (3.7)$$

In a homogeneous deformation (i.e. uniaxial tension), the strain gradient η is canceled out, and the flow stress can be simplified as follows:

$$\sigma_Y f(\epsilon^P) = C' \mu \vec{b} \sqrt{\rho_S}, \quad (3.8)$$

where σ_Y is the tensile yield stress, and $\sigma_Y f(\epsilon^P)$ is the hardening behavior for the uniaxial tension. Then, the density of SSDs can be evaluated from Equation 3.8:

$$\rho_S = \left[\frac{\sigma_Y f(\epsilon^P)}{C' \mu \vec{b}} \right]^2 \quad (3.9)$$

Finally, we obtain the flow stress accounting for the non-uniform plastic deformation associ-

¹Dislocations generated during homogeneous plastic deformations of crystals.

ated with GNDs by inserting Equation 3.9 into Equation 3.7:

$$\sigma_{flow} = \sqrt{\sigma_Y^2 f^2(\epsilon^p) + C'^2 \mu^2 \vec{b} \eta} = \sigma_Y \sqrt{f^2(\epsilon^p) + l \eta} \quad (3.10)$$

where

$$l = C'^2 \left(\frac{\mu}{\sigma_Y} \right)^2 \vec{b} \quad (3.11)$$

is the intrinsic material length scale, which depends on the material parameters μ , σ_Y and \vec{b} . For typical metallic materials, μ/σ_Y is in the order of 10^2 , and \vec{b} is in the order of 10^{-10} meters. Consequently, the length scale is in the order of micro-meters (10^{-6}). This fact is consistent with the size effect observed at nano- and micro-scales. This model has been incorporated into the FEA method, and has been successfully applied to predict size effects with several loading conditions (i.e., bending, torsion and indentation) and material types (single crystal and thin films) [Nix and Gao (1998); Fleck et al. (1994); Huang (2000)].

However, predicting every experiment for the same material and with the same length scale parameter l does not always work [Evans and Hutchinson (2009)]. After all, the length scale l is not a universal parameter which limits the applicability of ϵ GP. Furthermore, recent experiments showed size effects even though neither GNDs nor local-inhomogeneous lattice distortions could be measured [Greer et al. (2008)]. This is clearly beyond the scope of ϵ GP.

Stress-Gradient Plasticity

The previously mentioned limitation of ϵ GP can be resolved by defining the plastic stress flow with a physical length scale L associated with the employed sample. As discussed in sub-Section 2.2.3, the interactions between dislocations and the surrounding obstacles are important to understand size effects. With this concept, the parameter L can be chosen as an averaged distance between obstacles, allowing to consider stress gradient contributions to the yield strength. This idea leads to the so-called stress-gradient plasticity σ GP theory, and has reproduced favorably the size effects usually observed for bending and torsion loads in poly-crystalline metals [Chakravarty and Curtin (2011)]. The hardening mechanisms considered in σ GP can be explained with the dislocation source-obstacle model shown in Figure 3.1. Under an applied shear stress σ_{app} , a dislocation source (at $x = 0$) nucleates dislocation dipoles which will pile-up because of the obstacles (at $x = \pm L_{obs}/2$). The resulting stress is linearly varying with a stress-gradient parameter χ .

With the linear elastic continuum theory, the yield stress σ'_Y for this configuration can be analytically computed as follows:

$$\sigma'_Y = \frac{\sigma_Y}{1 - \chi L_{obs}/4} \text{ with } \sigma_Y = \sqrt{\frac{4\mu|\vec{b}|}{\pi(1-\nu)} \frac{\sigma_{obs}}{L_{obs}}} \quad (3.12)$$

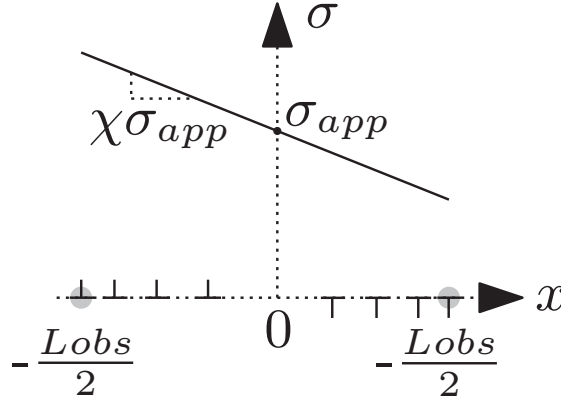


Figure 3.1 – Dislocations are emitted from a source ($x = 0$), and are piled-up against obstacles ($\pm L_{obs}/2$) under a shear stress σ_{app} . Figure from [Chakravarthy and Curtin (2011)].

with σ_Y the yielding stress under uniaxial tension, μ the shear modulus, ν the Poisson's ratio and σ_{obs} the obstacle strength. Consequently, the flow stress accounting for the stress gradient χ can be evaluated as

$$\sigma_{flow} = \sigma'_Y f(\epsilon^P) = \left(\frac{\sigma_Y}{1 - \chi L_{obs}/4} \right) f(\epsilon^P) \quad (3.13)$$

Equation 3.13 highlights the difference between ϵ GP and σ GP: the hardening contribution due to the presence of the stress gradient χ is considered instead of the strain gradient η . Finally, σ GP describes the size effect due to the variation of the material strength σ'_Y , which is inversely proportional to the distance between the obstacles L_{obs} .

Consequently, the σ GP model can describe size effects driven by intrinsic material structures. However, this model is only valid for domains with simple slip systems and modest dislocation motions. For instance, a too large number of dislocations may pile-up against an obstacles. In reality, dislocations may transfer to other slip planes (i.e. cross-slip) under high temperatures or high applied stresses, and such complex dislocation motions cannot be considered by σ GP. In these situations, it is necessary to characterize dislocation motions explicitly, which is usually done with the methods described in the next sub-sections.

Discrete Dislocation Dynamics (DDD)

In this section, we turn our attention to a method which explicitly represents dislocations and their evolution in time: the so-called Discrete Dislocation Dynamics (DDD). By tracking the motion of dislocations in response to local stresses from the externally applied loads or the elastic interactions with the other dislocations, this method provides a full access to realistic dislocation-driven material deformations. The typical length scale where this method is applied is the micro-scale. At this specific scale, dislocations are individually observed as curved lines with the Transmission Electron Microscopy (TEM).

Chapter 3. Computer Simulation Methods employed to study Size Effects

In the following sub-sections, we review the implications of using DDD with two dimensional [Kubin and Canova (1992)] and three-dimensional [Arsenlis et al. (2007)] systems. There are significant differences between 2d and 3d which are crucial to understand the new possibilities provided by this Ph.D work.

2d DDD

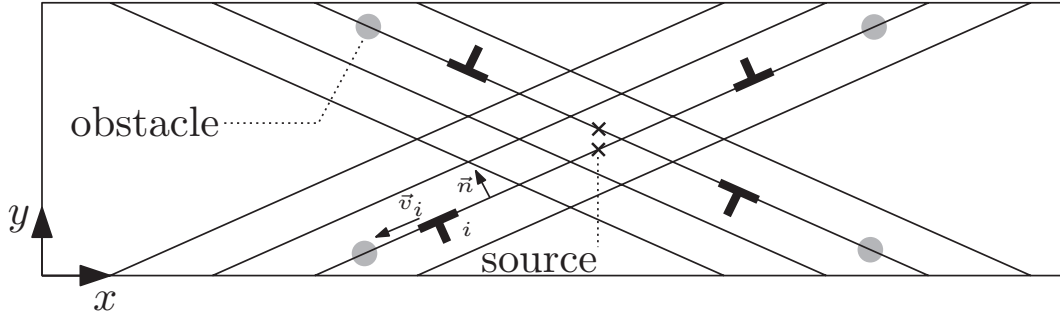


Figure 3.2 – Schematic of a single crystal system including multiple slip systems and dislocations. Figure from [Van der Giessen and Needleman (1995)].

Figure 3.2 shows a planar DDD system with several slip systems. Due to the two dimensional-nature of this system, only infinite straight dislocations (shown with the markers \perp) are taken into account, and they can be viewed as point-wise objects.

Such dislocations are parallel to one another and perpendicular to the $x - y$ plane such that only one character angle θ can be considered. These dislocations interact with each other through elastic fields. The effective force acting on such point-like entity is computed as the energy variation associated with its position:

$$\vec{f}_i = -\frac{\partial e_{tot}}{\partial \vec{x}_i}, \quad (3.14)$$

where \vec{f}_i is the force per unit length, e_{tot} is the total elastic energy per unit length (due to the plane strain/stress hypothesis), and \vec{x}_i is the coordinate of the point i . In order to compute the evolution in time of these dislocations, the velocity \vec{v}_i of every points can be determined by the so-called mobility law:

$$\vec{v}_i = B(\theta, T)(I - \vec{n} \otimes \vec{n})\vec{f}_i = B_\theta(T)(I - \vec{n} \otimes \vec{n})\vec{f}_i, \quad (3.15)$$

where \vec{n} is the normal unit vector of a given slip plane, I is an identity matrix, and $B(\theta, T)$ is a dedicated damping parameter, which accounts for the energy dissipated during a dislocation motion. Physically, this damping mechanism occur due to phonon-viscous drag forces in a crystal lattice, and should be defined as a function of θ and T [Hirth and Lothe (1992)]. We note that in 2d DDD only one character angle θ is considered, such that the damping parameter

is reduced to the function of temperature $B_\theta(T)$. In general, this damping parameter can be evaluated either from experiments, theory or molecular dynamics simulations.

To describe size effects due to intrinsic material structures with 2d DDD, two more ingredients (the nucleation sources and the obstacles) are required. Indeed, the creation of new dislocations is realized when the resolved shear stress overcomes a critical stress at predefined locations: the nucleation sources. In this circumstance a dislocation dipole is introduced next to the loaded source. After the creations, the dislocations can travel according to the mobility law previously described, but can also be pinned by the obstacles. The pinned dislocations can only pass the obstacles when their resolved stresses exceed the blocking obstacle strength.

On the other hand, when dislocations pile-up against obstacles, their associated stresses add-up and increase the effective backstress in the entire domain. As already described in the previous chapter, these pile-up structures can decrease the resolved stress on the sources and lead to hardening by preventing emissions of new dislocations [Van der Giessen and Needleman (1995); Devincre and Kubin (1994)]. This hardening mechanism that 2d DDD takes into account is similar to the concept of σ_{GP} : piled-up dislocations increase the resolved stresses acting on the dislocation sources. Like σ_{GP} , the 2d DDD method cannot represent plastic hardening due to complicated dislocation motions as can be observed in nature. This is because dislocations are generally curved objects and not straight, which invalidates the point-like representation. Only three dimensional systems allow to consider realistic dislocation structures and motions.

3d DDD

Again, to consider the generally curved shape that dislocations can take, 3d discrete dislocation dynamics simulations are required. Figure 3.3 (a) [Arsenlis et al. (2007)] shows a snapshot of a 3d DDD simulation: a BCC metal (Mo) cube of $10 \mu m^3$ under uniaxial tension. We can find multiple arbitrarily shaped dislocations forming complex networks. Like the 2d DDD framework, these dislocations interact with each other through the elastic force field, and move by following the mobility law. During their motion, some dislocations meet, connect, and compose junctions (shown as red lines) according to pre-defined topological operations. The junctions can form strong obstacles and impede other dislocations motions. Consequently, the size effect due to pinned dislocations can naturally be obtained without the need for ad-hoc obstacles as for 2d DDD.

Dislocation nodes, forces and mobilities

Figure 3.3 (b) [Bulatov and Cai (2006)] illustrates a generic topology accounted in 3d DDD. We observe that the dislocation lines are made of a set of nodes connected by straight segments. For a given node, a Burgers vector is defined. At a node, the sum of all incoming

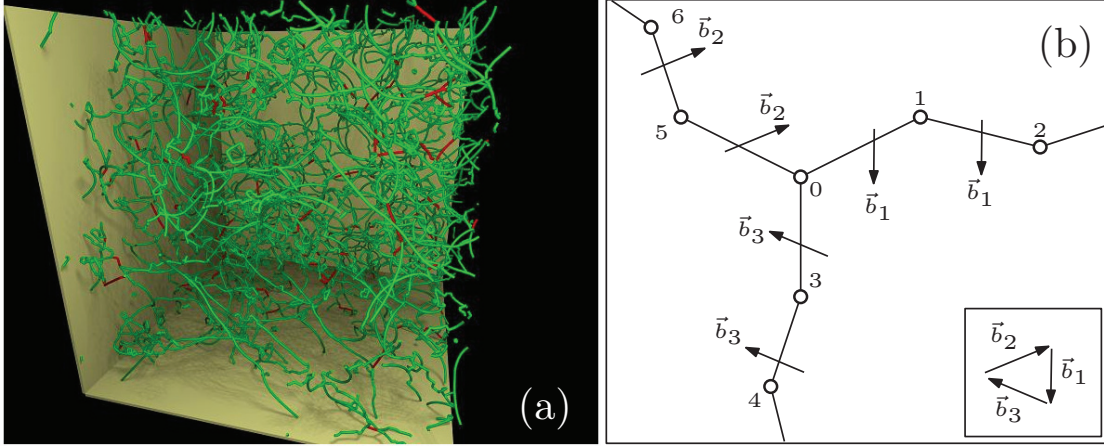


Figure 3.3 – (a) A snapshot of discrete dislocation dynamics simulation with a BCC metal of $10 \mu\text{m}^3$. Dislocations are colored by the Burgers vectors. Figure from [Arsenlis et al. (2007)]. (b) A dislocation network is composed of a set of nodes (empty circles) interconnected by straight lines. Figure from [Bulatov and Cai (2006)].

Burgers vectors matches the sum of all outgoing Burgers vectors.

Again, the effective nodal force acting on a node is evaluated with the negative derivative of the total energy of the system with respect to the node coordinate.

$$\vec{f}_i = -\frac{\partial E_{tot}}{\partial \vec{x}_i} \quad (3.16)$$

However, if compared to 2d DDD, 3d DDD requires additions for the computations of the nodal forces and velocities because of the curved nature of dislocations. First, the total energy is computed on a volume (while in 2d e_{tot} is an energy per unit length due to plane strain/stress conditions). Furthermore, this nodal force \vec{f}_i can be computed with the more convenient Peach-Köhler contour integral [Peach and Köhler (1950); Bulatov and Cai (2006)]:

$$\begin{aligned} \vec{f}_i &= \oint_C \vec{f}_{PK} N_i dl \text{ with} \\ \vec{f}_{PK} &= \overline{\overline{\sigma}} \cdot \vec{b} \times \vec{\xi}, \end{aligned} \quad (3.17)$$

where N_i is a linear interpolation function, $\overline{\overline{\sigma}}$ is the stress field of the system (due to all dislocations as well as externally applied loads), and $\vec{\xi}$ is the local tangent vector to the dislocation line.

Both the total energy E_{tot} and stress field $\overline{\overline{\sigma}}$ can be obtained by employing the linear elasticity theory. It is known that this linear elasticity theory predicts that E_{tot} is diverging if we account for the regions of space around dislocation cores. To avoid such an ill-posed condition, core and far-field regions have to be distinguished. The most generally implemented approach to effectively realize this separation for the far-field quantities is the non-singular dislocation

theory, which removes the core singularity by spreading the Burgers vector using a distribution function [Cai et al. (2006)]. In the end a nodal force takes the general form:

$$\vec{f}_i = \sum_{e=1}^{\#segments} \vec{f}_{e,i} + \vec{f}_i^{core} + \vec{f}_i^{external} \quad (3.18)$$

where $\vec{f}_{e,i}$ is the force created by segment e onto node i , where \vec{f}_i^{core} is the part of the self force created by the core energy term, and where $\vec{f}_i^{external}$ is the force created by stresses not due to the dislocation network, for instance such as the resultant of applied boundary conditions.

Like for 2d DDD, the nodal velocity \vec{v}_i is determined with the mobility law from the nodal forces \vec{f}_i . However, for a curved dislocation there are many character angles as shown in Figure 3.3 (b). Therefore, both dependencies on θ and T have to be considered in the drag coefficients $B(\theta, T)$ in Equation 3.15. The details of such a mobility law will be discussed in Chapter 6.

Although the 3d DDD model can describe complex dislocation motions, this model does not include a physically-based dislocation nucleation process, which needs an atomic description. Therefore, an ad-hoc treatment is required in 3d DDD. For instance by placing dislocations with an initial dislocation density or with sources capable of emitting new dislocations. Consequently the size effect involving dislocation nucleations (i.e. dislocation starvation discussed in sub-Section 2.2.2) cannot be studied with 3d DDD.

Classical Molecular Dynamics

Classical molecular dynamics (MD) is a simulation method representing materials at the atomistic level [Frenkel and Smit (2001)]. A set of atoms interacts through a force field derived from dedicated potentials. For instance embedded atom potentials [Daw et al. (1993)] account for some electronic effects and allow a more accurate atomistic force field for metallic materials. With a given force \vec{f}_i , the motion of the atom i is determined by integrating in time the Newton's second law:

$$m_i \ddot{\vec{r}}_i = \vec{f}_i \quad (3.19)$$

with m_i its mass and $\ddot{\vec{r}}_i$ its acceleration.

The MD principle is simple and can provide detailed information on plastic deformations of materials. Thanks to the atomic representation, dislocations are explicitly described as misfit structures. For example, Figure 3.4 (a) [Cho et al. (2015)] shows an edge dislocation with MD in a perspective view. Only the atoms below the slip plane ($Y = 0$ plane) are shown and

colored by their Y coordinate levels. The corresponding top view is depicted in Figure 3.4 (b) where the detailed dislocation core structure is highlighted. In particular the stacking fault region is particularly visible (stacking faults in FCC aluminum will be studied in Section 5.2). With accurate inter-atomic potentials, the dislocation nucleation process can be naturally predicted with MD simulations. As an example, Figure 3.4 (c) [Junge (2014)] shows the dislocations nucleated as a consequence of a nano-scratch test. The dislocation loops, which are represented by red atoms, are naturally nucleated under the indented surface (white atoms). We conclude that MD can be very useful to model size effects when the leading mechanism is

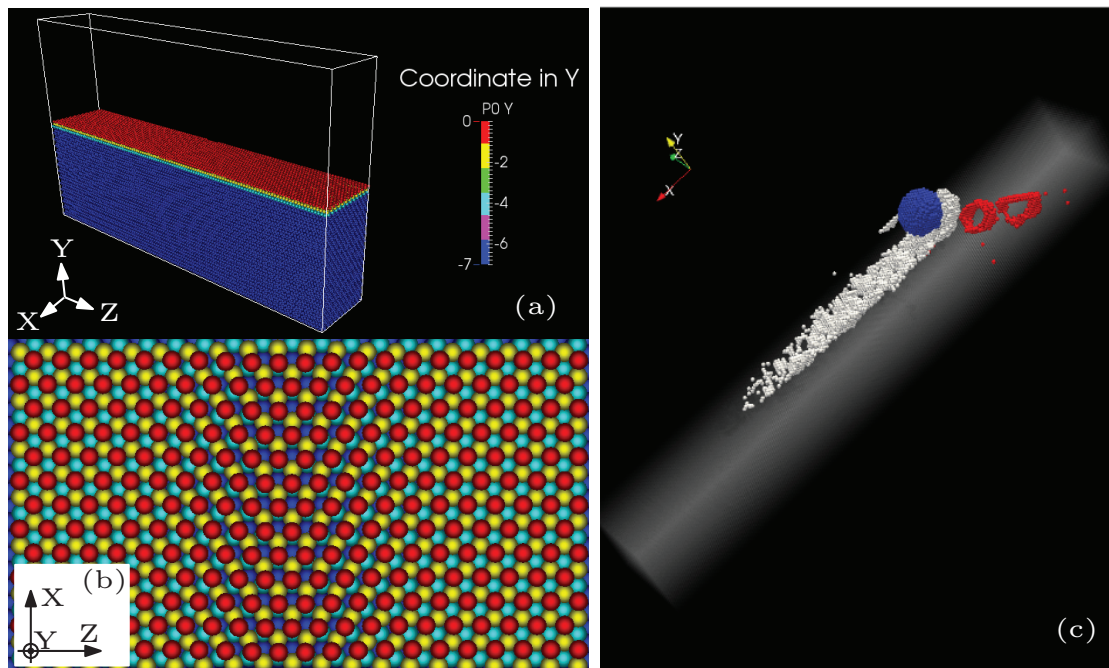


Figure 3.4 – (a) A perspective view of a MD system including an edge dislocation. Only the atoms below the slip plane are depicted, and are colored by the Y coordinate. Figure from [Cho et al. (2015)]. (b) The dislocation structure in the top view of the slip plane. The misfit stacking-fault sequence represents the edge dislocation structure in a FCC crystalline material. Figure from [Cho et al. (2015)]. (c) A snapshot of dislocation nucleation process during a nano-scratch simulation. Figure from [Junge (2014)]

the dislocation starvation (sub-Section 2.2.2).

However, the main constraint of MD is on the domain size, since the number of degrees of freedom increase very quickly with the specimen dimensions. For example, the number of atoms in a typical grain ($1\mu\text{m}^3$) of aluminum is approximately 25×10^{12} . Simulating so many atoms with MD is generally out of reach even with nowadays super-computers. Furthermore, the simulations with such a number of atoms are limited to short times. Consequently, crystal plasticity with medium grain sizes cannot be studied with MD.

Coupling Atomistic to Continuum Methods

In order to reduce the aforementioned computational cost it is possible to employ multiscale coupling methods. To that end, we need to identify the regions in which the fine scale resolution can be neglected and replaced with a cheaper representation, such as a coarser continuum-based finite element solver. Any coarsening implies a removal of some degrees of freedom. While it allows to manipulate a cruder solution, it however will inevitably cause unintended and spurious effects. The concurrent multiscale methods existing in the literature can be distinguished with the employed strategy to separate scales and to select the degrees of freedom to eliminate. Classically, we can distinguish the sharp interfaces from the overlapping ones.

The earliest approaches address the problem of scale decomposition by a sharp separation of atomic and continuum zones. The continuum is discretized on a mesh which is usually unrefined far for the atomic region, thus reducing the overall computational time. The discrete-continuum interaction is realized by exchange-type boundary conditions. The pioneering work of Kohlhoff et al. [Kohlhoff et al. (1991)], of Tadmor et al. [Tadmor et al. (1996)] and Abraham et al. [Broughton et al. (1999)] all employed this idea. Among them, the QuasiContinuum [Miller et al. (1998); Shenoy et al. (1999); Miller and Tadmor (2002); Dupuy et al. (2005)] (QC) is certainly the most famous atomic-to-continuum coupling method. It has been employed to study many fundamental problems of deformation in crystalline solids such as fracture [Miller et al. (1998)], grain boundary structure and deformation [Shenoy et al. (1998, 1999); Sansoz and Molinari (2005)], nano-indentation [Tadmor et al. (1999); Shenoy et al. (2000)] and three-dimensional dislocation junctions [Shenoy et al. (2000)].

In general, the difficulty of these methods lies in the difference in nature between the forces/energies between atoms and finite element nodes: atomic forces are non-local and non-linear, whereas the continuum mechanics theory usually considers a constitutive law based on local deformations. Therefore, a sharp boundary cannot be defined without causing side effects. In practice, we observe the emergence of ghost forces since local versus non-local force fields cannot be in perfect equilibrium all along the coupling region. Adding permanent configuration forces [Shenoy et al. (1999)] can help in reducing such ghost-forces. Concerning the non-linearity issue, a nice improvement can be made with the CauchyBorn rule [Tadmor et al. (1996)] which is a constitutive law based on the underlying crystal and inter-atomic potential (used in the QC approach).

When it amounts to the study of transient processes a sharp transition leads necessarily to wave reflections [Tadmor et al. (1996); Wagner and Liu (2003); Xiao and Belytschko (2004)]. Indeed, the mechanical waves coming from the atomic model cannot be transferred to a coarser model properly. Also it has been recently demonstrated that several displacement approaches are strongly unstable [Till et al. (2015)]. As stated, another strategy employs overlapping regions where the two models are co-existing and glued together with adequate operators. By spreading the coupling over space, the degrees of freedom removal can be made

smooth through space and time scales.

The method developed by Liu et al. [Liu et al. (2006); Wagner and Liu (2003)] treats the problem of wave reflections with Green functions [Liu et al. (2006)] in the fashion of perfectly matching boundary conditions. This allowed to compute the atomic vibrations for the atoms which have been replaced by a continuum representation. Another possibility is offered in the work of S. Xiao et al. [Xiao and Belytschko (2004)] which extends the Arlequin method of Ben Dhia [Hachmi and Rateau (2005)] to gradually mix the respective energy/influence of atoms and finite elements. Several applications of this class of methods may be found in the literature [Xiao and Belytschko (2004); Anciaux (2007); Anciaux et al. (2006); Xiao and Yang (2006); Luan et al. (2006)]. While these approaches address transient cases, the treatment of thermal fluxes through the interface needs additional treatments. Several methods [Wagner et al. (2008); Anciaux et al. (2012); Mathew et al. (2011); Ramisetti et al. (2013, 2014)] intent to handle heat in various ways, with a more or less important computational cost.

However, none of the previously presented methods address the challenge that defects represent. In particular, mobile defects such as dislocations may approach the continuum regions leading to artificial forces preventing accurate calculations. A proper treatment of dislocations, including their transfer to a DDD representation is the topic of the next section as well as this Ph.D thesis.

Coupled Atomistic and Discrete Dislocation Method in 2d (CADD2d)

DDD and MD permit to analyze dislocation dynamics and size effects at two different length scales: micro for DDD and nano for MD. However, in order to catch the most general size effect, we need to model both nucleations and long range elastic interactions. Thus, a multiscale approach modeling from nano- to micro-scales and handling dislocations is required.

The Coupled Atomistic and Discrete Dislocation Dynamics method (CADD2d) is a two dimensional multiscale coupling method between 2d DDD and MD [Shilkrot et al. (2004); Shiari et al. (2005)]. The key concept of the CADD2d method is a geometrical decomposition: an atomistic domain is used where dislocation nucleations are expected, whereas in the remaining zone DDD is employed. These two regions are mechanically coupled with each other such that dislocations can propagate from one domain to the other without any spurious force.

Figure 3.5 [Miller et al. (2004)] shows a snapshot of an indentation simulation realized with CADD2d. Figure 3.5 (a) shows the MD region, where a circular indenter is applied. Several dislocations were naturally nucleated, and moved away from the indented region. Once they are more than few nano-meters from the region of indentation, atomistic treatments are not necessary to describe their motions. Therefore, as depicted in Figure 3.5 (b) their behaviors are considered with the cheaper continuum description model (2d DDD). In order to solve the

3.5. Coupled Atomistic and Discrete Dislocation Method in 2d (CADD2d)

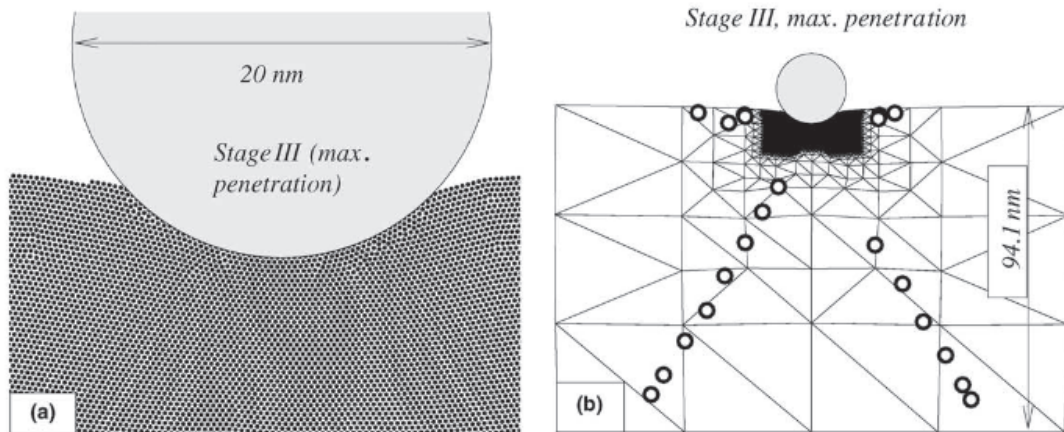


Figure 3.5 – An indentation study with CADD2d. (a) A close-up view at the indented surface in the MD domain. (b) A view of the complete CADD2d domain. Multiple dislocations nucleated under the indenter in MD are successfully transferred into DDD. Figures from [Miller et al. (2004)].

stress field solution of a finite boundary problem where the indentation and the free boundary boundary conditions are applied, the FE domain (mesh) is coupled with the DDD domain.

To seamlessly pass MD dislocations to the DDD region, the coupling scheme (so-called dislocation detection/passing) is conducted. This coupling scheme will be discussed in the following chapter. Finally, the MD dislocations are replaced by point-wise dislocations which travel in the DDD region as we described in sub-Section 3.2.1.

The two dimensional (plane strain) description of dislocations can be avoided by extending into three dimensional systems. Recently, a road map of the three-dimensional CADD (CADD3d) was proposed [Junge (2014)]. In the next chapter, based on the road map, the author presents the CADD3d methodology, which was extended and implemented into generic and parallel computing frameworks during the Ph.D work.

4 Coupled Atomistic and Discrete Dislocation Method in 3d (CADD3d)

In the previous chapter, we found that CADD2d has the advantage to describe material plastic deformations at nano- and micro-scales in a concurrent manner. This feature is essential to study the size effects experimentally observed (cf. Chapter 2). However, those are three-dimensional in nature. Thus CADD2d needs to be extended into three dimensional systems: CADD3d. It is expected to be very useful not only to study size effects but also to analyze many other plasticity problems such as indentations and crack blunting. Among the three different domains (MD, DDD and FEM), in this thesis we focus on the coupling between the MD and DDD domains, which has been developed as part of the CADD3d project ¹. In the following sections, the details of the development, implementation and algorithm of the MD+DDD coupling scheme will be discussed.

Differences between CADD2d and CADD3d

Infinite Straight Dislocations

Let us discuss the differences between CADD2d and CADD3d features. We will highlight the main development challenge for CADD3d. The key point of CADD2d is the scheme to detect and pass dislocations between the MD and DDD domains [Shilkrot et al. (2004); Shiari et al. (2005)]. The schematic procedure of this algorithm can be found in Figure 4.1. The MD region consists of a set of atoms (the full circles), and the boundary atoms (the empty circles) are linked with the DDD domain. As described in Section 3.5, to solve complex boundary condition problems, the DDD domain is coupled with the FEA domain (mesh). The boundary MD atoms are called *pad atoms*, and their motion are controlled by the displacements of the FE mesh. Therefore, the pure MD atoms communicate with the continuum through the displacement field of the pad atoms.

In two dimensional systems, a dislocation is represented as a point-like object, and

¹Swiss national science foundation project conducted by three principal investigators, William Curtin, Jean-François Molinari and Guillaume Ancaux.

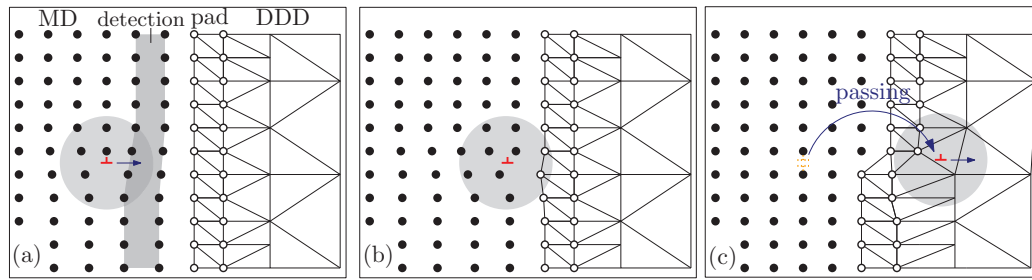


Figure 4.1 – The procedure of the detection/passing scheme of CADD2d. (a) An infinite straight dislocation approaches the DDD domain. The non-linear core region is shown as the grey circular area. This dislocation can be detected in the detection zone near the interface. (b) A repulsive spurious force applies on the MD dislocation because the DDD mesh cannot sustain the highly distorted core structure. (c) A successful dislocation passing from MD to DDD. This is done by introducing a DDD dislocation after the MD dislocation detection. The MD dislocation can disappear at the interface by adding the displacement field of a dislocation with the opposite sign.

such a point-wise dislocation may approach the DDD region as shown in Figure 4.1 (a). The displacement field created by the dislocation can be distinguished into two parts: the nonlinear core region (the grey circular area), where the linear elasticity theory cannot be used, and the far-field region, where it will be accurate enough. When the dislocation gets close to the interface as shown in Figure 4.1 (b), the nonlinear region includes not only the pure atoms but also the pad atoms. In such circumstances, the FE mesh results in a linear response which is too stiff. It brings artificial forces preventing the MD dislocation to get close to the continuum region. To solve this issue, a DDD node is introduced when an atomistic dislocation is detected in the *detection zone* (see figure 4.1 (a) and (c)). After such an introduction, there are two dislocations which strongly repel each other. The final step in the CADD2d passing strategy is to impose the displacement field of an image dislocation with an opposite Burgers vector, so that the remaining MD dislocation is strongly attracted to the interface where it will disappear. By this detection/passing scheme, the dislocation can effectively travel from MD to DDD. A similar strategy allows to realize the passing from DDD to MD (not described in here for conciseness).

Hybrid Dislocations

Such a detection/passing scheme cannot be applied in CADD3d since dislocations are curved objects in reality. Figure 4.2 (a) shows a schematic for a typical CADD3d domain. A MD region is employed where dislocation nucleation sources/defects exist, and is surrounded by a DDD domain. The detailed configuration of the interface between MD and DDD will be described in the following sub-section. Several dislocations are shown in Figure 4.2. When a dislocation is modeled with MD (and DDD), it is shown with a red line (and a blue line, respectively). It is important to note that a dislocation may cross the interface, and in this case it will have the two representations (atomistic and discrete) in one single dislocation structure,

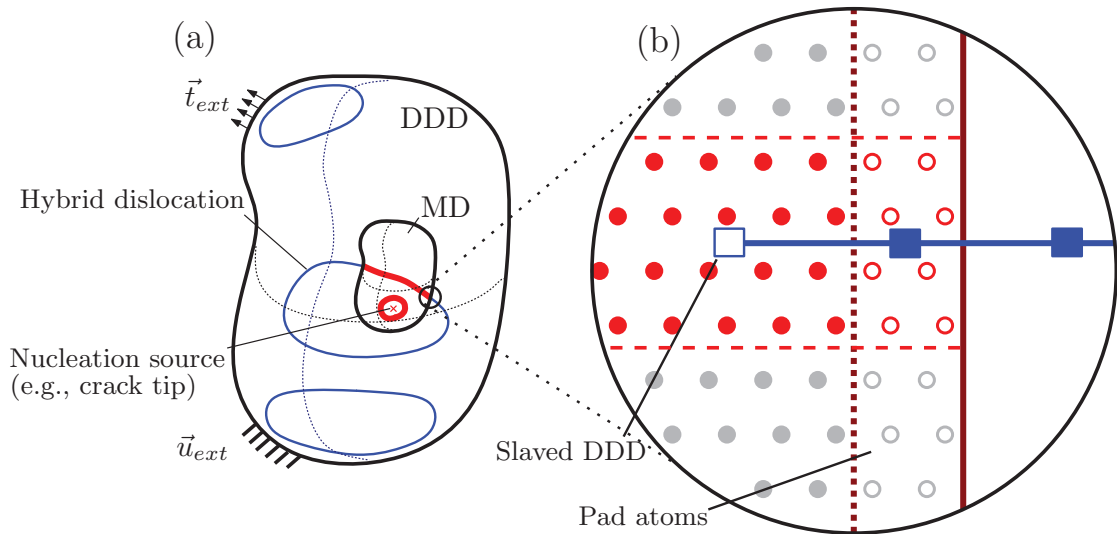


Figure 4.2 – CADD3d-domain decomposition. The MD region contains a dislocation source, while the remaining region is handled with DDD. Several dislocations are plotted. There is one dislocation loop which is partly in the MD domain and partly in the DDD zone. Such dislocation is the so-called *hybrid dislocation*.

which is called a *hybrid dislocation*.

Such hybrid dislocation requires particular features from CADD3d, which are not existing in the CADD2d formulation. First, the two different descriptions need to glide smoothly as one single dislocation structure. If they do not evolve in a similar manner, then a bi-material interface is effectively simulated which leads to inaccuracies. Figure 4.2 (b) shows the close-up view of the hybrid dislocation at the coupling interface. The MD atoms are bounded by pad atoms, which are constrained atoms, and the DDD dislocation is ended with a slaved DDD node. Therefore, by constraining the degrees of freedom in these boundary regions, the two different representations will effectively communicate and behave consequently as one single dislocation structure. We call this strategy the *application of reciprocal boundary conditions*, and details of this coupling scheme will be discussed in sub-Section 4.2.2.

Second, a smooth transition between MD and DDD is required, which invalidates the detection/passing scheme employed in CADD2d. Such smooth transition allows dislocations traveling in the CADD3d domain with atomistic, hybrid and discrete-line representations depending on their locations. We will achieve this behavior by the strategy called *dislocation-migration scheme* that will be explained in sub-Section 4.2.2.

CADD3d

In the previous section, we have proposed two of the components of the CADD3d coupling scheme: *application of reciprocal boundary conditions* and *dislocation-migration*

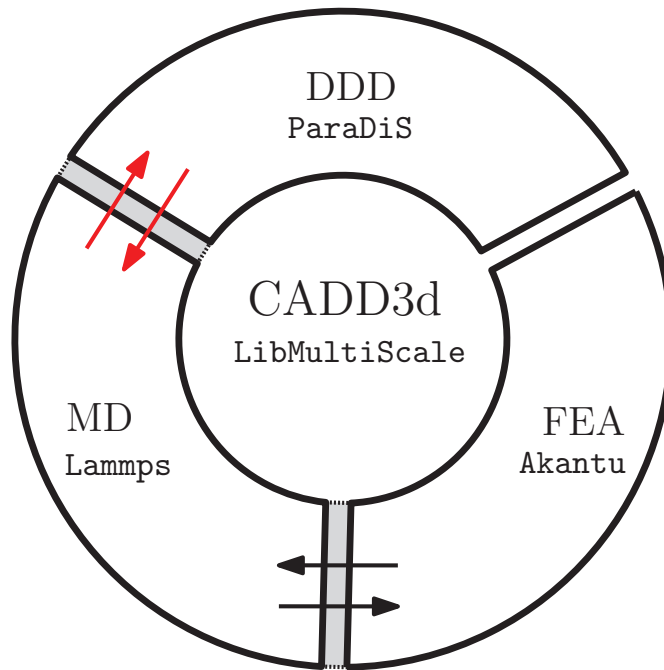


Figure 4.3 – Three simulation engines are plugged-in LibMultiScale, which is currently being maintained and developed in house [Anciaux et al. (2006); LibMultiScale (2006)]. For the molecular dynamics domain, Lammmps, developed by Sandia national laboratory, is chosen [Plimpton (1995); Lammmps (1995)]. The plug-in for the discrete dislocation dynamics domain is ParaDiS, which is maintained by Lawrence Livermore national laboratory [Arsenlis et al. (2007); ParaDiS (2007)]. The last plug-in Akantu is chosen to describe the finite element domain, and is maintained in house [Richart et al. (2010); Akantu (2007)].

scheme. Detailed explanations of these components and the implementation into an open-source software will be given in this section.

Coupling Engine

LibMultiScale is a parallel C++ framework for multiscale coupling simulations [Anciaux et al. (2006)], which is currently being developed and maintained by the Computational Solid Mechanics Laboratory in EPFL [LibMultiScale (2006)]. As shown in Figure 4.3, LibMultiScale currently includes three simulation engines for the three computational domains. Lammmps for molecular dynamics (MD), ParaDiS for discrete dislocation dynamics (DDD) and Akantu for finite element analysis (FEA). By coupling these three software within LibMultiScale, the Concurrent Atomistic/Discrete Dislocations method (CADD) can be realized [Junge (2014)].

The current status of CADD can be summarized as follows: the interface between MD and FEA has been developed recently, and now supports static and dynamics coupling problems [Junge (2014)]. The interface between MD and DDD is the main theme of this thesis, and will be described in details in this chapter. The coupling scheme between DDD and FEA has

not been developed yet, and this can be considered as an objective for the future.

It is worth to mention that the DDD method needs the nodal forces to be computed by taking into account all the other dislocation segments (see equation 3.18). When a MD region replaces several of these segments, their influence on the nodal forces cannot be computed anymore. In the original formulation of CADD2D, this was compensated by the resolution of a linear elastic problem, providing an additional stress field matching the missing forces. In principle CADD3D needs a coupling scheme between DDD and FEA to achieve the DDD nodal force field calculation. To overcome such a limitation, the current CADD3d method is simplified in two points: first, only a constant external shear loading will be considered and second the DDD network needs to be known everywhere, including in the atomic region. The details and implication of these two conditions will be shown in Section 7.2.

Coupling Algorithm

Figure 4.4 shows the detailed CADD3d algorithm where the MD (Lammps) and DDD (ParaDiS) domains are highlighted (red box: MD processors; blue box: DDD processors). More precisely, each of the MD and DDD domains is simply partitioned into sub-domains, and each domain is assigned to a given processor. The parallel computation for each single-scale method is realized thanks to its engine code. Particularly, to support the parallel coupling calculations, the coupling algorithm has to be parallelized, which has been implemented with the message-passing paradigm (MPI) [MPI (1993)].

In turn, the coupling code can be decomposed in eight sub-modules (inside the cyan dashed-dot-lines) as shown in Figure 4.4. These modules are executed after the time integration of the MD and DDD domains. The coupling is called every *update step* (t_{update}) which does not have to be the same as the MD and DDD integration time steps. However, this update step t_{update} should be chosen properly, which will be clarified later. Let us tag the coupling modules from ① to ⑧. We will refer to these numbers while providing the details of the coupling algorithm in following.

Coupling Procedure

During the evolution of the hybrid dislocation, the reciprocal boundary conditions must be maintained such that the two representations behave as a single entity. Figure 4.5 shows how to apply the necessary reciprocal boundary conditions during the gliding motion of a hybrid straight dislocation. Above a limiting finite shear load the hybrid dislocation will glide. Without any coupling, the interface regions will remain at their positions. This is what happens during an integration time-step before the coupling is actually enforced. Consequently, a hybrid dislocation is first distorted close to the coupling interfaces because the reciprocal boundary conditions are "outdated" as shown in Figure 4.5 (b). At this moment, the update scheme of the reciprocal boundary conditions must be carried out as follows.

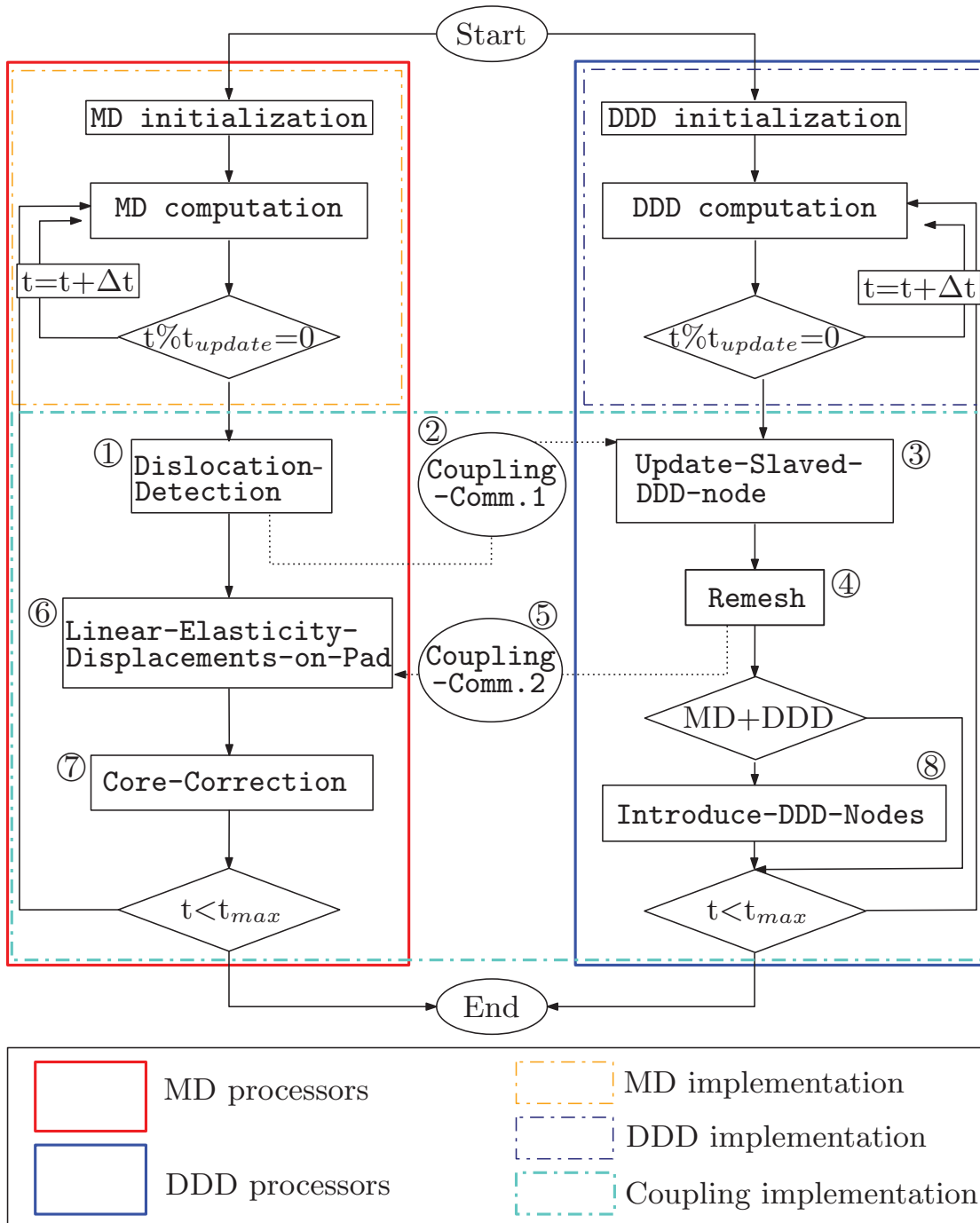


Figure 4.4 – Algorithm of the CADD3d method. MD and DDD processors are shown with the red and blue solid lines, respectively, and their implementation components are surrounded by the orange and the dark-blue dashed lines, respectively. The components of the CADD3d implementation are placed inside the cyan dashed-dot-lines. Each of them are run on processor subsets handling either MD or DDD. The components running on the different processors communicate with each other through the two steps labeled Coupling-Communication 1 and Coupling-Communication 2.

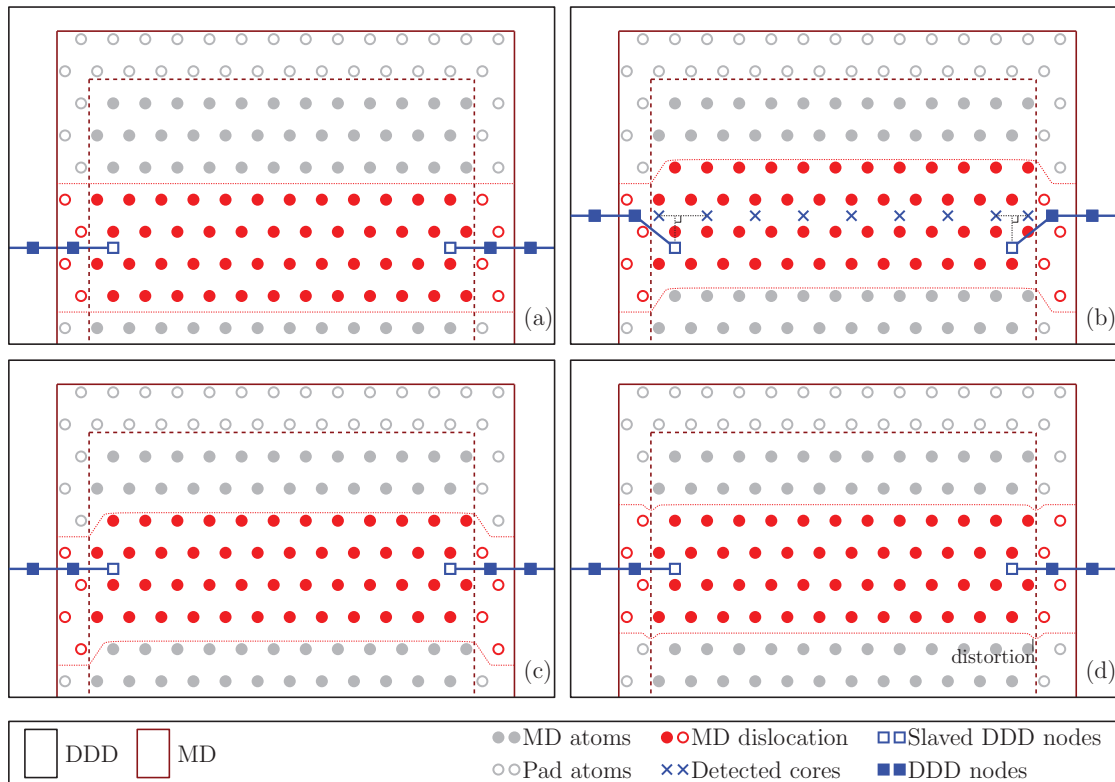


Figure 4.5 – Hybrid straight dislocation dynamics with the update of the reciprocal boundary conditions. (a) At an initial stage, the MD and DDD boundary conditions are consistent with each other. (b) By applying a shear load, the two dislocation sub-parts move, which lead to mismatched boundary conditions. The update of the reciprocal boundary conditions consists of the two steps: (c) update of the slaved DDD nodes and (d) update of the pad atoms.

- ① Dislocation-Detection: First, the MD-sub-part dislocation is analyzed to find the locations of the dislocation cores. One of the most common methods for this task stands on the centro-symmetry criterion which can be employed to distinguish defects from a perfect lattice [Kelchner et al. (1998)]. An alternative method is the Dislocation Extraction Algorithm (DXA) developed by Stukowski and Albe [Stukowski and Albe (2010)]. To employ this approach, the DXA algorithm has been recently implemented by M.L. Hodapp² into LibMultiScale in a more compact and optimized way. The detected dislocation cores are denoted in Figure 4.4 with the blue crosses on the MD sub-part in Figure 4.5 (b).
- ② Coupling-Communication1: The set of coordinates detected is dispatched from MD to DDD. Each MD processor broadcasts its core coordinates to the DDD processors.
- ③ Update-Slaved-DDD-node: Based on the received data, the DDD domain updates their slaved DDD nodes. Currently, we enforce the position of the slaved DDD node between the two closest detected cores. By perpendicularly projecting a straight line onto the

²One of the CADD3d-project members associated in LAMMM, EPFL

segments connecting these two MD cores, the next position of the slave DDD node can be determined as shown in Figure 4.5 (b) with the black dashed lines.

- ④ **Remesh:** After the update of the slaved DDD nodes, the DDD networks may require topological operations (not shown in Figure 4.5). For instance, the updated constrained nodes do not meet the criterion for mesh coarsening. To avoid such situations, a coarsening or refining procedure needs to be performed, and it is usually performed by executing the remesh routines implemented in the ParaDiS engine.
- ⑤ **Coupling-Communication2:** After the remesh, the DDD nodal coordinates and their connectivities are sent to the MD processors. More precisely, all the DDD nodes and their connectivity information, which are distributed over the DDD processors, are gathered in one single DDD processor. Then, this collected data is dispatched to the MD processors meaning that only one DDD processor communicates with all the MD processors.
- ⑥ **Linear-Elasticity-Displacements-on-Pad:** Then, with the received data, the MD processors can compute the displacements of the pad atoms in order to provide a matching boundary condition through the pad region. We employ the Barnett's approach [Barnett (1985); Barnett and Balluffi (2007)] to obtain the linear elasticity displacement solution for the pad atoms. According to the theory, we have to consider the elastic displacement contributions from all the DDD segments for each pad atom, and this total effect can be fulfilled thanks to the DDD data set gathered from the previous module (⑤).
- ⑦ **Core-Correction:** The linear elasticity theory diverges in core structures and thus it is required to correct the analytic displacement field. The additional correction field is evaluated by using the so-called the core template. Therefore, the core template should be prepared in advance by studying dislocation core structures with offline MD. The core template is the first building component, which will be described in details in Chapter 5. After this step, the hybrid dislocation gains the correct boundary conditions as shown in Figure 4.5 (d) matching the MD and DDD sub-parts
- ⑧ **Introduce-DDD-Nodes:** When a MD dislocation (or the MD part of a hybrid dislocation) approaches a pad region as shown in Figure 4.6 (a), a smooth-transition into a DDD dislocation should be realized. It can be achieved by introducing new DDD nodes at the core positions detected from MD. This feature will be clarified below.

These eight steps constitute the coupling algorithm and enforce adequate reciprocal boundary conditions. As already mentioned, it is possible to apply this coupling scheme at a different frequency than the MD/DDD time-integration frequency. Particularly, by choosing a large update step (t_{update}), this can be helpful to save computational time. However, small distortions of the dislocation lines can be observed at the transition from the atomic representation towards the continuum one (a visual guide is provided as an example with the red dashed line

in Figure 4.5 (d)). Such distortions increase when enlarging the update step, and spurious forces may pollute the coupling simulations. Therefore, the update step (t_{update}) has to be chosen carefully, and this trade-off condition will be studied with a benchmark problem in Chapter 7.

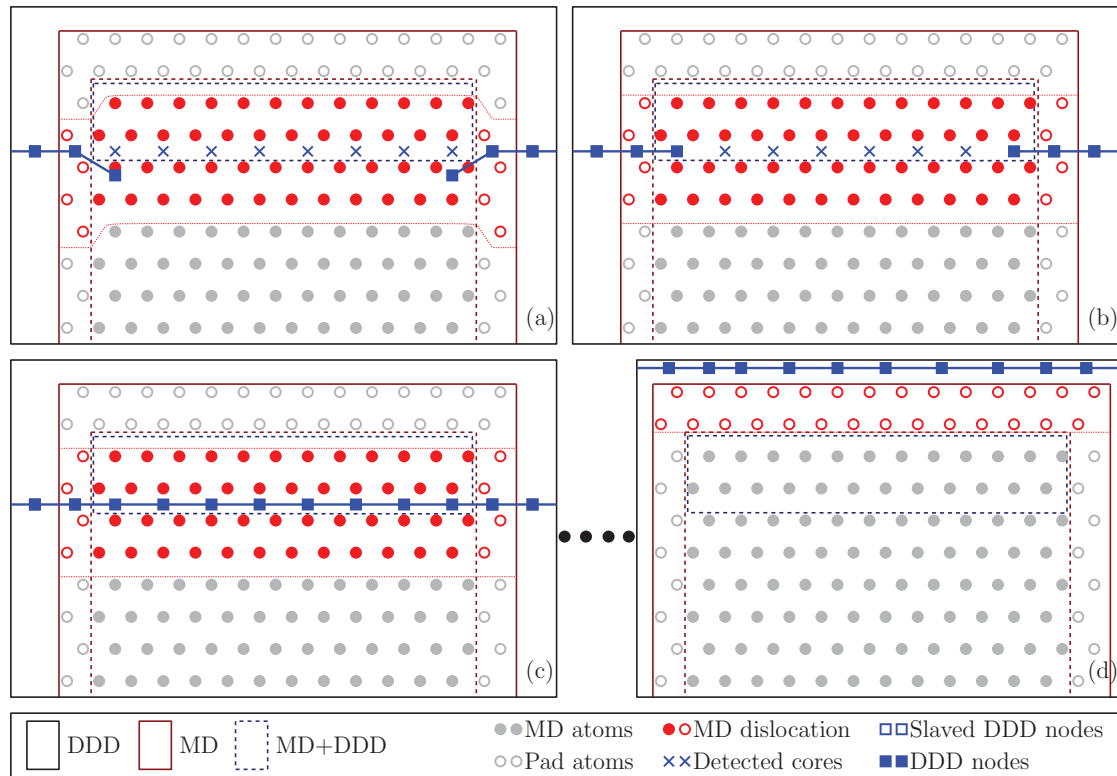


Figure 4.6 – A straight hybrid dislocation approaches the DDD domain. (a) The hybrid dislocation moves forward, and needs to update the boundary conditions of MD and DDD. (b) The reciprocal boundary conditions are updated. The MD sub-part will be completely impeded by the pad atoms in front. (c) To migrate the hybrid dislocation to DDD, new DDD nodes are introduced at the cores in the insertion (MD+DDD) zone. (d) The dislocation escapes the MD domain, and the MD dislocation leaves a step at the outer-surface of the pad region.

Let us discuss in more details the hybrid dislocation migration that was briefly described in the very last coupling step (⑧). Figure 4.6 (a) shows a hybrid straight dislocation approaching the DDD domain. As previously discussed along with Figure 4.5, the reciprocal boundary conditions result in the situation shown in Figure 4.6 (b). In the presented case, a pad region stands in front of the MD sub-part of the hybrid dislocation. If nothing is done, the atomic representation will be impeded by the constrained pad atoms: this prevents the travel into the DDD region. To avoid it, a new DDD node is effectively introduced when the MD dislocation core is near the pad region. To that end, an additional region (the insertion zone) should be defined near the coupling interface as shown in Figure 4.6 with the blue dashed box (MD+DDD). When MD cores are detected in the insertion zone (MD+DDD), the corresponding DDD nodes

Chapter 4. Coupled Atomistic and Discrete Dislocation Method in 3d (CADD3d)

are inserted (in step ⑧) as shown in Figure 4.6 (c). The introduced DDD nodes should travel at the same speed as the MD dislocation thanks to the matching mobility law. With this strategy, the hybrid dislocation can smoothly transform into a DDD dislocation, and escape the pad region as shown in Figure 4.6 (d).

It is worth being noted that this coupling scheme is only valid if the two dislocations travel at the same pace, which relies on an accurate mobility law in the DDD domain. As discussed in Section 3.2.2, a mobility law of FCC dislocations can be defined as a function of a character angle θ and a temperature T [Hirth and Lothe (1992); Cai and Bulatov (2004)], and can be constructed by a MD dislocation mobility study. This will be detailed in Chapter 6.

To summarize, we have given the main steps of the new CADD3d coupling scheme. This method requires three components: the MD dislocation detection, the core templates, and the mobility law. In the next two following chapters (Chapters 5 and 6), the last two components will be evaluated with molecular dynamics, and be analyzed. This new information, which was not previously available in the literature, will be used as input to this novel coupling method.

5 Dislocation Core Structures, Peierls Stresses and Core Templates with Several Character Angles in Aluminum

This chapter is a modified version of the journal paper *Toward a 3D coupled atomistic and discrete dislocation dynamics simulation: dislocation core structures and Peierls stresses with several character angles in FCC Aluminum* published in the *Advanced Modeling and Simulation in Engineering Sciences* on 2015 [Cho et al. (2015)] including a new section (Section 5.6: Generation of Core Templates).

The coupling method proposed in the previous section needs two building components. One of them is the core template, employed to enforce displacement boundary conditions at the coupling interface. In this chapter, we compute this core template by means of molecular dynamics simulations.

This chapter is organized as follows. In Section 5.1, a refined definition of the core template is given. Since the core structure is angle dependent, its evaluation is needed for virtually any character angle. Therefore, in Section 5.2 we provide comprehensive modeling techniques to create a dislocation with a chosen mixed character angle. We also provide an extended variational Peierls -Nabarro (PN) method [Bulatov and Kaxiras (1997)] to validate the obtained MD core structures in Section 5.3. Interestingly, the extended PN method can be used to predict core structures of mixed dislocations which cannot be obtained with MD simulations due to the computational cost. With this successful extension of PN method, we obtain core structures matching MD results, and the analysis of the details of dislocation core structures for all the studied character angles in Section 5.4. We also measure Peierls stresses for various mixed dislocations in Section 5.5, and show that Peierls stresses are largely influenced by the atomistic structures of the dislocation cores. Finally, in Section 5.6, we conclude this chapter by detailing the construction of the core templates from the obtained MD core structures.

Chapter 5. Dislocation Core Structures, Peierls Stresses and Core Templates with Several Character Angles in Aluminum

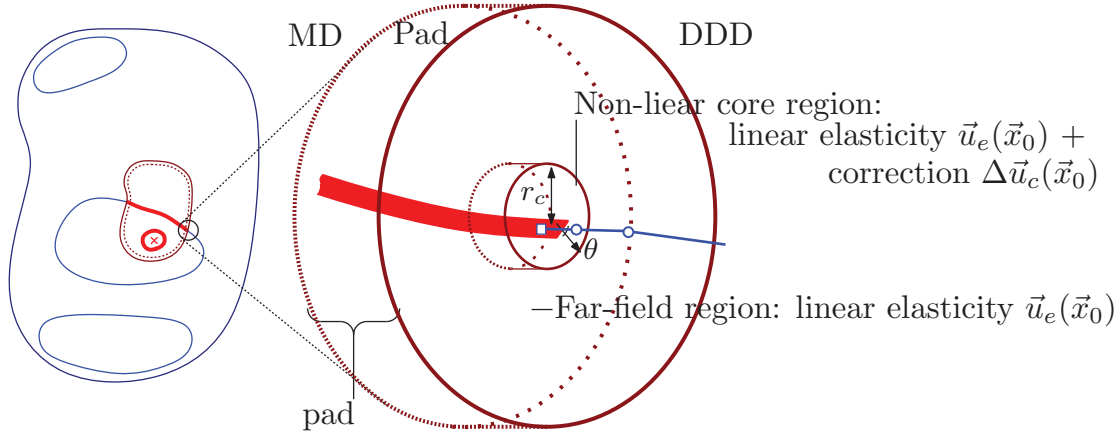


Figure 5.1 – Schematic of a dislocation core in the pad. For most of the pad, the linear elasticity displacement solution \vec{u}_e is adequate. However, in the vicinity of the dislocation line (non-linear core region), it is necessary to add the correction field $\Delta\vec{u}_c$ obtained from the core template to minimize spurious forces.

Core templates

A schematic of the core template principle is shown in Figure 5.1 with a hybrid dislocation consisting of atomistic and discrete dislocations in the MD and DDD domains, respectively. At the interface, the hybrid dislocation consists of the MD and DDD boundary conditions, and they match each other (i.e. respective boundary conditions as discussed in Chapter 4). More precisely, a correction field obtained from the core template is applied inside the nonlinear dislocation core region (defined by a cut-off radius r_c) to correct the diverging nature of the linear elasticity solution.

Such a correction $\Delta\vec{u}_c(\vec{x}_0)$ for an atom with an initial position \vec{x}_0 is the difference between the exact atomistic solution $\vec{u}_A(\vec{x}_0)$ and the prediction provided by linear elasticity $\vec{u}_e(\vec{x}_0)$:

$$\Delta\vec{u}_c(\vec{x}_0) = \vec{u}_A(\vec{x}_0) - \vec{u}_e(\vec{x}_0) = \vec{u}_A(\vec{x}_0) - \sum_j \vec{u}_{e,j}(\vec{x}_0), \quad (5.1)$$

where $\vec{u}_{e,j}$ is the contribution of the j -th discrete dislocation segment to the displacement field. By assuming that the atomistic solution can be split into individual contributions due to the discrete dislocation segments, we obtain this expression:

$$\vec{u}_A(\vec{x}_0) = \sum_j \vec{u}_{A,j}(\vec{x}_0), \quad (5.2)$$

and consequently the correction $\Delta\vec{u}_c$ can be expressed as a sum segment contributions:

$$\Delta\vec{u}_c(\vec{x}_0) = \sum_j \Delta\vec{u}_{c,j}(\vec{x}_0) = \sum_j [\vec{u}_{A,j}(\vec{x}_0) - \vec{u}_{e,j}(\vec{x}_0)]. \quad (5.3)$$

Far from any dislocation core, non-linear effects become negligible, and the small-strain linear

elasticity solution \vec{u}_e converges to the atomic solution \vec{u}_A . Also, the atomistic solution $\vec{u}_{A,j}$ can be approximated in the core region of segment j with the displacement field due to a straight dislocation:

$$\vec{u}_{A,j}(\vec{x}_0) \approx \vec{u}_A^S(\vec{x}_0, \theta_j) \quad \forall \vec{x}_0 \quad s.t. \quad D(\vec{x}_0) \leq r_c \quad (5.4)$$

where $D(\vec{x}_0)$ is the distance to the dislocation line, θ_j is the local character angle of the j -th segment, and \vec{u}_A^S is the displacement of a straight dislocation. This approach is valid only if line curvatures are much less than the considered core radius. Furthermore, the dislocation lines should be far enough from each other to be able to neglect non-linear close-range interactions between dislocations: this constrains the overall density of dislocations. The displacement field around straight dislocations can be obtained by modeling straight dislocations with MD. A rigorous and detailed setup for the atomic modeling of arbitrary mixed and straight dislocations is provided in the following section.

Atomistic Dislocation Modeling

A straight single dislocation, as shown in Figure 5.2, is inserted in the simulation box

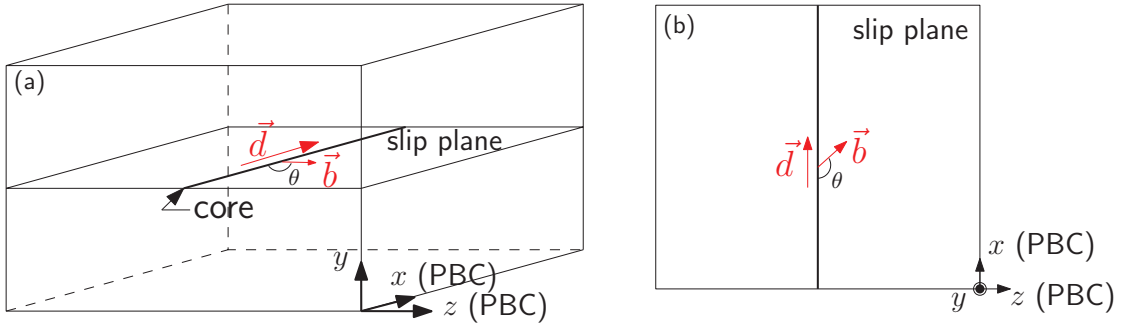


Figure 5.2 – (a) Schematic modeling of a straight dislocation with an arbitrary character angle. (b) Top view of the slip plane. Lattice coordinate in y axis is $[111]$, while the coordinates of x and z axes vary with the character angle θ as shown in Table 5.1.

having periodic boundary conditions (PBC) both in the dislocation gliding (z) and line (x) directions. As shown in Figure 5.2 (b), by setting the character angle θ as an arbitrary value, we can model several mixed dislocations. For an edge (respectively screw) dislocation, the dislocation line direction \vec{d} is defined as perpendicular (respectively parallel) to the slip direction (Burgers vector \vec{b}) on the same slip plane. The edge (90°) and screw (0°) dislocations in FCC are modeled by choosing the dislocation line direction as $\vec{d} = [11\bar{2}]$ for edge and $\vec{d} = [1\bar{1}0]$ for screw with the same Burgers vector $\vec{b} = \frac{1}{2}[1\bar{1}0]$. Therefore, in order to create intermediate angle dislocations ($0^\circ \leq \theta \leq 90^\circ$), one needs to choose the dislocation line direction \vec{d} accordingly. We explain the detailed procedure to find a line direction \vec{d} for a specific angle dislocation as shown in Figure 5.3.

Chapter 5. Dislocation Core Structures, Peierls Stresses and Core Templates with Several Character Angles in Aluminum

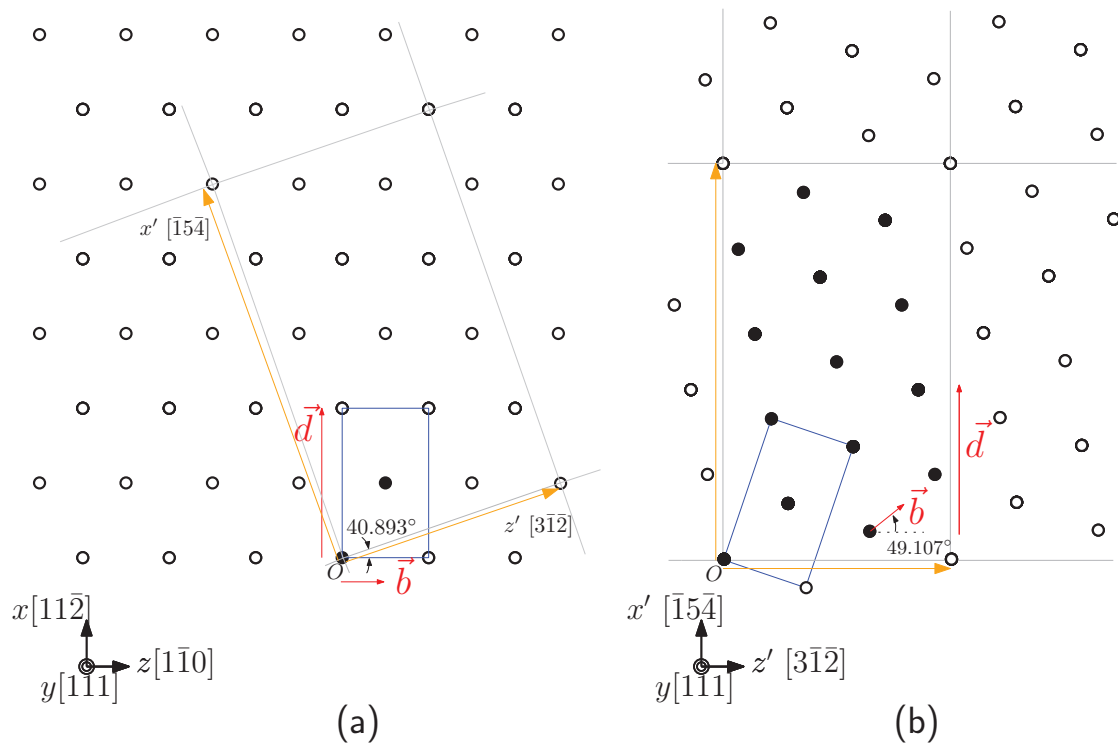


Figure 5.3 – (a) Procedure to find lattice coordinates for a mixed dislocation based on the atomistic representation used for edge dislocation ($x = [11\bar{2}]$, $y = [111]$ and $z = [1\bar{1}0]$). (b) Result of the procedure ($x'[\bar{1}54]$, $y = [111]$ and $z' = [3\bar{1}2]$). The 49.107° mixed dislocation can be created by choosing x' as the dislocation line direction. The full black circles are the minimal number of atoms under the given coordinate system, and empty black circles are the result of replications.

The empty/full circles in Figure 5.3 (a) are atomistic positions in the slip plane (111). The full circles represent atoms contained in a chosen periodic unit cell, and its replications in x and z directions generates the other atoms as empty circles. We select one atom in the unit cell as a reference point O . Then, one of the neighboring atoms of O indicated by the orange color arrow is chosen as shown in Figure 5.3 (a), which can be used to construct the direction $z' = [3\bar{1}\bar{2}]$ by connecting it to O . The cross product of the $y[111]$ and $z'[3\bar{1}\bar{2}]$ directions gives the remaining lattice coordinate $x'[\bar{1}5\bar{4}]$ indicated by another orange arrow. Atomistic positions constructed using the new lattice coordinate system (x' , y and z') are shown in Figure 5.3 (b). By choosing the dislocation line in x' direction with Burgers vector ($\vec{b} = \frac{1}{2}[110]$), a mixed (49.107°) dislocation can be modeled. Other neighboring atoms, defining other z' axes, provide lattice coordinates and associated angles for other mixed dislocations. In this study, we have chosen eight representative cases which are presented in Table 5.1. It shows that the sizes of minimum periodic unit cells vary with the character angles. For example, the 90° (edge) dislocation has the periodic unit cell with dimensions $D_X = \sqrt{6}a$, $D_Y = \sqrt{3}a$ and $D_Z = \sqrt{2}a$, while the size of the unit cell of the 49.107° (mixed) dislocation is $D_X = \sqrt{42}a$, $D_Y = \sqrt{3}a$ and $D_Z = \sqrt{14}a$ with $a = 4.056\text{\AA}$ (the lattice constant). Therefore, the number of replicas need to be carefully chosen to balance evenly the number of atoms and the length of the simulation box with respect to the desired character angle.

In order to insert a dislocation with a Burgers vector $\vec{b} = \frac{1}{2}[1\bar{1}0]$, we employ the edge and screw Volterra displacement fields (u_x^0 , u_y^0 and u_z^0) given by [Hirth and Lothe (1992)]

$$\begin{aligned} u_x^0(z, y) &= \frac{|\vec{b}|}{2\pi} \arctan \frac{y}{z}, \\ u_y^0(z, y) &= -\frac{|\vec{b}|}{2\pi} \left(\frac{1-2\nu}{4(1-\nu)} \ln(z^2 + y^2) + \frac{z^2 - y^2}{4(1-\nu)(z^2 + y^2)} \right), \\ u_z^0(z, y) &= \frac{|\vec{b}|}{2\pi} \left(\arctan \frac{y}{z} + \frac{zy}{2(1-\nu)(z^2 + y^2)} \right) \end{aligned} \quad (5.5)$$

θ ($^\circ$)	x	y	z	Replicas (x, y, z)	Atoms
90 (edge)	$[11\bar{2}]$	$[111]$	$[1\bar{1}0]$	(6, 10, 60)	86040
70.893	$[14\bar{5}]$	$[111]$	$[3\bar{2}\bar{1}]$	(2, 10, 20)	66900
60	$[01\bar{1}]$	$[111]$	$[2\bar{1}\bar{1}]$	(10,10, 30)	71700
49.107	$[\bar{1}5\bar{4}]$	$[111]$	$[3\bar{1}\bar{2}]$	(2, 10, 20)	66960
40.893	$[\bar{1}3\bar{2}]$	$[111]$	$[5\bar{1}\bar{4}]$	(4, 10, 12)	80400
30	$[\bar{1}2\bar{1}]$	$[111]$	$[10\bar{1}]$	(6, 10, 60)	86220
19.107	$[\bar{2}3\bar{1}]$	$[111]$	$[41\bar{5}]$	(4, 10, 12)	80520
0 (screw)	$[\bar{1}10]$	$[111]$	$[11\bar{2}]$	(10,10, 30)	72000

Table 5.1 – Selected eight angles, lattice coordinates, number of replicas and atoms of each simulation box.

Chapter 5. Dislocation Core Structures, Peierls Stresses and Core Templates with Several Character Angles in Aluminum

where ν is Poisson's ratio of the material. For a mixed dislocation, the displacements (u_x^0 , u_y^0 and u_z^0) are rotated by the character angle θ as

$$\begin{aligned} \vec{u}_{\text{total}}(z, y) &= (u_x, u_y, u_z) \text{ with} \\ u_x(z, y) &= u_x^0(z, y) \cos \theta, \\ u_y(z, y) &= u_y^0(z, y) \sin \theta, \\ u_z(z, y) &= u_z^0(z, y) \sin \theta. \end{aligned} \tag{5.6}$$

The rotated total displacement \vec{u}_{total} is imposed on the perfect crystal. Figure 5.4 shows the change of simulation box after imposing the displacement. The boxes before and after imposing the fields are represented by the gray dot and black solid (dashed) lines respectively. In order to create a straight boundary on the left side of the simulation box in direction z , image dislocations are inserted additionally on the other side of z direction. The right side of the simulation box violates the PBC in direction z . This violation can be simply fixed by two additional geometric treatments. First, the step created by the edge displacement fields

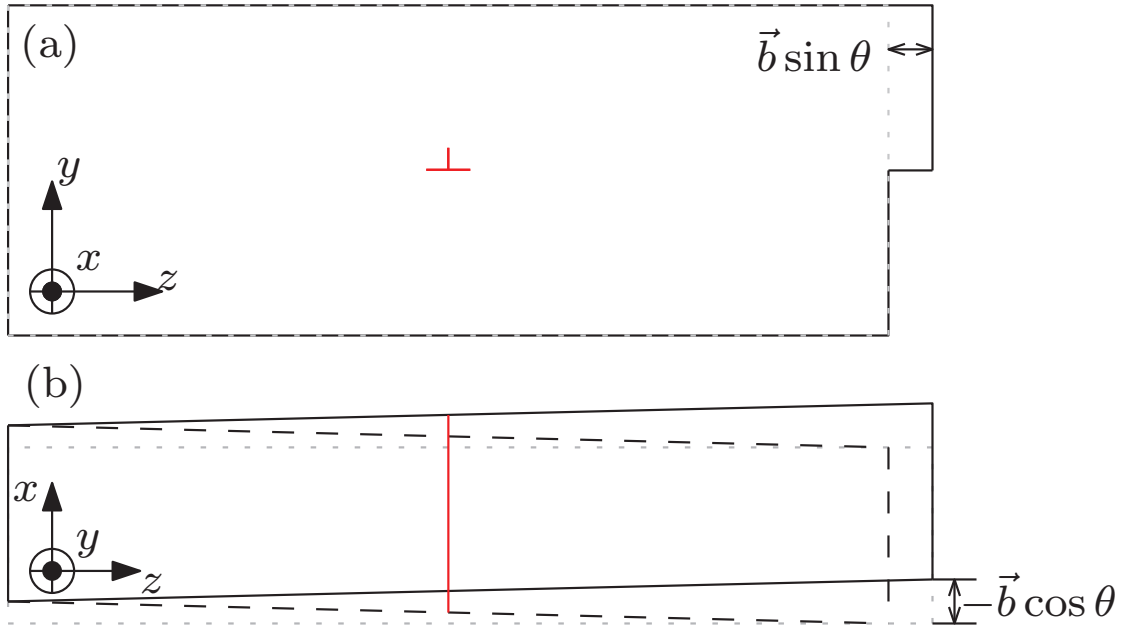


Figure 5.4 – Deformation of the simulation box after imposing the Volterra fields. (a) front view and (b) top view. The initial configuration is denoted by the gray dot lines, and the box after inserting the dislocation is described with the black solid lines. The dashed black lines in (b) are the boundary of the bottom side in the y direction.

(u_y and u_z) can be avoided by removing the extra plane (a slab of length $\vec{b} \sin \theta$). Second, as seen in 5.4(b), the opposite boundaries in direction z mismatch each other by half of the

screw Burgers vector $\vec{b}/2 \cos\theta$. The dashed black lines are the boundaries of the bottom surface. This mismatch created by the screw displacement field (u_z) is fixed by tilting the simulation box with respect to the y axis in the x direction by half of the corresponding screw component $-\vec{b}/2 \cos\theta$. Consequently, the PBC in the z direction is satisfied without any change of the original elastic displacement field. Finally, the surfaces in the y direction remain free boundaries.

In order to find the equilibrium state of dislocation core structures, the simulation box has to be relaxed. We choose the latest Aluminum EAM potential (Mendelev et al. Mendelev et al. (2008)) to evaluate the inter-atomic forces. The comparison of this potential with other EAM ones will be described in Section 5.3. We relax by using a quenching process which is stopped when a norm of forces of all the atoms is below 10^{-10} eV/\AA .

Atomistic structures resulting from the relaxation are shown in Figure 5.5 for the cases of 90° and 49.107° dislocations. The atoms are colored by the y coordinates (normal to the slip plane). The initial dislocation line is dissociated into two partial dislocations. After the dissociation, the regions far away from the dislocation core show the red (A) \rightarrow yellow (B) \rightarrow cyan (C) \rightarrow blue (A) color sequence while the area around the dislocation core shows the red (A) \rightarrow yellow (B) \rightarrow blue (A)¹ color sequence. The modified stacking sequence is known as a stacking fault between two Shockley partial dislocations [Hirth and Lothe (1992)] (indicated by the black arrows in the right side of Figure 5.5). These partials have dissociated from a perfect dislocation ($\vec{b} = \frac{1}{2}[1\bar{1}0] = \vec{b}_1 + \vec{b}_2$ with $\vec{b}_1 = \frac{1}{6}[1\bar{2}1]$ and $\vec{b}_2 = \frac{1}{6}[2\bar{1}\bar{1}]$) due to the energy landscape of the FCC structure. We can see that the stacking fault width for the 49.107° dislocation is smaller than for the 90° (edge) dislocation. Furthermore, the two partials are symmetric in the case of the edge dislocation, but not for intermediate (49.107°) dislocations. In order to understand and validate these relaxed core structures, the variational Peierls -Nabarro model, describing dislocation core structures with a continuum representation, is used in the next section.

Method: Variational Peierls -Nabarro Method

Continuum theory of linear elasticity provides useful analytic solutions for dislocation problems because the theory offers quite accurate dislocation structures when far from the core. However, this theory cannot be employed anymore near the dislocation center, where one finds highly distorted atomistic structures. These nonlinear atomic interactions can be naturally captured by an atomistic model. For these reasons, simulations combining the continuum and atomistic models can be useful not only for the far field but also for the dislocation center. One of the available tools combining the continuum and atomistic models is the variational Peierls -Nabarro (PN) method [Burgers (1940); Nabarro (1947)], which generally has been used to calculate dislocation core structures by minimizing the total energy

¹The stacking fault sequence of the dislocation core region (A \rightarrow B \rightarrow A) allows us to see the second layer of A atoms. These atoms are not seen in the stacking sequence of perfect FCC crystal systems (A \rightarrow B \rightarrow C \rightarrow A).

Chapter 5. Dislocation Core Structures, Peierls Stresses and Core Templates with Several Character Angles in Aluminum

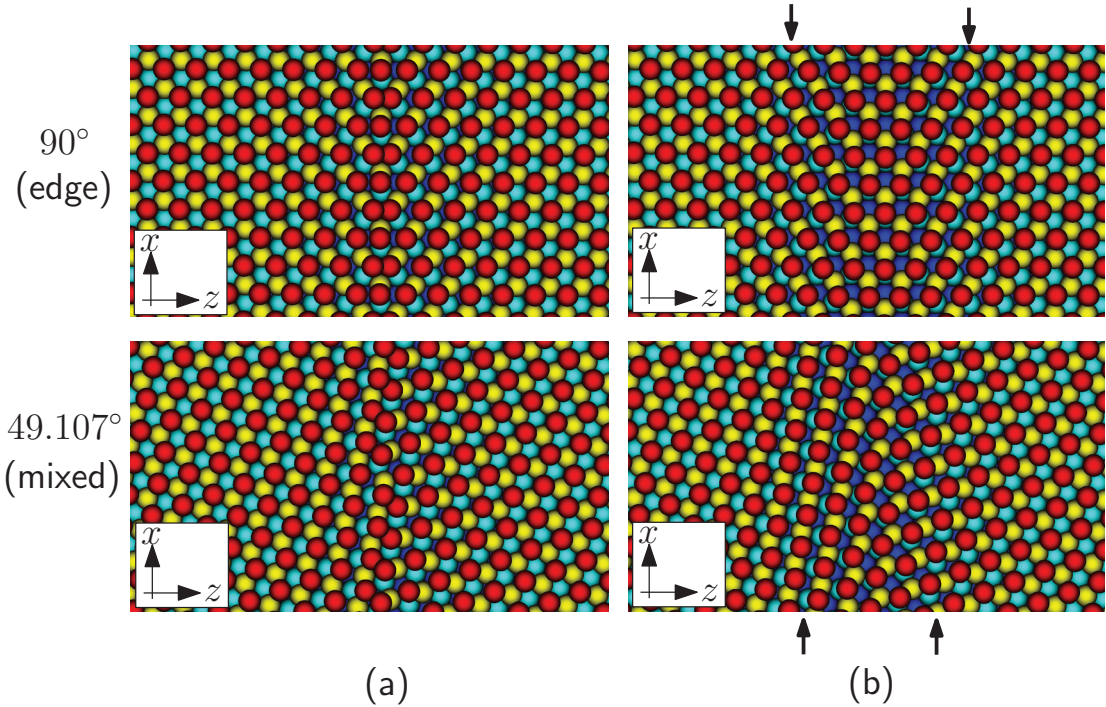


Figure 5.5 – Atomistic structure of the edge (90°) and mixed (49.107°) dislocation in FCC Al. (a) compact core structures after imposing the Volterra field / before the relaxation. (b) core structures after relaxations. The atoms are colored by coordinates of the y axis. Red, yellow, cyan, and blue atoms are placed on top, 2nd, 3rd and 4th layers in the y axis from the slip plane. The initial compact dislocation lines dissociate into two Shockley partial dislocation lines indicated by the black arrows.

of the system. More precisely, the energy in the far field is captured by the energy formulation of continuum linear elasticity theory, while the energy in the core region is obtained by using the crystalline misfit energy and a spread displacement field on the slip plane. The total energy is the sum of both these energy formulations, and the optimal dislocation core structures are found when the total energy is minimum. The PN model is known as a tool providing good descriptions of dislocation core structures in comparison with MD results [Bulatov and Cai (2006); Bulatov and Kaxiras (1997); Schoeck (2012); Hunter et al. (2011); Ngan (1997)].

The original PN formulation starts from the total energy E_{tot} :

$$E_{\text{tot}} = E_{\text{el}} + E_{\text{msft}},$$

where E_{el} is the elastic energy, and E_{msft} is the misfit energy. Because the original Volterra displacement field \vec{u} is singular on the dislocation core, the original energy formulation is ill-posed. Therefore \vec{u} has to be spread, which can be performed in two ways. In a first approach, the displacements are divided into edge u_z and screw u_x components using several arc-tangent functions [Bulatov and Cai (2006); Bulatov and Kaxiras (1997); Schoeck (2012)]. A second method called phase field (PF) method is distributing the displacement \vec{u} into all possible slip directions $u_1 = [0\bar{1}1]$, $u_2 = [10\bar{1}]$ and $u_3 = [\bar{1}10]$ using scalar functions $\zeta(z)$ recording the amount of slips [Hunter et al. (2011); Denoual (2007); Shen and Wang (2003, 2004)]. In this section, we choose the first approach without comparisons between the two methods because the both methods are known to provide sufficiently good dislocation core structures confirming the obtained atomistic simulation results. The two arc-tangent functional forms for both edge u_z^0 and screw u_x^0 displacements as described in [Bulatov and Cai (2006)]:

$$\begin{aligned} u_z^0 &= A_1 \arctan \frac{z - z_1}{c_1} + A_2 \arctan \frac{z - z_2}{c_2} - \frac{b}{2}, \\ u_x^0 &= A_3 \arctan \frac{z - z_1}{c_3} + A_4 \arctan \frac{z - z_4}{c_4} \end{aligned} \quad (5.7)$$

where A_k , c_k and z_k are the parameters obtained through minimization. By the principle of superposition, we rotate u_z^0 and u_x^0 by the character angle θ to have slip and line directions in z and x axes respectively:

$$\begin{aligned} u_z &= \frac{b}{\pi} (u_z^0 \sin \theta - u_x^0 \cos \theta) - \frac{b}{2}, \\ u_x &= \frac{b}{\pi} (u_x^0 \cos \theta + u_z^0 \sin \theta). \end{aligned} \quad (5.8)$$

Chapter 5. Dislocation Core Structures, Peierls Stresses and Core Templates with Several Character Angles in Aluminum

With the arc-tangent shape of displacements in hand (u_z and u_x), we can construct analytically the elastic energy E_{el} :

$$E_{el} = -K_{edge} \int_{-\infty}^{\infty} \int_{-\infty}^{\infty} \frac{du_z}{dz} \frac{du_z}{dz'} \ln|z-z'| dz dz' - K_{screw} \int_{-\infty}^{\infty} \int_{-\infty}^{\infty} \frac{du_x}{dz} \frac{du_x}{dz'} \ln|z-z'| dz dz' \quad (5.9)$$

where $K_{edge} = \mu/(4\pi(1-\nu))$, $K_{screw} = \mu/4\pi$.

The misfit energy E_{msft} can be constructed by using Equation (5.10) with the γ -surface $\gamma(u_z, u_x)$ obtained from independent MD simulations. The γ -surface are computed by constant and rigid shifting of two crystals on the glide plane (111) against each other [Zimmerman et al. (2000)]. The results of γ -surface of Mendelev et al. [Mendelev et al. (2008)] potential is shown in Figure 5.6(a).

$$E_{msft} = - \int_{-\infty}^{\infty} \gamma(u_z(z), u_x(z)) dz \quad (5.10)$$

For a dislocation in FCC materials, the generalized stacking fault (GSF) energy curve in $x = \langle 11\bar{2} \rangle$ directions is important to understand dislocation slip behaviors. The GSF energy curve was first suggested by Vitek [Vitek (1968)] to be composed of an intrinsic stacking fault energy γ_I (ISF) and an unstable stacking fault energy γ_U (USF) [Hunter et al. (2011); Swygenhoven et al. (2004)]. The ISF energy is the local energy minimum of partial dislocations, and the USF energy is the minimum energy required in order to translate partials. The obtained GSF energy curve in $x = \langle 11\bar{2} \rangle$ is given in Figure 5.6 (b) with $\gamma_U = 243.3 mJ/m^2$ and $\gamma_I = 128.6 mJ/m^2$. When compared DFT computations and Mishin & Farkas, our selected Mendelev et al. potential provides an accurate description of γ_U and γ_I .

After constructing the total energy formulation, one can see that the only difference between the arbitrary character angles is the amount of elastic energy E_{el} given by the terms K_{edge} and K_{screw} (see Equation 5.9), which differ by $1/(1-\nu)$: the dislocations close to edge have larger elastic energies than the dislocations around screw. The total energy E_{tot} is minimized numerically to get the optimal shape of the displacement fields \vec{u} over the slip plane.

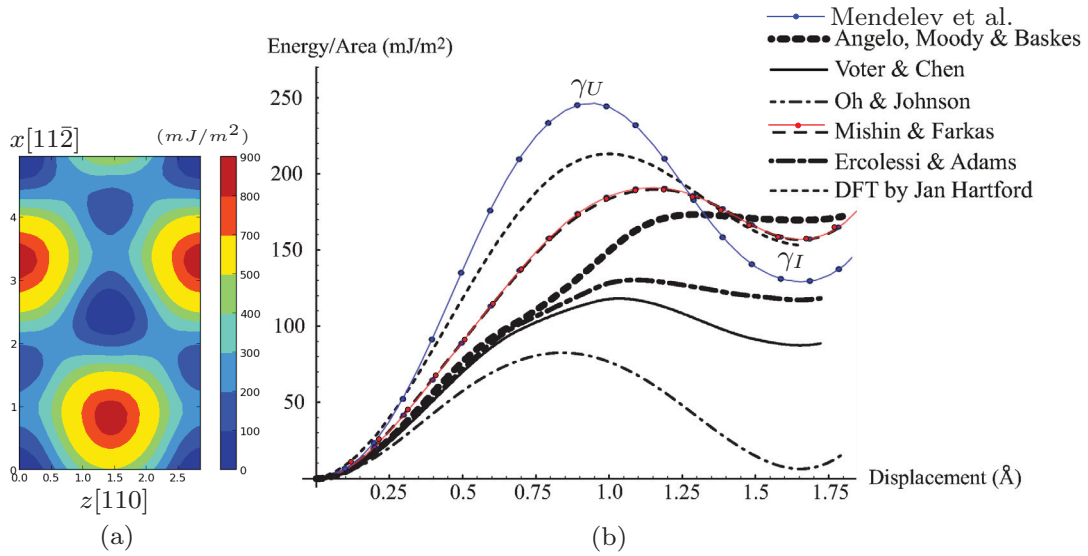


Figure 5.6 – (a) Periodic γ -surface in the x and z directions of the Mendeleev et al. EAM potential [Mendeleev et al. (2008)]. (b) GSF energy curves in $\langle 112 \rangle$ direction of several Al EAM potentials [Angelo et al. (1995); Voter and Chen (1987); Oh and Johnson (1988); Mishin et al. (1999)] and DFT computations Hartford et al. (1998)(figure was taken with agreement of copyright by author [Zimmerman et al. (2000); Ercolessi and Adams (1994)] and IOP publishing). The blue curve shows results obtained with the Mendeleev et al. potential [Mendeleev et al. (2008)]. We reproduce one of author's results shown by the red curve with Mishin and Farkas potential [Mishin et al. (1999)].

Results and Discussion: Comparison between the MD and PN Models Core Structures

By dumping the displacements of all atoms located on the upper and lower slip planes in the MD simulation, we can compare the displacements $\vec{u} = (u_x, u_z)$ with the PN results as shown in Figure 5.7. The MD results are represented with markers while the PN results are described by lines. Clearly, the PN model predicts well the atomistic dislocation core structures. The edge (90°) dislocation is decomposed into the two symmetric Shockley edge and screw partial dislocations. As the angle increases, the partial displacements are no longer symmetric to each other, and finally become symmetric again at the angle of screw dislocation (0°). The

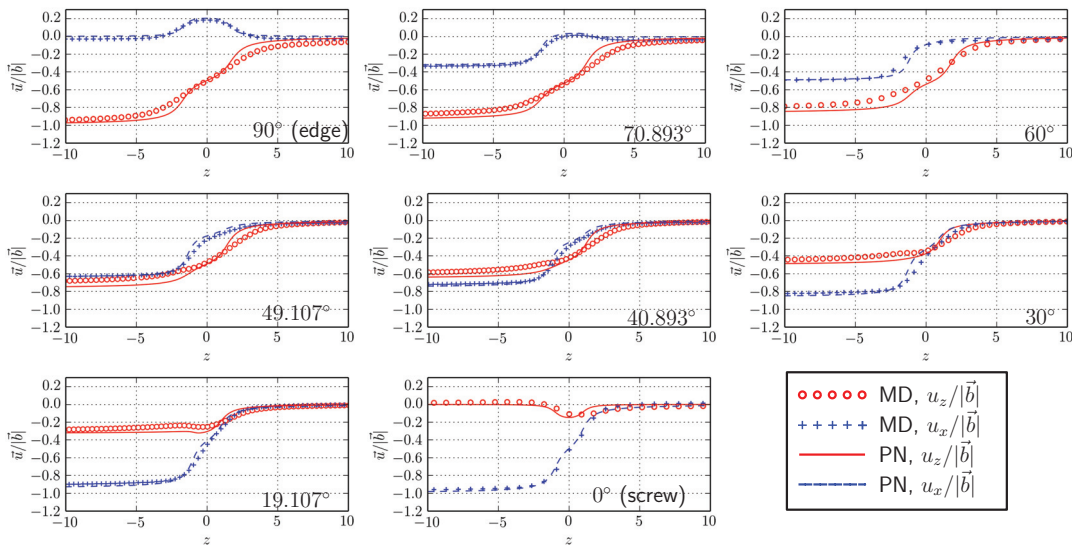


Figure 5.7 – The displacements u_z (edge direction), u_x (screw direction) over the z coordinate (normalized by Burgers vector length) obtained from MD and PN methods for different character angles (some MD atoms are excluded for better visibility).

mapping of PN results onto the perfect atoms located on the slip plane is shown in Figure 5.8 with blue crosses in the case of 49.107° dislocations. The equilibrium state of atomistic core structures is represented in red circles. Again, both results are in good agreement in the core region.

Next, we compare the strains with respect to z coordinates ($d\vec{u}/dz$) as shown in Figure 5.9. While the strains for the PN results can be derived analytically since the displacements are represented by the two arc-tan functions, the strains for the MD results are obtained by computing the slope between two neighboring points without any line interpolation. We define the stacking fault width as the distance between the strain extremes, thus providing a way to measure the widths as function of the different angles (see Figure 5.10). The width for the edge dislocation is $l = 3.4|\vec{b}|$, and it is in reasonable range ($2.8 \leq l \leq 13.4$) when compared to results obtained from other simulations and potentials [Mishin et al. (1999); Hunter et al.

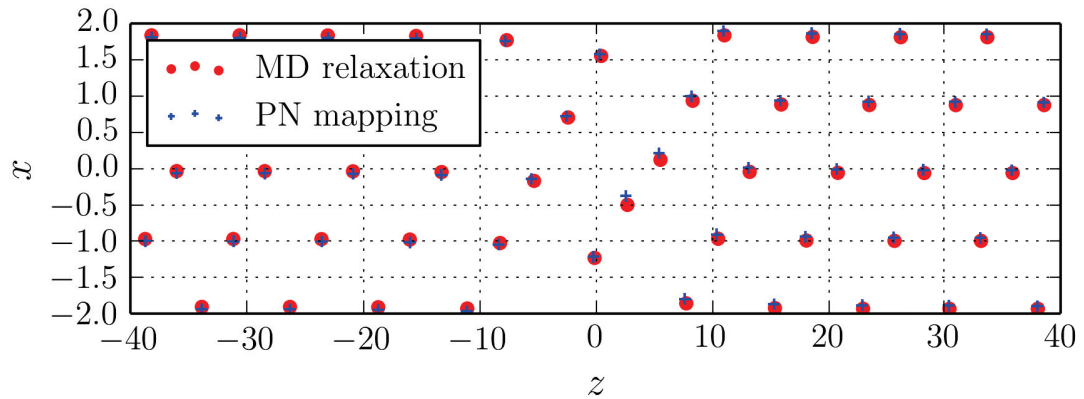


Figure 5.8 – Comparison between MD with PN results with atomistic representation on the slip plane (49.107° mixed dislocation).

(2013); Kuksin et al. (2008); Srinivasan et al. (2005)]. As the angle increases to screw dislocation (0°), the width decreases smoothly. It can be understood due to the decrease of the elastic energy with increasing angle.

We see that the extended PN method produces dislocation core structures, at much cheaper computational costs, that compare reasonably well with the atomistic core structures. Therefore, we can employ the PN method to predict core structures of mixed dislocations which cannot be obtained by atomistic simulations when the sizes of unit cells become large enough to exclude an atomistic calculation.

Peierls Stresses

The Peierls stress is defined as the minimum stress required to translate a dislocation at zero temperature [Hirth and Lothe (1992)], and it is known to be influenced by core structures [Cai et al. (2004); Olmsted et al. (2001); Shin and Carter (2013); Srinivasan et al. (2005); Simmons et al. (1997)]. Because we have obtained the details of the dislocation core structures e.g., lattice orientation and stacking fault widths, the influences of the core structures on the Peierls stress can be studied in this section. Several articles [Olmsted et al. (2001); Shin and Carter (2013); Srinivasan et al. (2005)] have been published regarding the Peierls stresses of FCC Aluminum, measured using direct atomistic simulations. A wide range of results (1 – 13MPa for an edge and 1 – 82MPa for a screw) is observed. Shin and Carter [Shin and Carter (2013)] found that a dislocation dissociated into partials has a smaller Peierls stress than a compact dislocation. Olmsted et al. [Olmsted et al. (2001)] studied Peierls stresses for mixed dislocations (60° and 30°) including the edge and screw character angles. They found that the screw and 60° dislocations are required to overcome a higher Peierls energy barrier than the edge and 30° dislocations. They argued that such results are due to the density of atoms in the motion

Chapter 5. Dislocation Core Structures, Peierls Stresses and Core Templates with Several Character Angles in Aluminum

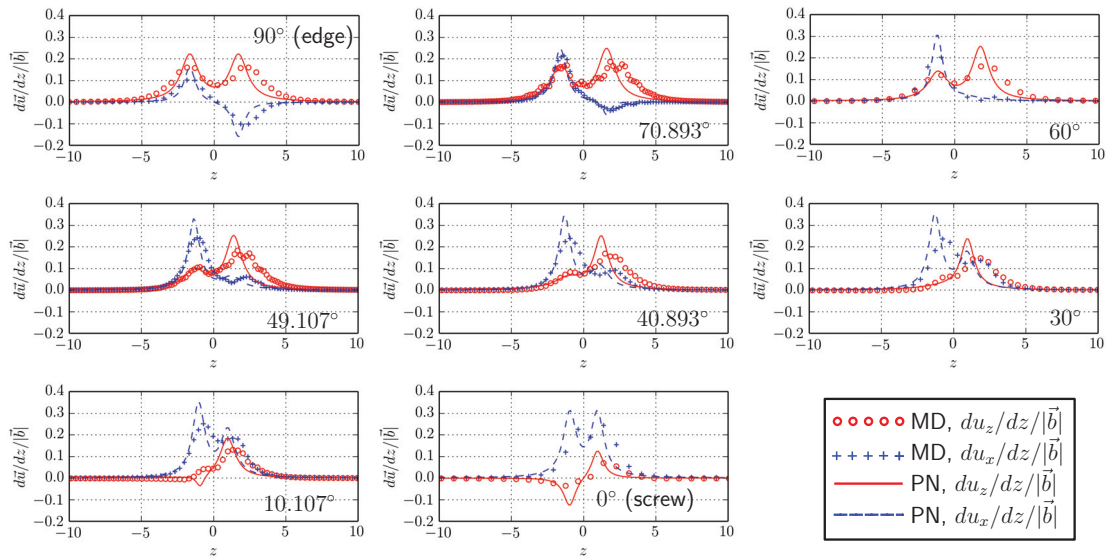


Figure 5.9 – The strains (du_z/dz and du_x/dz) along z axis (normalized by Burgers vector length) measured by MD and PN for the representative eight angles.

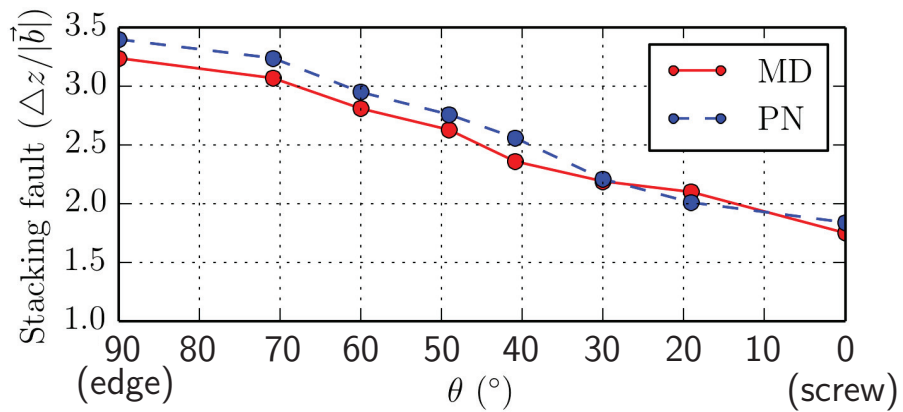


Figure 5.10 – Variation of stacking fault widths for the eight angles.

direction (Simmons et al. [Simmons et al. (1997)] initially suggested this idea). To the best of our knowledge, Peierls stresses have been studied only for the four character angles (90° , 60° , 30° and 0°), whereas we selected other new character angles.

In Section 5.2, we constructed the dislocations based on the corresponding Volterra displacement fields followed by relaxations. These relaxed fields are only valid when dislocations locate at initial positions. As the dislocations change their positions on the gliding plane, the following stresses are polluted by the artificial image stresses from the unmatched dislocation surrounding fields [Olmsted et al. (2001)]. In order to avoid the unwanted effects from the boundaries, we imposed linear displacement fields ($u_{x,\text{lin}}$, $u_{y,\text{lin}}$ and $u_{z,\text{lin}}$) on the atoms in the top and bottom surfaces instead of the Volterra elasticity solution. By introducing these linear fields, the boundary conditions are invariant with respect to the dislocation position. The linear displacement fields for the top and bottom surfaces are chosen as follows:

$$\begin{aligned} u_{x,\text{lin}}^0(z, y) &= \frac{-\text{sign}(y)b_{\text{screw}}/2}{L_Z} \left(z + \frac{L_Z}{2} \right), \\ u_{y,\text{lin}}^0(z, y) &= 0.0, \\ u_{z,\text{lin}}^0(z, y) &= \frac{-\text{sign}(y)b_{\text{edge}}/2}{L_Z} \left(z + \frac{L_Z}{2} \right). \end{aligned} \tag{5.11}$$

with L_Z the length of the simulation box in direction z . On the top surface, the negative Burgers ($-b_{\text{edge}}$ and $-b_{\text{screw}}$) vectors are used, and the positive Burgers ($+b_{\text{edge}}$ and $+b_{\text{screw}}$) are employed for the bottom surface. In order to consider the mixed character angles, the linear displacements are rotated by the given character angle θ (Equation 5.6). The remaining atoms are subjected to the Volterra fields, and are also rotated by θ as we described in Section 5.2. After imposing the various displacement fields on the atoms in each region, we relax the simulation box, and measure the Peierls stress through quasi-static loading. Specifically, we translate the atoms on the top surface along the Burgers direction in small steps, while we fix the atoms on the bottom surface. After each translation, we minimize the bulk of atoms and monitor the final energy value when the minimization finishes. Therefore, we can observe the energy variation of the system as the dislocation moves to different positions along the gliding direction.

Figure 5.11 (a) shows the dislocation displacement u_{dis} in the gliding direction z with respect to the displacements of the top surface u_{top} in the Burgers direction \vec{b} , and the corresponding potential energy variations ΔE_{pot} of the system are given in Figure 5.11 (b). The dislocations slowly change their position, and suddenly jump to the next positions as the quasi-loading is incremented. The jump magnitudes of the edge dislocation are larger than the mixed (40.893°) dislocation. Consequently, the edge dislocation requires higher energy accumulations (and reliefs) before (and after) jumps(respectively) as shown in Figure 5.11 (b)

Chapter 5. Dislocation Core Structures, Peierls Stresses and Core Templates with Several Character Angles in Aluminum

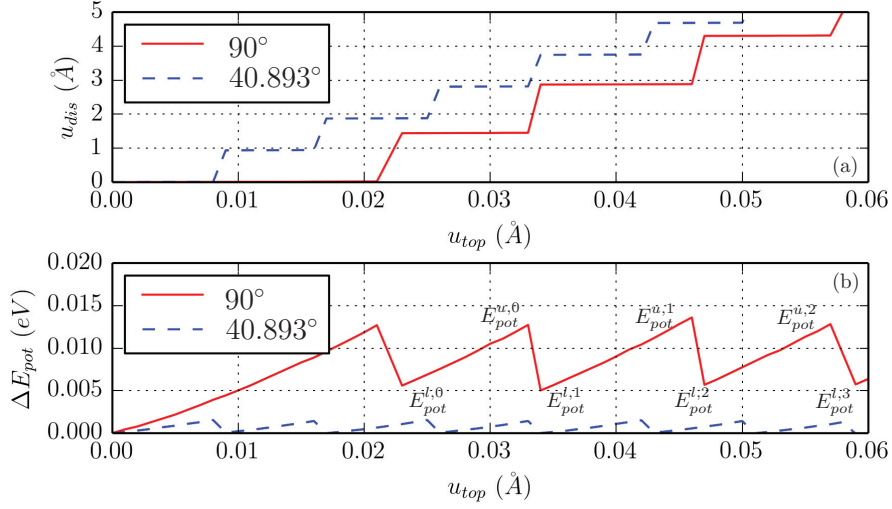


Figure 5.11 – (a) Dislocation displacements and (b) energy variations with respect to top surface displacement of the edge (90°) and mixed (40.893°) dislocation.

than the mixed dislocation. We call each energy relief and peak point E_{pot}^l and E_{pot}^u respectively. The Peierls stress is computed as follows [Cai (2001)]:

$$\sigma_p = \frac{\Delta E_{\text{pot}}^{\text{max}}}{bh_z L_x} = \frac{\max \left\{ \left(E_{\text{pot}}^{u,n-1} - E_{\text{pot}}^{l,n} \right) \mid n \in [1..N] \right\}}{bh_z L_x} \quad (5.12)$$

where L_x is the length of the simulation box in dislocation line direction x and $\Delta E_{\text{pot}}^{\text{max}}$ is the maximum energy release among N events, h_z is the displacement of the dislocation in z direction occurred by one Burgers \vec{b} slip. Cai [Cai (2001)] defined h_z as the repeat distance for which the system is translation invariant, and argued that h_z can be defined geometrically with respect to D_z (length of a primitive unit cell in gliding direction). Since the 90° , 60° , 30° and 0° dislocations were built based on the FCC primitive unit cells, h_z can be defined as $h_z = D_z(90^\circ)/4$ in the case of FCC crystals. For example, h_z is $|\vec{b}|/2$ for 90° and 30° dislocations, and $\sqrt{3}|\vec{b}|$ for 60° and 0° dislocations. These distances are represented in the energy variation curves (Figure 5.11) as follows. The energy of the simulation box containing a edge (90°) dislocation varies with a period $h_z = |\vec{b}|/2 = 1.43\text{\AA}$. Particularly, the other mixed dislocations (70.893° , 49.107° , 40.893° and 19.107°) are constructed based on the periodic unit cells where several primitive unit cells exist (see Figure 5.3). The repeat distances h_z for those angles cannot be defined with respect to the primitive unit cell. Since there are 28 atoms in the given periodic unit cells meaning that 28 energy accumulation-release events happen as a dislocation moves across an entire unit cell. As shown in Figure 5.11, the energy of 40.893° dislocation varies periodically by $h_z = D_z(40.893^\circ)/28 = 0.935\text{\AA}$. Using the corresponding value

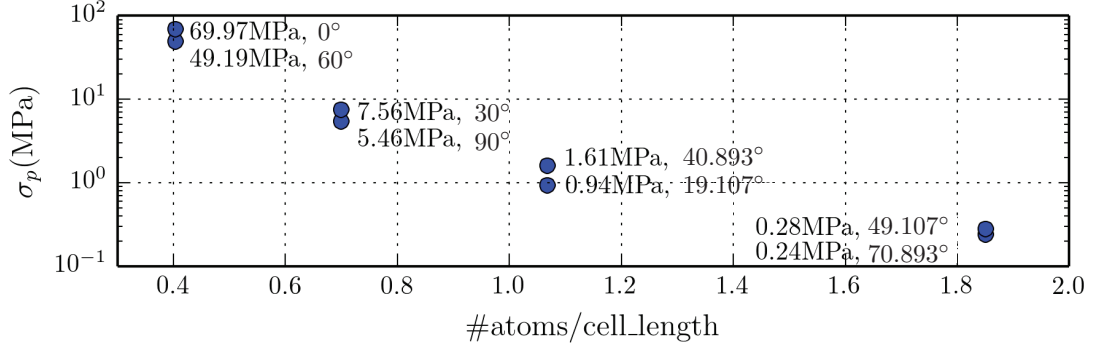


Figure 5.12 – Variation of Peierls stresses for several angles with respect to the density of atoms in the gliding direction. The corresponding Peierls stress value and the character angle are denoted next to each marker.

of h_z ($D_z(\theta)/4$ or $D_z(\theta)/28$), the Peierls stresses of all the character angles can be measured with Equation 5.12. The measured Peierls stresses are shown in Figure 5.12 with respect to the density of atoms in the gliding direction.

We can first compare Peierls stresses of the dislocations constructed with an equivalent lattice orientation (but with a different character angle). As shown in Table 5.1, the edge and 30° , 70.893° and 49.107° , 40.893° and 19.107° , 60° and screw dislocations are modeled based on the same lattice orientation. For each lattice orientation, the Peierls stress decreases low as the character angle decreases. These observations were confirmed by Simmons et al. [Simmons et al. (1997)], and it can be understood with the magnitudes of dislocation dissociation [Shin and Carter (2013)]. As seen in the variation of stacking fault widths in Figure 5.10, the dislocations are dissociated into larger stacking fault widths when their character angles become small. Consequently, the Peierls stress decreases as the character angle reduces. In the case of 40.893° and 19.107° dislocations, the above argument is not valid, and we have not found any reasons for the discrepancy.

Second, we confirm qualitatively the Peierls stresses of the dislocations between the different lattice orientations as follows. The two dislocations (60° and 0°) based on the lattice orientation $x = \langle \bar{1}10 \rangle$, $y = \langle 111 \rangle$ and $z = \langle 11\bar{2} \rangle$ have higher Peierls stresses than the other dislocations. It can be understood with the density of atoms in the gliding direction. We see in Figure 5.12 that the densities vary with the lattice orientations of the slip plane. Therefore, the dislocations built within the same family of lattice orientation having small density have high Peierls stresses. Consequently, the 70.893° and 49.107° dislocations have small Peierls stresses compared to the other dislocations.

Generation of Core Templates

In this section, we generate the core templates from the obtained MD dislocation core structures. According to the definition given in Section 5.1, the core template purpose is to impose the difference (correction) between the fully nonlinear dislocation core structure and the linear elasticity solution. Figure 5.13 shows the error maps $\epsilon(\vec{x}_0)$ of the eight mixed

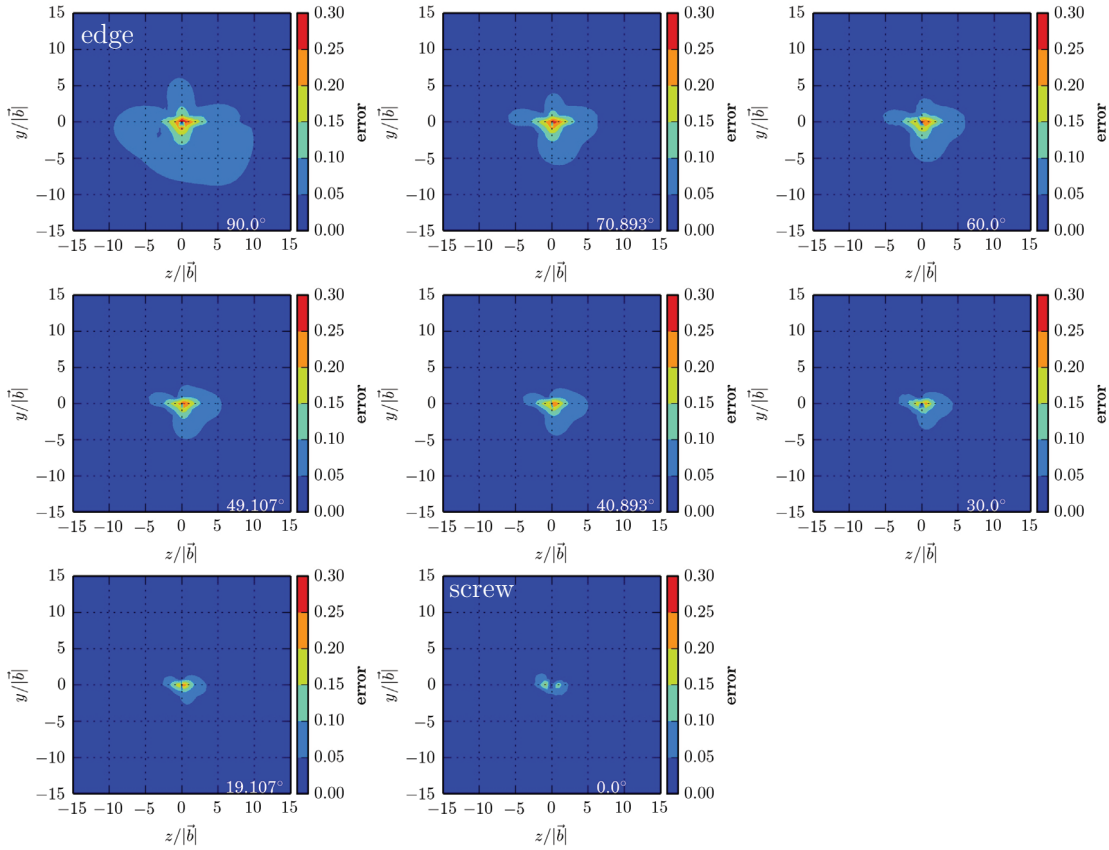


Figure 5.13 – The differences between the atomistic displacements and the linear elasticity displacements around the dislocation cores $(0, 0)$ for the eight character angles.

dislocations, which are evaluated with Equation 5.13, depicted onto the $y-z$ plane, which is normal to the dislocation line (x):

$$\epsilon(\vec{x}_0) = \frac{|\vec{u}_A(\vec{x}_0) - \vec{u}_e(\vec{x}_0)|}{|\vec{b}|} \quad (5.13)$$

with \vec{u}_A the displacement field of the relaxed atoms, and \vec{u}_e the Volterra displacement field.

As expected, the analytic solution fails to predict all displacements due to dislocations

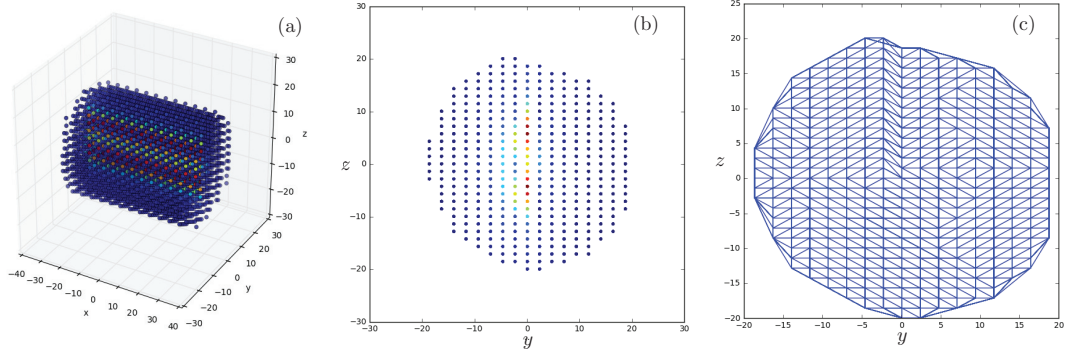


Figure 5.14 – Computation procedure of the core template of the edge 90° dislocation. (a) Atoms around dislocation core. (b) The projected atoms on the y - z plane. (c) Two dimensional mesh, the so-called core template, based on the projected atoms.

when close to the dislocation core. Especially, the radii of the non-linear core regions decrease while increasing the character angle. This feature is consistent with the variation of the stacking fault width shown in Figure 5.10. Since the edge dislocation shows the largest non-linear core region, we can decide the size of the core template as ten times the magnitude of the Burgers vector : $r_c = 10|\vec{b}|$.

A detailed definition of the core template has been recently given by Junge [Junge (2014)]. From this definition, the core template extraction can be summarized as follows. First, the atoms around the core are extracted with the cut-off $r_c = 10|\vec{b}|$ as shown in Figure 5.14 (a). Second, the extracted atoms are projected on the plane normal to the dislocation line x . Third, we construct a two dimensional mesh using a Delaunay triangulation of the projected positions [Preparata and Shamos (1985)] as shown in Figure 5.14 (c). By employing linear shape functions, the correction field can be interpolated [Hughes (1987)] at any point. During the CADD3d simulations, those pre-computed templates are looked up, the corrections are evaluated, and consequently the respective boundary conditions can be accurately imposed.

Let us recall the limitations of the template approach:

- **Dislocation spacing:** it is implicit in the template definition (Equation 5.3) that dislocation lines in the pad are sufficiently separated from one another. If this assumption is violated there will be spurious forces acting in the pad.
- **Dislocation curvature:** since we pre-compute the templates from offline MD calculation with straight dislocations, the local correction that we apply needs to be well approximated. Again, this condition is valid only when the curvatures of dislocation lines in the pad region are much less than the considered core radius r_c .
- **Accuracy and simplicity:** The template is only useful if it can be pre-computed and looked up during the simulation. This means that the displacement field for dislocation

Chapter 5. Dislocation Core Structures, Peierls Stresses and Core Templates with Several Character Angles in Aluminum

core of an arbitrary character angle needs to be interpolated accurately from a finite set of pre-computed straight dislocation cores. With the assumption that core structures continuously vary with the character angles, the dislocation field $\vec{u}_A(\vec{x}_0, \theta)$ of a mixed angle θ can be evaluated with the linear interpolation:

$$\vec{u}_A(\vec{x}_0, \theta) = \frac{\theta - \theta_1}{\theta_2 - \theta_1} \{ \Delta \vec{u}_c(\vec{x}_0, \theta_2) - \Delta \vec{u}_c(\vec{x}_0, \theta_1) \} + \Delta \vec{u}_c(\vec{x}_0, \theta_1) + \vec{u}_e(\vec{x}_0, \theta) \quad (5.14)$$

when $\theta_1 < \theta < \theta_2$

where θ_1 and θ_2 are the closest pre-computed angles and $\Delta \vec{u}_c(\vec{x}_0, \theta_1)$ and $\Delta \vec{u}_c(\vec{x}_0, \theta_2)$ are the core correction fields for the orientations θ_1 and θ_2 respectively.

Summary

In this chapter, we constructed one building component of CADD3d: the so-called core template. It enforces the matching boundary conditions at the pad region through the displacement correction field. To evaluate it, the dislocation core structures of arbitrary character angles were studied with MD simulations. We could verify that a core structure has a stacking fault width decreasing when the character angle increases. A variational PN model was employed to validate the core structures computed with MD. To that end, the general PN method was extended to consider arbitrary angles. This approach can be employed to study any angles, including those that are difficult to obtain with periodic MD simulations due to the computational cost. Thanks to the computed data, the Peierls stresses have been measured, and we found that the magnitude of the dissociation into partials as well as the density of atoms in the gliding direction determine the dislocation Peierls stress. Lastly, we generated the core templates usable in CADD3d from the obtained core structures.

6 Mobility law of dislocations in Aluminum

This chapter is a modified version of the journal paper *Mobility law of dislocations with several character angles and temperatures in FCC Aluminum* accepted in the International Journal of Plasticity in 2016 [Cho et al. (2016)].

The coupling method proposed in the Chapter 4 needs the two building components. One of them is the core template, which was generated in the previous chapter, and the remaining constituent is the mobility law. It is essential to impose the respective boundary conditions at the correct locations defined by the DDD dislocation mobilities.. This can be feasible by employing an accurate-mobility law in the DDD method.

In a pioneering work, Nabarro [Nabarro (1947)] studied dislocation mobility with a continuum approach and showed that dislocations should not propagate at a velocity larger than the shear wave speed. Much below this forbidden velocity, dislocation motions are dragged by a phonon viscous force in a crystal lattice. This drag force is proportional to temperature [Leibfried (1950); Hikata et al. (1971); Gorman et al. (1969)]. Eshelby [Eshelby (1956)] found a distinct supersonic solution to the equation of a dislocation motion and introduced the idea that during motion of a dislocation, both sub-sonic and super-sonic waves can be emitted depending on the dislocation velocity. This mixed-wave dispersion brings another dislocation drag mechanism, which explains how dislocations can loose energy by radiations, besides the phonon viscous force. The transition from phonon-viscous dragging to damping due to dispersive nature happens when the dislocation velocity becomes larger than a critical velocity v_0 . Later, this critical transition-velocity has also been analyzed thanks to lattice dynamics [Atkinson and Cabrera (1965); Ishioka (1973); Ramos de Debiaggi and Caro (1987); Flytzanis et al. (1974)] based on a Frenkel-Kontorowa model [Frenkel and Kontorowa (1938)].

Dislocation mobilities can also be investigated using MD simulations [Kang et al. (2012); Martínez et al. (2008); Olmsted et al. (2005); Bhate et al. (2002)]. For example, Kang et al. Kang et al. (2012) made recently computations of the BCC Peierls limits for various angles to derive a kink-driven mobility law. To the best of our knowledge, direct measurements of mobilities

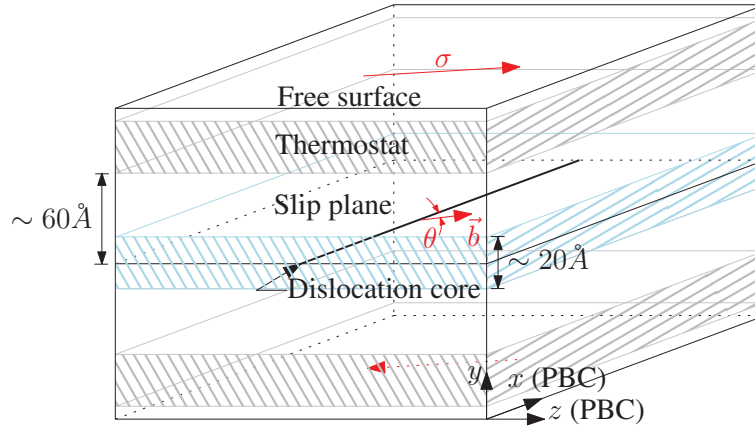


Figure 6.1 – Schematic modeling of a straight dislocation with an arbitrary character angle θ . The length of the simulation box along y axis is $\sim 200\text{\AA}$, while the dimensions along x and z axes vary around 70\AA and 350\AA , respectively, with the lattice orientations determined by the character angle θ [Cho et al. (2015)]. A finite temperature is imposed by Langevin thermostats and a shear stress is applied on the free surfaces in the direction of the Burgers vector $\vec{b} = \frac{1}{2}[1\bar{1}0]$.

with MD remain limited to very few orientations (edge/screw for FCC [Martínez et al. (2008); Olmsted et al. (2005); Bhate et al. (2002)] and screw/M111 for BCC [Kang et al. (2012)]). Indeed, for FCC materials the mobility law employed in DD models is assumed to be a monotonically varying function between the edge and screw dislocation mobilities [Arsenlis et al. (2007); Cai and Bulatov (2004); Zbib et al. (2000)]. However, we will show that it is not the case. This is an important contribution of this chapter, as it is known that the character angle impacts macroscopic plasticity in FCC crystals, for instance through cross-slips [Hirth and Lothe (1992); Martínez et al. (2008); Martínez and Hirth (2014)]. Consequently, having the correct mobilities for multiple orientations is particularly crucial.

This chapter is organized as follows: dislocation mobilities for various mixed angles and temperatures are extracted from atomistic simulations in Section 6.1. In Section 6.2, the obtained mobility results are fitted to an Eshelby-Olmsted [Eshelby (1956); Olmsted et al. (2005)] equation, and the outcome is discussed. In particular, we comment on the origin of one important fitting parameter, called the critical velocity, which identifies a change in the dislocation damping mechanisms. In Section 6.4, we finally construct a mobility law issued from these findings and use it in DDD simulations.

Atomic dislocation modeling

The schematic modeling of a single dislocation is shown in Figure 6.1. At the center of the simulation box, a dislocation with an arbitrary character angle θ is inserted. We choose in total 8-character angles from screw (0°) to edge (90°) dislocations. Periodic boundary

conditions (PBC) are imposed in the dislocation line direction (x) and in the gliding direction (z). The details of the modeling procedures and the character angle selections have been discussed in the previous chapter. We choose the Mendeleev et. al. aluminum EAM/FS potential [Mendeleev et al. (2008)], which describes well the stacking fault energies obtained from DFT calculations [Cho et al. (2015)]. We select three different temperatures $T=100K$, $200K$ and $300K$ by relaxing the atoms using a Langevin thermostat [Schneider and Stoll (1978)]. Furthermore, we also expand the simulation box by 0.26%, 0.48% and 0.7% for the $100K$, $200K$ and $300K$ cases, respectively, during the relaxations in order to correct for pressures due to thermal expansions.

In order to initiate the dislocation motion after the relaxation, a shear loading is applied on the top and bottom free surfaces in the direction of the Burgers vector $\vec{b} = \frac{1}{2}[1\bar{1}0]$. The shear loads have been chosen between 50MPa to 1000MPa. As the shearing occurs, the dislocation glides smoothly on the slip plane and creates heat. In order to keep the system at a constant temperature, Langevin thermostats with a damping constant $\tau = 10000\Delta t$ (10 ps) are used close to the top and bottom surfaces. A large distance (60\AA) separates the thermostat regions from the dislocation core to limit the artificial frictional forces acting on the core region. Consequently, the dislocation can glide in the direction z infinitely (thanks to PBC conditions), while keeping a globally constant the targeted temperature.

Figure 6.2 (a) shows the temperature evolution around the slip plane for the 90° dislocation and for several shear stresses at $100K$. There are fluctuations during dislocation dynamics which decay quickly. When the dislocation stabilizes, the absolute magnitudes of the fluctuations are within 0.1% of the target temperature ($100K$). The temperature imprecision remains within 10% (the maximum is $106K$ for the largest applied stress considered), which is acceptable. Figure 6.2 (b) shows the velocity variations of 49.107° and 90° dislocations for an applied shear stress $\sigma = 300\text{MPa}$ at two different temperatures $T= 100K$ and $300K$. At time $t = 0\text{ps}$, the dislocation escapes the stationary state, and starts to accelerate. At the beginning of gliding ($5\text{ps} < t < 30\text{ps}$), the dislocation dynamics are influenced by waves due to the sudden shear loading applied on the top and bottom surfaces. After 30ps , the dislocation glides at a globally constant velocity. By taking the average values at the steady-state dislocation velocity regimes, the variation of dislocation velocities can be obtained.

The atomistic (virial) stress $\bar{\bar{\sigma}}$ is measured during the dislocation dynamics. The stresses are evaluated in a region of thickness 20\AA around the slip plane (the blue hatching area in Figure 6.1). These measured stresses are projected onto the Burgers vector direction \vec{b} . Finally the reference stress $\bar{\bar{\sigma}}_0$, obtained when the dislocation core is not subjected to any external stress, is subtracted. The magnitude of this stress is an effective stress σ_{eff} defined by the following:

$$\sigma_{eff} = |\bar{\bar{\sigma}} \cdot \vec{b} - \bar{\bar{\sigma}}_0 \cdot \vec{b}| \quad (6.1)$$

The evolution of the effective stresses σ_{eff} is shown in Figure 6.2 (c) for several applied

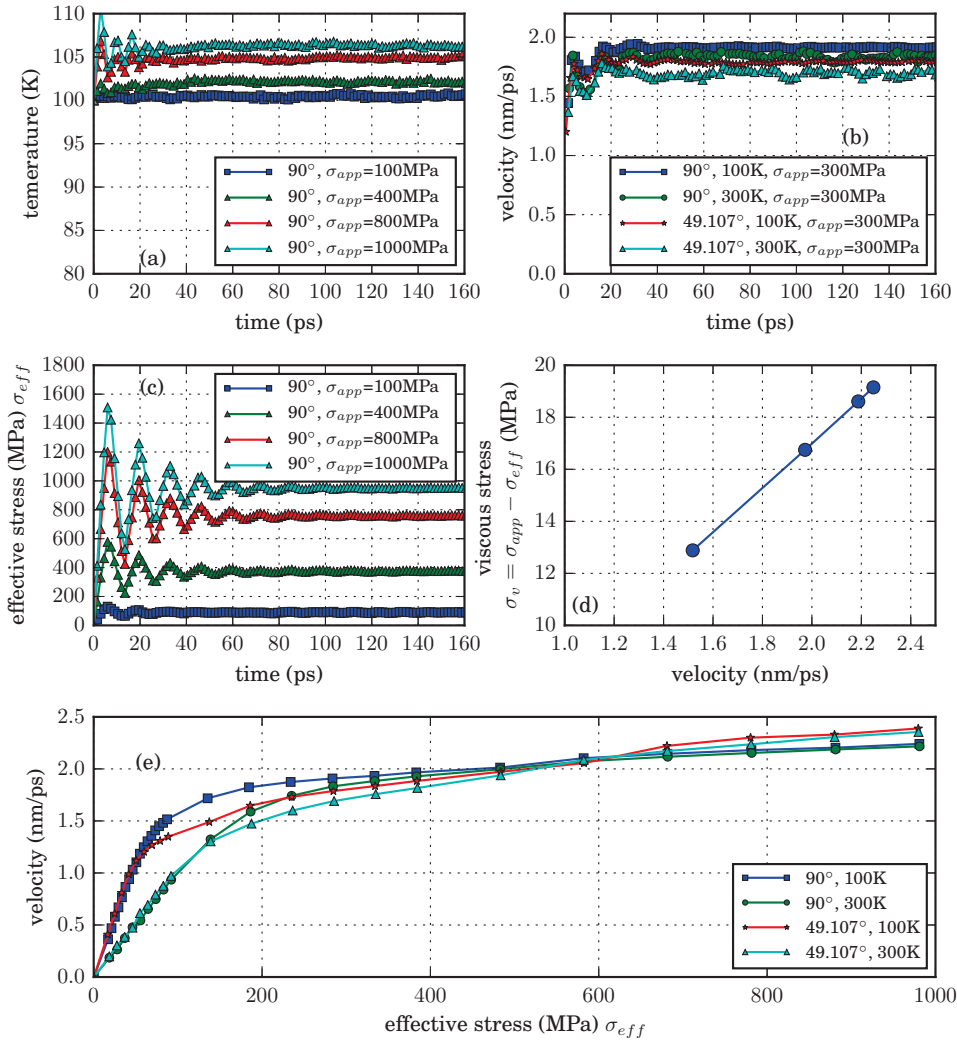


Figure 6.2 – (a) Evolution of temperatures at the vicinity of the slip plane of the edge dislocation with various shear stresses. The target temperature is 100K. (b) Velocity of dislocations (49.107° and 90°) at 100K and 300K under 300MPa. (c) Variations of effective stresses around the slip plane during edge dislocation motion. (d) Differences between the applied and effective stresses as function of the dislocation velocity. (e) Variations of steady-state velocities for 49.107° and 90° dislocations as a function of shear force at 100K and 300K.

shear stresses. We see that the applied stress σ_{app} is not coinciding with the effective stress σ_{eff} acting on the dislocation. The difference is due to the thermostat's friction force. More precisely, the dislocation motion generates heat proportionally to the dislocation velocity. Accordingly, the viscous forces sustaining the targeted temperature are proportional to that velocity. This is confirmed with Figure 6.2 (d) which shows the relationship between the magnitudes of the stress differences as function of the dislocation velocity: a linear correlation clearly applies. Finally, we can construct the relationship between dislocation velocities and the effective stresses. Figure 6.2 (e) shows this relationship for the 49.107° and 90° dislocations at 100K and 300K. The simulations reveal that:

1. The dislocation velocities first increase linearly with the load, and progressively saturate due to an increase of the effective drag force.
2. The dislocations in the hot systems (300K) glide slower than the dislocations in the cold systems (100K).
3. This temperature effect is more important in the linear regime (for small applied shear) than in the saturation regime.
4. The strength of this temperature effect depends on the character angle.

These observations are consistent with MD simulations in several publications [Martínez et al. (2008); Olmsted et al. (2005); Bhate et al. (2002)] for screw (0°) and edge (90°) dislocations, and can be rationalized by theoretical models [Nabarro (1947); Leibfried (1950); Eshelby (1956); Hikata et al. (1971); Gorman et al. (1969)]. In the following section, we will investigate the variation of the mobility law with respect to the character angle and compare it with the aforementioned models.

Eshelby-Olmsted approach

Olmsted et. al. [Olmsted et al. (2005)] recently studied dislocation mobility laws using atomistic simulations, and showed that their results were confirming previous theoretical observations [Nabarro (1947); Leibfried (1950); Eshelby (1956); Hikata et al. (1971); Gorman et al. (1969)]. More precisely, they fitted their numerical findings to the following phenomenological equation [Olmsted et al. (2005)]:

$$\sigma_{res} = \begin{cases} ATv_d & \text{if } v_d \leq v_0 \\ ATv_d + D(v_d - v_0)^{3/2} & \text{if } v_d > v_0 \end{cases} \quad \text{with} \quad \sigma_{res} = \sigma_{eff} - \sigma_p \quad (6.2)$$

Chapter 6. Mobility law of dislocations in Aluminum

with v_d the dislocation velocity, σ_{res} the resolved shear stress, σ_p the Peierls stress¹², T the temperature, and A , D two fitting constants. This equation accounts for the transition of dislocation damping mechanisms as a dependence on the dislocation velocity v_d . When the dislocation velocity v_d is smaller than the critical velocity v_0 , only the phonon viscous term ATv_d is considered. The dislocation mobility in this linear regime ($v_d \leq v_0$) can be described by the damping constant A times the corresponding temperature T . For $v_d > v_0$, an additional damping effect occurs due to supersonic wave emissions. Eshelby [Eshelby (1956)] showed that this new contribution should increase non-linearly, taking the form $(v_d - v_0)^{3/2}$, and thus leads to the asymptotic dislocation velocities that we also observed. Following his argument, the constant D should not depend strongly on the temperature T .

Figure 6.3 shows all the relations between dislocation velocity and the effective stress that we have simulated. The data computed from MD simulations are denoted by dots, while the solid curves are fits using Equation 6.2. For each character angle, a single parameter of A and v_0 is fitted, and three different constants D are used to fit the results of three temperature cases. The results show a generally good agreement with the simulated data: we have a match within a $\sim 7\%$ error for all the character angles and temperatures investigated. However, Equation 6.2 yields a strong transition between the two different velocity regimes (damping mechanisms), and does not capture well the smooth transitions as observed in the MD results.

Figure 6.4 (a) shows the fitting parameter $A|\vec{b}|$, where $|\vec{b}|$ is the magnitude of Burgers vector, as function of the character angle θ . Screw-like dislocations (0° and 60°)³ show the highest damping values $A|\vec{b}|$ implying large phonon viscous forces. According to experiments [Hikata et al. (1971); Gorman et al. (1969); Vreeland and Jassby (1971)], the range of damping constant $A|\vec{b}|$ is between 1.8 and 7.0×10^{-8} [$\text{Pa} \cdot \text{s} \cdot \text{K}^{-1}$]. Other atomistic simulations [Bhate et al. (2002); Olmsted et al. (2005)] provided damping parameters between 3.7 and 4.5×10^{-8} [$\text{Pa} \cdot \text{s} \cdot \text{K}^{-1}$], and 6.0 and 7.5×10^{-8} [$\text{Pa} \cdot \text{s} \cdot \text{K}^{-1}$] for edge and screw dislocations, respectively. This reveals that the damping parameters obtained from our atomistic simulations are within the range of reported values. Figure 6.4 (b) shows the fitting parameters $D|\vec{b}|$ and v_0 for the studied character angles θ and temperatures T . As could be granted to the Eshelby analysis, the fitted parameter D depends weakly on temperature. Concerning the critical velocity v_0 , Marian and Caro [Marian and Caro (2006)] recently argued that it can be defined from the reciprocal space structure, and more precisely from the crystalline dispersion curves. This transition is thought to be strongly correlated to the minimum phase velocity v_p^{min} in the dislocation propagation direction [Marian and Caro (2006)]. This last argument seems not general enough to explain the value of v_0 for every mixed angle, as can be observed from Figure 6.4 (c). In the following section, we discuss the link between the critical velocity v_0 and the dispersion relation.

¹The employed values can be found in Section 5.5. We consider the Peierls stresses at 0K although the mobility law describes dislocation mobilities in a finite temperature.

²Some authors [Martínez et al. (2008); Bhate et al. (2002)] prefer not to incorporate the Peierls stress definition into the resolved shear stress.

³The two dislocations are constructed based on the same family of lattice orientation associated with screw dislocations, x:{110} y:{111} and z:{112}.

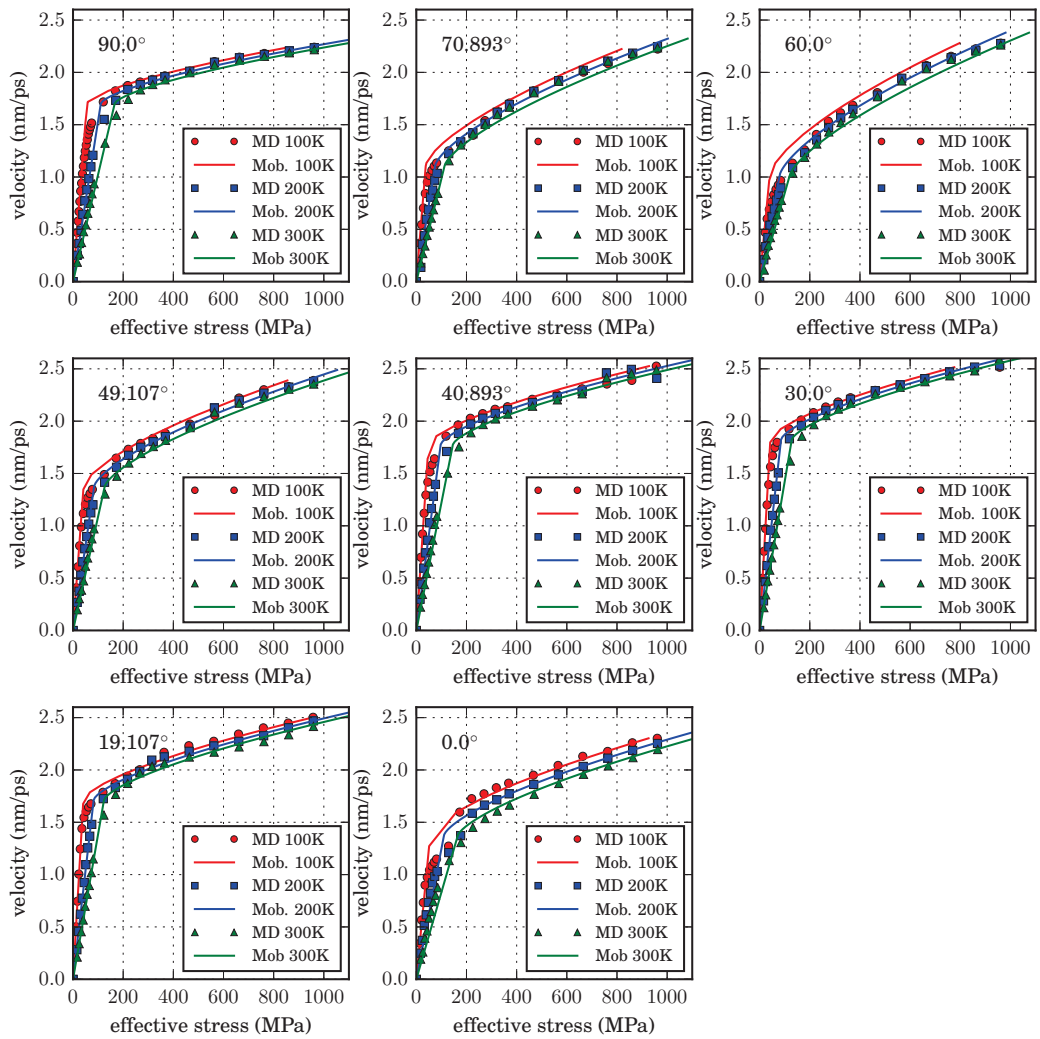


Figure 6.3 – Dislocation mobility for the various character angles and temperatures. The MD results are described by the markers and the fits using Equation 6.2 are depicted by the solid lines. For the 100K, 200K and 300K cases, the simulations and fits are denoted with the red, blue and green colors. The critical velocities v_0 are notified by the black-dashed lines.

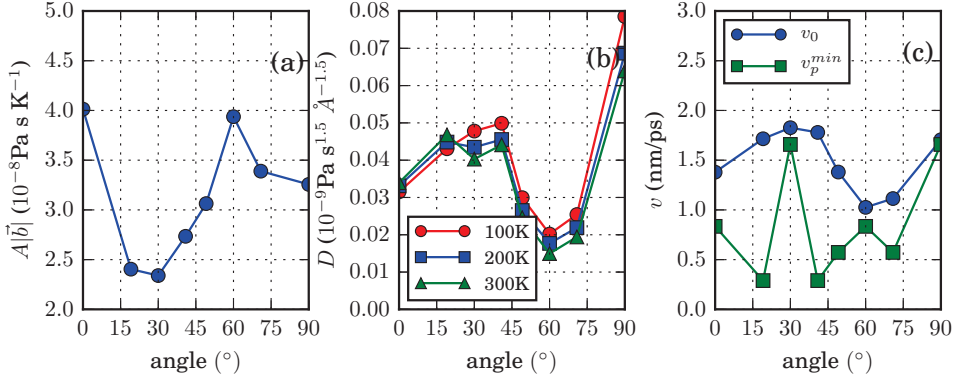


Figure 6.4 – (a) Variation of the damping parameter A multiplied by the magnitude of Burgers vector $|\vec{b}|$ for the various character angles. (b) Variations of damping constant D with respect to character angle. The constants for 100K, 200K and 300K cases are represented by red circles, blue squares and green triangles, respectively. (c) The fitted critical velocity v_0 and the minimum phase velocity v_p^{min} in the dislocation propagation direction of the various character angles.

Discussion: critical velocity

Many authors [Eshelby (1956); Bhate et al. (2002); Marian and Caro (2006); Atkinson and Cabrera (1965); Ishioka (1973)] have discussed the existence of the critical velocity v_0 . A lot of efforts aimed at understanding its origin by using lattice dynamics [Atkinson and Cabrera (1965); Ishioka (1973); Ramos de Debiaggi and Caro (1987); Flytzanis et al. (1974)] based on a Frenkel-Kontorowa model [Frenkel and Kontorowa (1938)]. All of these previous studies identified critical regions in the reciprocal lattice, which can be described by the equation:

$$\omega(k) = kv_d \quad (6.3)$$

with $\omega(k)$ the time frequency associated with the wave vector k and v_d the dislocation velocity. As Eshelby [Eshelby (1956)] noted, when $\frac{\omega(k)}{k} = v_d$ then the wave equation can flip from a rapidly decaying solution to an oscillatory one, which changes completely the damping mechanism. The simple interpretation is that when the dislocation moves faster than the phase velocity $v_p(k) = \frac{\omega(k)}{k}$, supersonic modes are created, and these waves radiate energy.

To apply Eshelby's argument on our work, we need the 3d dispersion relations $\omega(k)$ for the selected potential. These relations can be calculated by using the dynamical matrix, which is derived from the equation of motion [Kittel (1986)]. To compute this matrix [Liu et al. (2006)], a set of molecular dynamic simulations considering the fifth nearest neighbor atoms have been employed. The computed dispersion relations have been validated in specific directions by comparing to a published source [Tadmor et al. (2011)]. Figure 6.5 shows the curves $\omega(k)$ for screw 0°, mixed 40.893° and edge 90° dislocations directions. For each of these directions,

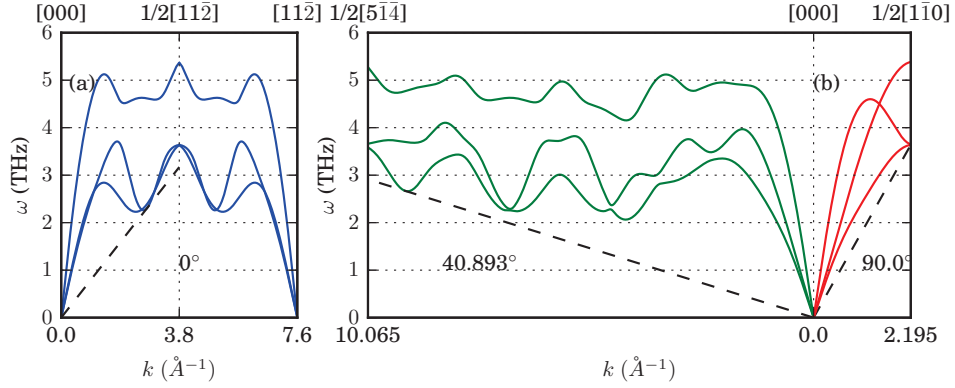


Figure 6.5 – Dispersion curves in the propagation direction of screw 0° , mixed 40.893° and edge 90° dislocations. Three phonon branches exist for each wave number k . For each angle, the minimum phase velocity v_p^{min} corresponds to the slope of the black dashed line.

the three dispersion branches are presented.

Marian and Caro [Marian and Caro (2006)] studied dislocation mobilities of edge and screw dislocations, and argued that minimum phase velocities v_p^{min} computed from these dispersion curves correspond to the critical velocities v_0 used in Equation 6.2. For example, a screw 0° dislocation propagates in the $[11\bar{2}]$ direction, and the three dispersion branches in that direction are shown in Figure 6.5 (a) by the blue curves. We see that these dispersion curves are periodic over an interval L (depending on θ), so it is natural to use $L/2$ to compute v_p^{min} which leads to the formula:

$$v_p^{min} = \min \left\{ v_p(k) = \frac{\omega(k)}{k}, \quad k \in [0, L/2] \right\} \quad (6.4)$$

The computed v_p^{min} for each angle corresponds to the slope of the black dashed line as shown in Figure 6.5. The variations of v_p^{min} with character angles are shown in Figure 6.4 (c) by the green square-dot line. When compared to v_p^{min} and v_0 , we conclude that Marian and Caro [Marian and Caro (2006)] argument works well for edge-like (30° and 90°) and for screw-like (0° and 60°) dislocations, but it fails to predict the critical velocities v_0 for the other mixed angles.

This can be rationalized by considering crystallography as discussed in Cho et. al. [Cho et al. (2015)]. The size of the minimal periodic unit cell varies with the character angle. When the axes of the FCC lattice are aligned with the x, y, z directions, the minimal lattice employed is the FCC primitive unit cell. For completely arbitrary angles, the size of the minimal lattice changes, and there are angles (irrational) for which the periodicity length is infinity. There is a similar variation of the periodicity length in the reciprocal space, which brings the following definition problematic: the pulsation $\omega(k)$ is a necessarily bounded quantity ($\omega(k) < \omega^{max}$)

such that:

$$0 \leq \frac{\omega(k)}{k} \leq \frac{\omega^{max}}{k} \quad (6.5)$$

And consequently:

$$0 \leq v_p^{min} \leq \min \left\{ \frac{\omega^{max}}{k}, \quad k \in [0, L/2] \right\} = \frac{\omega^{max}}{L/2} \quad (6.6)$$

The immediate consequence is that for a large periodicity length L of the reciprocal space, v_p^{min} becomes arbitrarily small. However, up to our knowledge, the transition velocity v_0 does not present such a behavior for any angle.

In reality, the assumption that excited phonons exist only in the dislocation propagation direction is incorrect. After all, the motion of atoms at the dislocation core is mainly along the Burgers vector \vec{b} with a complication due to the separation into Shockley partials [Hirth and Lothe (1992)] which leads to all sorts of wave propagation directions. Consequently, the assumption of unidirectionality suggested by Marian and Caro [Marian and Caro (2006)] is insufficient to predict the critical velocities for general mixed dislocations in FCC crystalline materials.

Implementation of mobility law

The obtained dislocation mobility law obtained now is implemented into a discrete dislocation dynamics (DD) simulator, which is the well-known ParaDis software package [Bulatov et al.; Arsenlis et al. (2007)]. In order to describe the effects of the mobility law on dislocation dynamics, we simulate dislocation loops with three different mobility modules. The first one is implemented in the present version of ParaDis. Currently, the mobility module of ParaDis uses two damping parameters B_{90} and B_0 ⁴ for edge 90° and screw 0° character angles, respectively, and interpolates linearly between these two constants to get damping values for mixed angles [Bulatov and Cai (2006)]. With this strategy, the nodal velocity increases linearly with shear loading, and the saturation regime is not considered. The second module consists in exploiting the obtained parameters (A_{90} , D_{90} and A_0 , D_0) of edge 90° and screw 0° dislocations. The mobility law for a mixed angle is constructed by linear interpolation between the edge and screw parameters. The last case uses the (proposed) complete mobility law, which accounts for the 8-intermediate angles considered in this work. This law allows us to refine the interpolated mobilities for the mixed angle dislocations.

Figure 6.6 shows the computational domain employed to model a single dislocation loop. This dislocation loop is inserted onto the centered slip plane. Anisotropic aluminum material

⁴According to our proposed mobility law, B_θ is corresponding to $A_\theta T$.

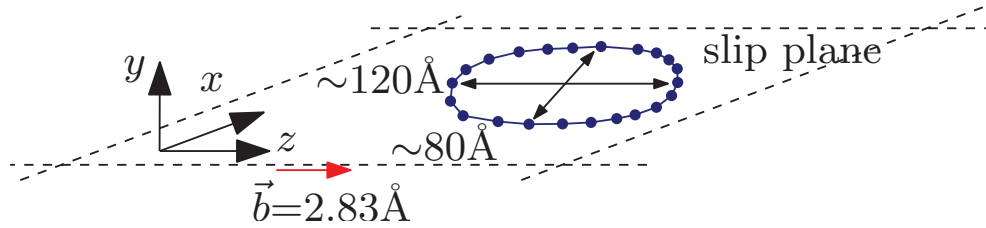


Figure 6.6 – Schematic modeling of a dislocation loop in a discrete dislocation simulation. Infinite boundary conditions are employed in all directions. A constant shear stress $\sigma_{yz} = 700\text{MPa}$ activates the dislocation loop expansion.

properties justify the initial ellipsoidal shape of the dislocation loop. The size of the ellipsoid is small when compared to dislocation loops experimentally observed in aluminum. However, the simulation setting employed here aims at highlighting the influence of the mobility law on dislocation dynamics, which we believe applies also for larger dislocation loops. In order to expand this small loop, a shear stress $\sigma_{yz} = 700\text{MPa}$ is applied, which is large enough to avoid any shrinking of the dislocation loop. The trapezoidal integration scheme is applied with a timestep of 1 femto-second (10^{-15} second).

Figure 6.7 shows top-view snapshots of the slip plane at 0ps, 2.5ps, 5ps and 10ps with the three different dislocation mobility strategies described above. Comparing the results shown in Figures 6.7 (a) and (b), we can conclude that the current DDD engine cannot correctly calculate the dislocation dynamics. As the loops expand, the effective stresses acting on DDD segments increase due to the decay of self interactions, and describing the non-linear behavior of the mobility law becomes important. This effect is comparable with the one described by Kang et al. [Kang et al. (2012)] for BCC materials.

Consequently, two different dislocation structures are finally observed at 10ps. Also, when comparing Figures 6.7 (b) and (c), it is clear that the mobility law accounting for intermediate angles produces large differences in the loops dynamics. In the latter case, the ellipsoidal loop becomes an octagon with three distinct facets in the direction of edge, screw, and mixed $60^\circ \sim 70^\circ$ dislocations. This contrasts with the rounded rectangle aligned with edge and screw dislocation directions in the former case. Arguably, the octagon shape is a more favorable dislocation loop structure since these shapes have been observed in experiments Wolfenden (1972) dealing with FCC aluminum. These three simulation results show the necessity of defining the anisotropic mobility law not only for discrete dislocation dynamics but also for the CADD3d coupling scheme in order to minimize a source of error over the global dislocation network evolution (described in Chapter 4).

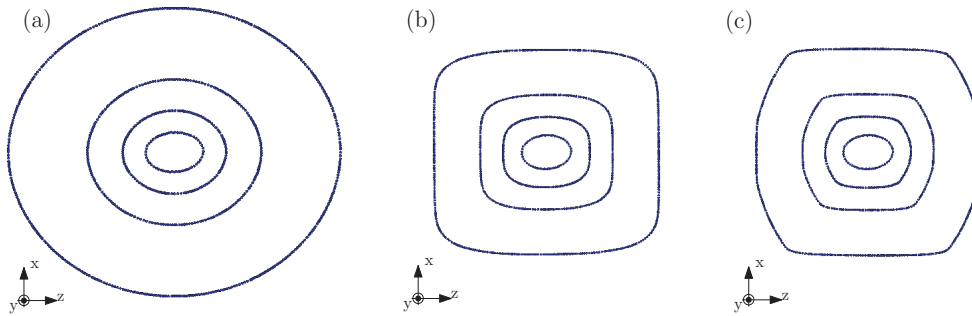


Figure 6.7 – Snapshots of dislocation loop dynamics at 0, 2.5, 5 and 10ps with three different dislocation mobility laws: (a) A linear relation (A_{90} and A_0) between dislocation velocity and shear loading is considered and interpolated linearly from edge (90°) to screw (0°) angles. (b) The linear and supersonic asymptotic regimes are considered by considering the mobility parameters A_{90} , D_{90} and A_0 , D_0 for edge (90°) and screw (0°) dislocations. Intermediate angles are interpolated linearly from edge to screw. (c) The new mobility law proposed, which accounts for the linear and supersonic regimes and a total of 8-mixed angles.

Summary

In this chapter, the mobilities of straight dislocations in FCC aluminum were studied using atomic simulations (MD) at several temperatures and for various character angles. The obtained velocity-effective_stress curves were successfully fitted to the Eshelby-Olmsted equation. We could distinguish the two velocity regimes following the damping mechanisms due to phonon viscosity and (supersonic) wave radiations. The phonon viscosity regime is characterized by the constant A that was shown to be in good agreement to other works in the literature for edge and screw dislocations. The damping constant D , relevant to the radiation regime, depends weakly on the temperature as was expected from Eshelby's theory. These two regimes are separated by the critical velocity v_0 . We could show that v_0 cannot simply be defined as the minimum phase velocity v_p^{min} in the propagation direction of the dislocation. Finally, the obtained mobility law, which is valid for several character angles, has been implemented in a discrete dislocation dynamic engine. The results show the large impact of having accurate mobilities on the dislocation dynamics.

7 Validation of CADD3d: Hybrid Dislocations

In Chapter 4, we have proposed the CADD3d method, and in Chapters 5 and 6, the necessary coupling components have been generated. Finally, in this chapter the CADD3d method is implemented and validated by studying various situations including hybrid dislocations. The first test problem, given in Chapter 7.1, considers the dynamical propagation of a hybrid straight dislocation with an arbitrary character angle. The analysis of the results allows to evaluate the sensitiveness of CADD3d with respect to the coupling components (i.e. core templates, mobility law and update step). In Section 7.2, CADD3d is tested with a hybrid dislocation loop. In that case, CADD3d needs to couple two sub-parts of an arbitrary shaped hybrid dislocation. Section 7.3 presents the coupling problem when multiple dislocations exist and interact each other. Finally, Section 7.5 summarizes the validation results of the CADD3d method.

Hybrid Straight Dislocations

In this section, the CADD3d methodology will be validated for straight dislocations. Figure 7.1 illustrates a hybrid straight dislocation with an arbitrary character angle in a perspective view (a) and from a top view (b) of the slip plane. The character angle θ can be chosen between the edge (90°) and screw (0°) dislocations. This dislocation is represented with atoms and DDD segments both being fully coupled by the reciprocal boundary conditions as discussed in Chapter 4. As shown in Figure 7.1, the pad atomic region surrounding the MD box has a thickness 7\AA .

In order to initiate the hybrid dislocation motion, a homogeneous external loading σ is initially applied on the MD and DDD domains in the direction of the Burgers vector \vec{b} . For the MD region, the atoms are displaced according to the strain $\epsilon = \sigma/\mu$ with μ the shear modulus, while for the DDD region, a homogeneous stress σ is applied [Arsenlis et al. (2007)]:

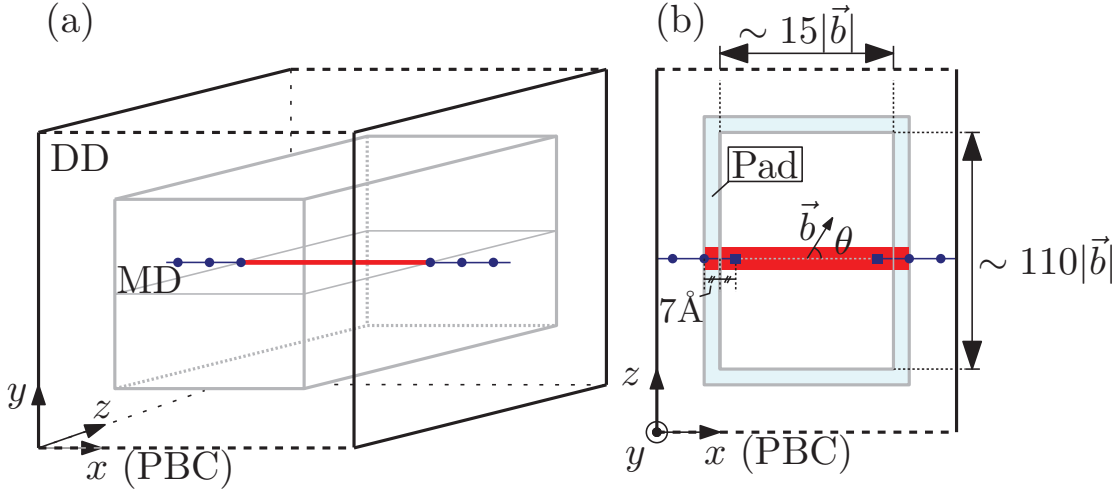


Figure 7.1 – (a) A schematic modeling of a hybrid straight dislocation. At the center of the domain, a MD system is introduced. A DDD domain is used in the remaining region. A periodic boundary condition is applied in the x direction, while infinite boundary conditions are employed in the other directions. (b) The hybrid dislocation from a top view of the slip plane. The two dislocation subparts are coupled by imposing the reciprocal boundary conditions with the pad atoms and the two constrained DDD nodes.

$$\left. \begin{aligned} \sigma_{xy} &= \sigma \cos \theta \\ \sigma_{yz} &= \sigma \sin \theta \end{aligned} \right\} : \text{DDD nodes}$$

$$\left. \begin{aligned} u_x &= \epsilon_{xy} y = \frac{\sigma \cos \theta}{\mu} y \\ u_z &= \epsilon_{yz} y = \frac{\sigma \sin \theta}{\mu} y \end{aligned} \right\} : \text{MD atoms}$$
(7.1)

with θ the character angle considered.

During the simulation, those boundary conditions are constantly applied on the pad atoms and DDD nodes to keep the constant external loading σ . Especially, for the pad atoms, the displacements of the dislocation networks (including the core correction if necessary) should be superimposed on the homogeneous strain field as discussed in Chapter 4. A detailed description of the applied displacement field is provided in the next sub-Section.

The time integration is performed explicitly with the Verlet and trapezoidal schemes for the MD and DDD methods respectively. While the two subparts of the hybrid dislocation move they are synchronized at the frequency $f_{update} = 1/t_{update}$. In this problem the duration (the so-called update step) $t_{update} = 50\Delta t$ has been chosen with Δt the time step (1fs).

The synchronization procedure can be divided into two steps as proposed in Chapter 4.

First, the discrete dislocation boundary nodes are constrained with the center of the detected MD dislocation. Second, the pad atoms are displaced according to the current discrete dislocation positions.

Displacements of Pad Atoms

As shortly described in Section 5.1, for the pad atoms far away from any dislocation core, the imposed displacement can be computed by a superposition of the linear elasticity solution with the displacement due to the imposed external shear loading (Equation 7.1). For pad atoms close to a dislocation core, the sum of the linear-elastic and external strain displacements has to be corrected to account for non-linear effects by applying the core templates. For example, the displacement of the pad atom located at \vec{x}_0 can be written as follows:

$$\vec{u}(\vec{x}_0) = \begin{cases} \sum_{i=1}^{\#nodes} [\vec{u}_{e,i}(\vec{x}_0) + \Delta\vec{u}_c(\vec{x}_0, \theta_i)] + \vec{e} \cdot \vec{x}_0 & \text{if } D(\vec{x}_0) \leq r_c \\ \sum_{i=1}^{\#nodes} \vec{u}_{e,i}(\vec{x}_0) + \vec{e} \cdot \vec{x}_0 & \text{otherwise} \end{cases} \quad (7.2)$$

with $\#nodes$ the number of the DDD nodes, $\vec{u}_{e,i}(\vec{x}_0)$ the linear elasticity displacement solution [Barnett (1985); Barnett and Balluffi (2007); Fivel and Depres (2014)] of a segment connecting i th and $i + 1$ th nodes, $\Delta\vec{u}_c(\vec{x}_0, \theta_i)$ the correction field of the core template of a mixed angle θ_i , θ_i a local character angle of the i th segment, $D(\vec{x}_0)$ the distance to the i th segment, and $\vec{e} \cdot \vec{x}_0$ the external homogeneous strain field given in Equation 7.1. As demonstrated in Section 5.6, the core template corrections are restricted to the pad atoms within ten times magnitude of the Burgers vector ($r_c = 10|\vec{b}|$) from the core $D(\vec{x}_0) \leq r_c$.

Let us discuss the linear elasticity solution \vec{u}_e . We employ Barnett's approach [Barnett (1985); Barnett and Balluffi (2007); Fivel and Depres (2014)] to obtain the analytic expression of the displacement field \vec{u}_e . One of the requirements of Barnett's method is to consider only closed dislocation loops. In other words, the sum of the Burgers vectors of all the DDD segments has to be zero such that the dislocation networks are closed. Therefore, in order to evaluate Barnett's expression for the present problem, the straight DDD dislocation network should be closed implicitly.

We actually close the DDD network in two steps. First, we have to close the external boundary of the DDD segments. The straight dislocation can be considered as a part of the rectangular dislocation loop as shown with a dotted line in Figure 7.2. This rectangular loop considers two additional fictitious points (cross markers) far away from the MD box in the gliding direction (z). These points are connected to the two outward boundary nodes. Second, we have to connect the internal boundary region which should overlap the MD domain. The two slaved nodes can be simply connected with a straight line which is comparable to the MD

part of the hybrid dislocation as shown in Figure 7.2 (a). Another possibility is to introduce segments on the dislocation line detected from the atomic arrangement as shown in Figure 7.2 (b). For the present problem, the first strategy (Figure 7.2 (a)) is employed to close the internal

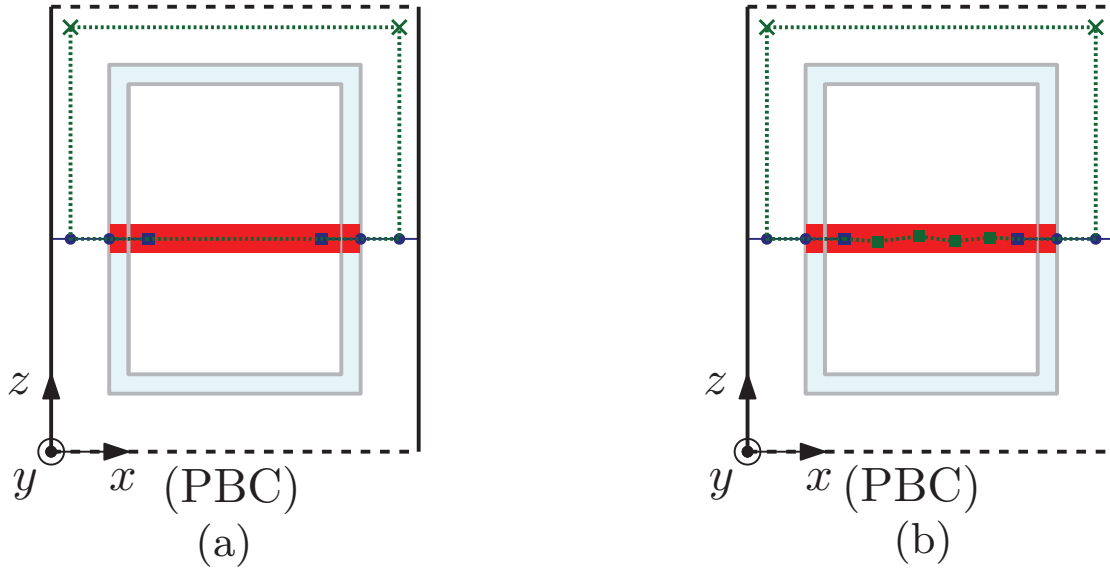


Figure 7.2 – The external boundary of the DDD nodes are closed by the two fictitious nodes shown with the cross markers. The internal boundary regions of the two hybrid straight dislocations are connected by (a) a straight line between the two slaved DDD nodes and (b) the result of the MD dislocation detection.

part of the DDD network. The detection approach (Figure 7.2 (b)) will be used for the curved hybrid dislocation in Section 7.2.

Results

The evolution of the hybrid dislocation positions (the MD and the DDD subparts) along the gliding direction (z axis) are measured during the simulations, and the results are shown in Figure 7.3 (a). For simplification purposes, only the results of two shear loading cases (100MPa and 500MPa) are depicted. The dislocation velocity is evaluated by finite difference and are shown in Figure 7.3 (b). The MD and DDD results are denoted by the markers and the dashed lines respectively.

At the beginning of each simulation, the dislocation first accelerates. After some time (~ 4 ps), the dislocation glides at a globally constant velocity. We note that effective masses m have been pre-computed from independent atomistic simulations [Cho et al. (2016)] and included in the mobility law of the DDD engine to account for the initial dislocation acceleration. Although m is angle dependent, we employ an averaged value of $100\text{MPa} \frac{f s^2}{\text{\AA}}$ in all the simulations that will be conducted. The equation of motion employed in the DDD engine can be written as follows:

7.1. Hybrid Straight Dislocations

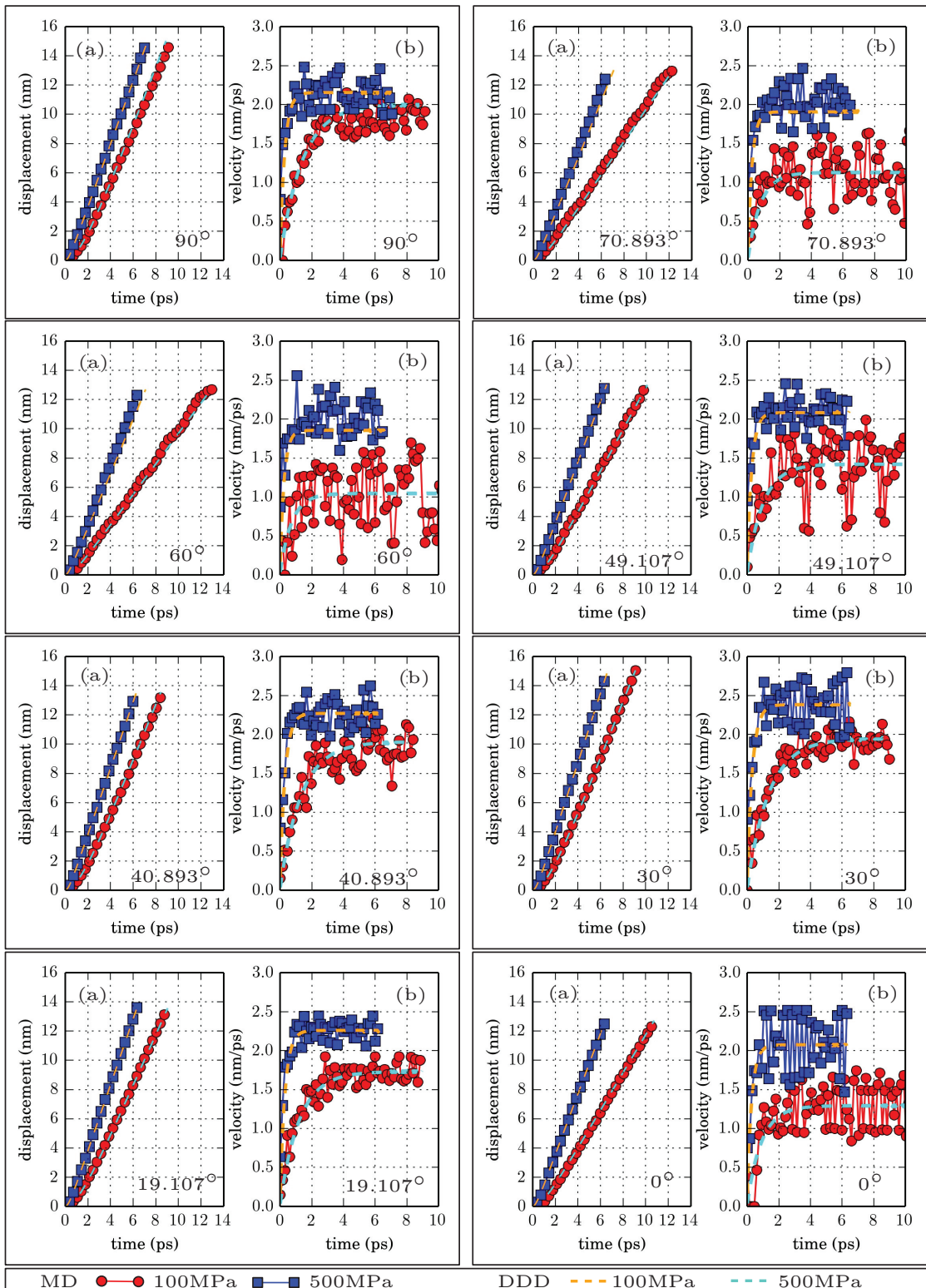


Figure 7.3 – Evolutions of (a) the displacement and (b) the velocity of the hybrid dislocations with the selected eight character angles and the two shear stresses (100MPa and 500MPa). The results of the MD sub-part of the hybrid dislocations are represented by the (red and blue) circle-lines, and the (orange and cyan) dashed lines represent the results of the DDD sub-part of the hybrid dislocations.

$$\sigma_{\text{res}} = B_{\theta} v + m \dot{v} \quad (7.3)$$

with σ_{res} the resolved shear stress defined in Equation 6.2, B_{θ} ¹, the damping parameter for a given character angle θ (See Section 6.4), v the current dislocation velocity, and \dot{v} the acceleration computed with a finite difference approach: $\dot{v} = (v^{n+1} - v^n)/\Delta t$. We note that if the resolved shear stress is smaller than zero, the mobilities of DDD nodes are set to be zero.

By comparing the results of the atomistic and discrete dislocations, we can conclude that the CADD3d methodology works well with a single hybrid straight dislocation. More precisely, the coupling procedure does not yield to significant artificial forces at the coupling interfaces between the two domains, and maintains the two sub-parts of the hybrid dislocation as one single coherent entity. We want to emphasize that correct coupling results can only be obtained when the core templates [Cho et al. (2015)], the mobility law [Cho et al. (2016)] and the update step (t_{update}) are correctly set. In the following subsection, we will demonstrate this claim by varying purposely these crucial parameters.

Sensitiveness of the Coupling Parameters

In order to identify the influence of the parameters onto the hybrid dislocation behavior, we will vary them independently in distinct simulations. We first employ the core templates with a smaller cut-off radius $r_c = |\vec{b}|$ (Case1) than the previous one $r_c = 10|\vec{b}|$. Second, the mobility parameter will be changed to $B_{\theta} = 2B_{\theta}$ (Case2) and $B_{\theta} = \frac{1}{2}B_{\theta}$ (Case3) with B_{θ} the damping constant. Case4 will set the effective mass to zero $m = 0$ which will remove any inertial effects. Lastly, a lower update frequency will be used ($t_{\text{update}} = 200\Delta t$) in Case5 instead of $t_{\text{update}} = 50\Delta t$ previously employed.

The snapshots of the hybrid dislocation dynamics at 0ps and 5.5ps for the two cases (Case1 and Case2) with the reference simulation (the mixed 30° dislocation under 100MPa) are shown in Figure 7.4. When compared to the reference simulation result ((a) and (b)), the simulations with the coupling parameters incorrectly set show the hybrid dislocation motions, where the mismatched structures are observed. More precisely, for the Case1, the compact dislocation cores are observed at the coupling interface due to the insufficient correction of the displacement field. Second, the different dislocation mobility leads to an artificial bending of the line.

The evolution of the hybrid dislocations with the five cases is shown in Figure 7.5. Let us focus on Case1 (d). The comparison indicates that a too small core template slows down the hybrid dislocation motion. This occurs due to ghost forces created from the mismatched dislocation core structure as shown in Figure 7.4 (d). Second, the comparison of Case2 (Case3)

¹ B_{θ} is the damping constant evaluated from Eshelby-Olmsted mobility law as follows: $\sigma = B_{\theta} v = ATv + (v-v_0)^{3/2}$. A more detailed description can be found in Chapter 6.

7.1. Hybrid Straight Dislocations

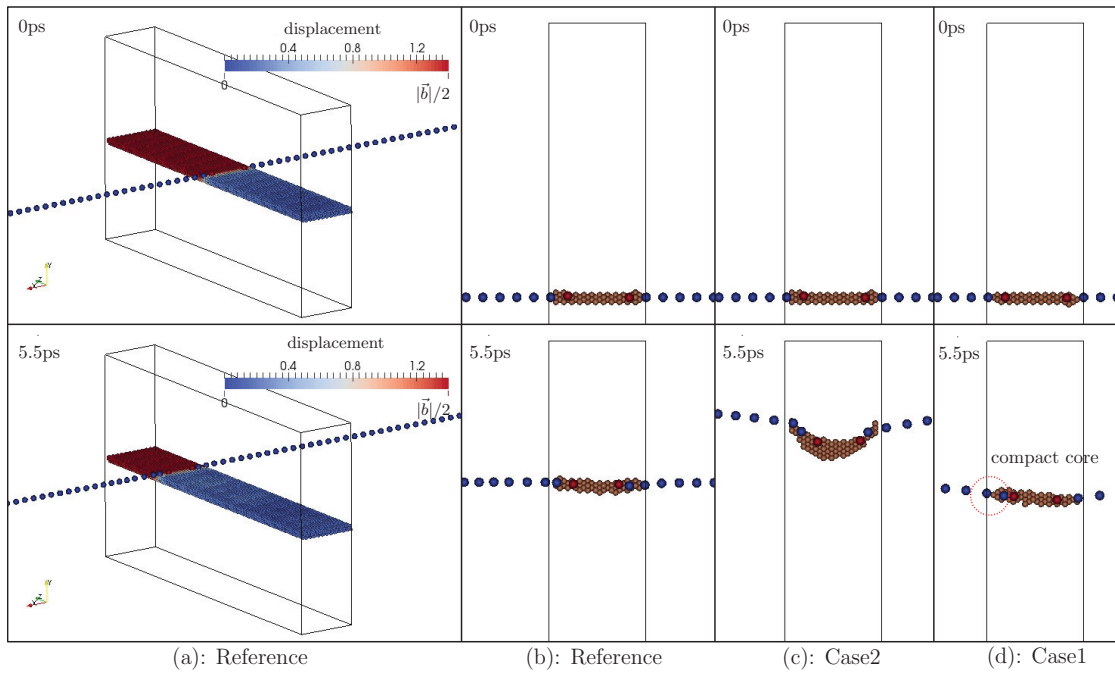


Figure 7.4 – (a) Snapshots of the dynamics of a mixed 30° hybrid dislocation with 100MPa in a perspective view (reference case). Only the atoms around the bottom slip plane are shown, and are colored by the magnitude of the displacement. The DDD nodal points are shown as big spheres. (b) Top view of the slip plane shown in (a) where the DDD nodes and the atoms violating centro-symmetry are plotted. (c) Simulation result obtained with $B_\theta = \frac{1}{2}B_\theta$. (d) Simulation result obtained with a small cut-off radius $r_c = |\vec{b}|$ for the core correction. This leads to smaller stacking fault widths as can be observed near the coupling interface.

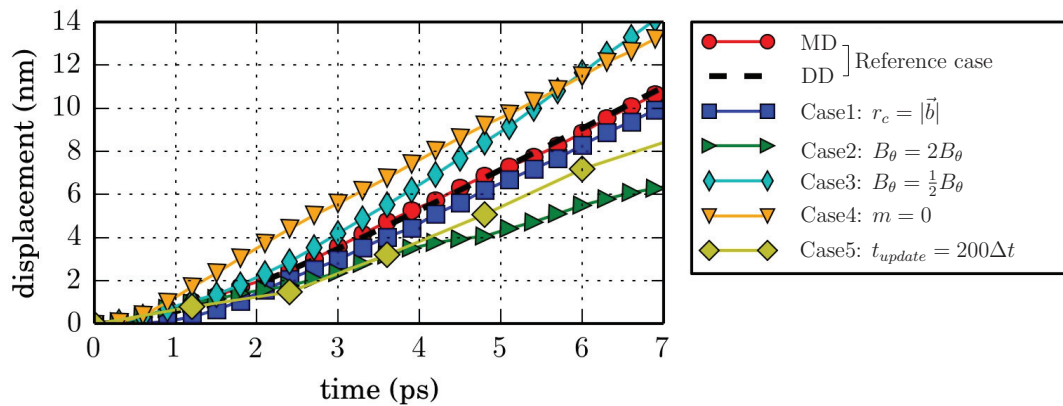


Figure 7.5 – Sensitiveness studies of the coupling scheme with the five different simulation settings (change of core template cut-off radius r_c , of the damping parameter B_θ , of the effective mass m and of the update step t_{update}). The dislocation displacements are shown as functions of time. These results can be compared to the reference results denoted by the red circle-line and the black dashed line.

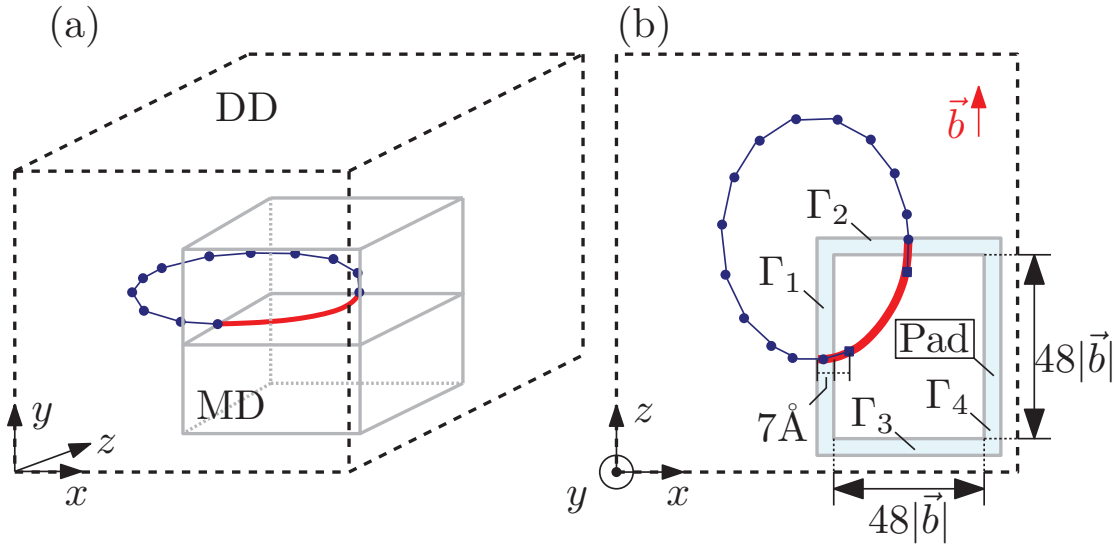


Figure 7.6 – (a) A schematic modeling of a hybrid dislocation loop in a perspective view. Infinite boundary conditions are applied in all directions. (b) The hybrid dislocation is shown from a top view of the slip plane.

with the reference, is consistent with an artificial deceleration (acceleration) of the dislocation imposed by the modified mobility parameter B_θ . Indeed, modifying the DDD mobility law leads to mismatched MD-DDD velocities and a modification of the effective velocity of the hybrid dislocation. These two last cases can be compared with Case4 to check influences of the effective mass on the coupling simulation: after 2ps the MD and DDD dislocation subparts travel at the same speed, and the influence of the effective mass disappears. Lastly, we achieve wrong simulation results when a large update step ($t_{update} = 200\Delta t$) is employed. Such an impact was expected since delaying the synchronization creates misfit configurations at the coupling interface. With this sensitiveness study we can demonstrate that the aforementioned CADD3d components need crucially to be correctly adjusted.

Hybrid Dislocation Loops

In this section, we validate the CADD3d coupling scheme with a curved dislocation shape. Figure 7.6 shows a schematic modeling of a hybrid dislocation loop. A quarter of the domain consists of atoms while the remaining region is modeled with DDD. The hybrid dislocation loop is shown with a red solid line and blue circle-line for atomistic and discrete dislocation models, respectively. The procedure employed to create this hybrid dislocation loop is the following:

1. Impose the elasto-static displacement field of the complete dislocation loop on a MD box.
2. Relax the MD box while a finite strain is imposed on the boundaries to avoid any

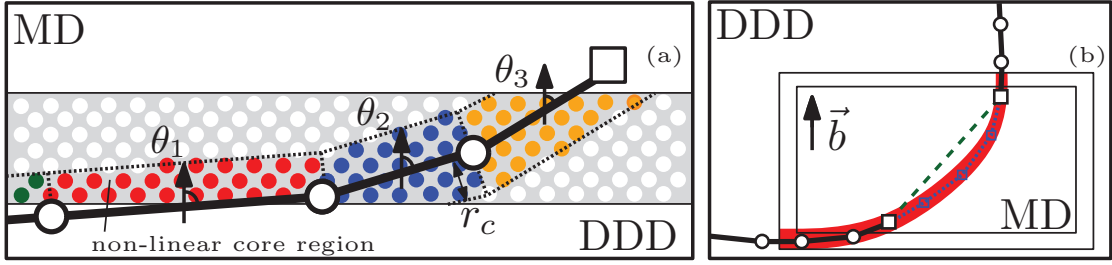


Figure 7.7 – (a) Application of multiple core templates within the pad zone. The pad region is decomposed to match each DDD segment. Based on this decomposition, the core templates with three different angles (θ_1 , θ_2 and θ_3) are applied on the red, blue and orange colored atoms, respectively. (b) Two strategies to close the loop between the two constrained DDD end nodes of the hybrid dislocation loop. The first strategy is to connect the two nodes by using a straight line as shown by the blue dashed line. The second strategy is to connect them by employing a discrete line consisting of the MD dislocation cores.

shrinking of the dislocation loop.

3. Extract the atoms from a quarter of the MD box, and replace the remaining MD dislocation with matching DDD nodes.

After the creation of the coupled model, a shear loading of 400MPa (strain for MD and stress for DDD) is applied by following Equation 7.1. The MD and DDD boundary conditions are synchronized every 50 steps ($t_{update} = 50\Delta t$), and the core templates with a radius $r_c = 10|\vec{b}|$ are employed. The geometrical evolution of this hybrid loop will be monitored and discussed in section 7.2.2. Before doing so, we wish to highlight in the following section the newly needed features to solve this coupling problem.

Additional Features of CADD3d for Curved Dislocations

If we compare to the case with the straight hybrid dislocation, there are additional difficulties due to the curved dislocation structure. First of all, the application of the core template needs to be done for many different character angles. As depicted on Figure 7.6 (b) there are now four boundary surfaces for the MD region: Γ_1 , Γ_2 , Γ_3 and Γ_4 . Since the Burgers vector \vec{b} is aligned with the z axis, the edge and screw core corrections will be applied to the regions Γ_1 and Γ_2 , respectively. When the loop will be large enough, it will necessarily cross Γ_3 and Γ_4 borders and then the angle will vary continuously. However, only a discrete set of angles have been considered in the offline MD calculation of the core template (Chapter 5). In practice, we will evaluate the correction field for a given angle by using the linear interpolation between the discrete set of pre-computed core templates as discussed in Section 5.6.

Second, the angle can be so oblique that more than a single DDD segment may intersect the pad region. Figure 7.7 (a) shows a snapshot of the simulation when multiple DDD nodes are inside the pad region. In this situation several core templates have to be applied with

different angles. The pad atoms are then subdivided into regions each associated with a constant angle. Figure 7.7 (a) shows a typical decomposition with dashed lines. On this example, the correction fields from core templates for θ_1 , θ_2 and θ_3 angles are applied on the red, blue and orange atoms, respectively.

Third, as we did for the straight hybrid dislocation in Section 7.1.1, we have to implicitly close the loop in order to compute the linear elastic displacements. As shown in Figure 7.6 (b), the DDD part of the hybrid dislocation is not closed between the two constrained nodes (square markers). This part can be closed by employing either a straight line or a discrete set of lines which follows the MD dislocation as shown in Figure 7.7 (b). For this problem, both methods will be tried, and their influence on the coupling simulation will be analyzed.

Lastly, contrary to straight dislocations, curved dislocations generate self interactions influencing the resolved shear stress calculations. As briefly mentioned in sub-Section 4.2.1, to compute the nodal forces when some parts of the dislocation network is modeled by molecular dynamics, a coupling scheme between DDD and FEM domains is needed. In the scope of this thesis we have made the following simplification: we connected the two slaved DDD end nodes by a set of constrained DDD nodes and segments. The positions of these new constrained DDD nodes are re-assigned every update step by detection from the MD representation. This strategy will provide a correct self interaction for the DDD sub-part of the hybrid dislocation loop. However, this limits to simple situations where the dislocation network can be identified without ambiguity (excluding nano-indentation for instance). In the following sub-Section, we study this test problem with two different DDD dislocation networks, and two different strategies to connect/detect the missing part of the studied dislocation loop.

Results

The snapshots of the simulation at 0ps, 1ps, 4.5ps and 5.5 ps in a perspective view are shown on Figure 7.8 (a), and from a top view of the slip plane in Figure 7.8 (b) and (c). The hybrid dislocation is shown by plotting the DDD nodes and by drawing only the atoms violating centro-symmetry for the atomic part. If we compare the obtained loop shapes obtained with the two possible ways to close the DDD loop in the MD region (Figures 7.8 (b) and 7.8 (c)), we find that the influence of the connecting strategy on the MD sub-part dislocation is negligible as demonstrated as follows.

In Figure 7.10 (a), the position of the hybrid dislocation with respect to time (along the axis $x = -z$) is presented. Velocities are evaluated by finite difference of the displacement and are shown in Figure 7.10 (b). We observe that the effect of the connectivity on the MD sub-parts dislocation is small when the MD core (along the axis $x = -z$) exists far away from the pad region. As the loop expands and the MD sub-part approaches the pad region, the influence of the connectivity strategy increases. The influence on the hybrid dislocation motion is smaller than 0.5% at maximum.

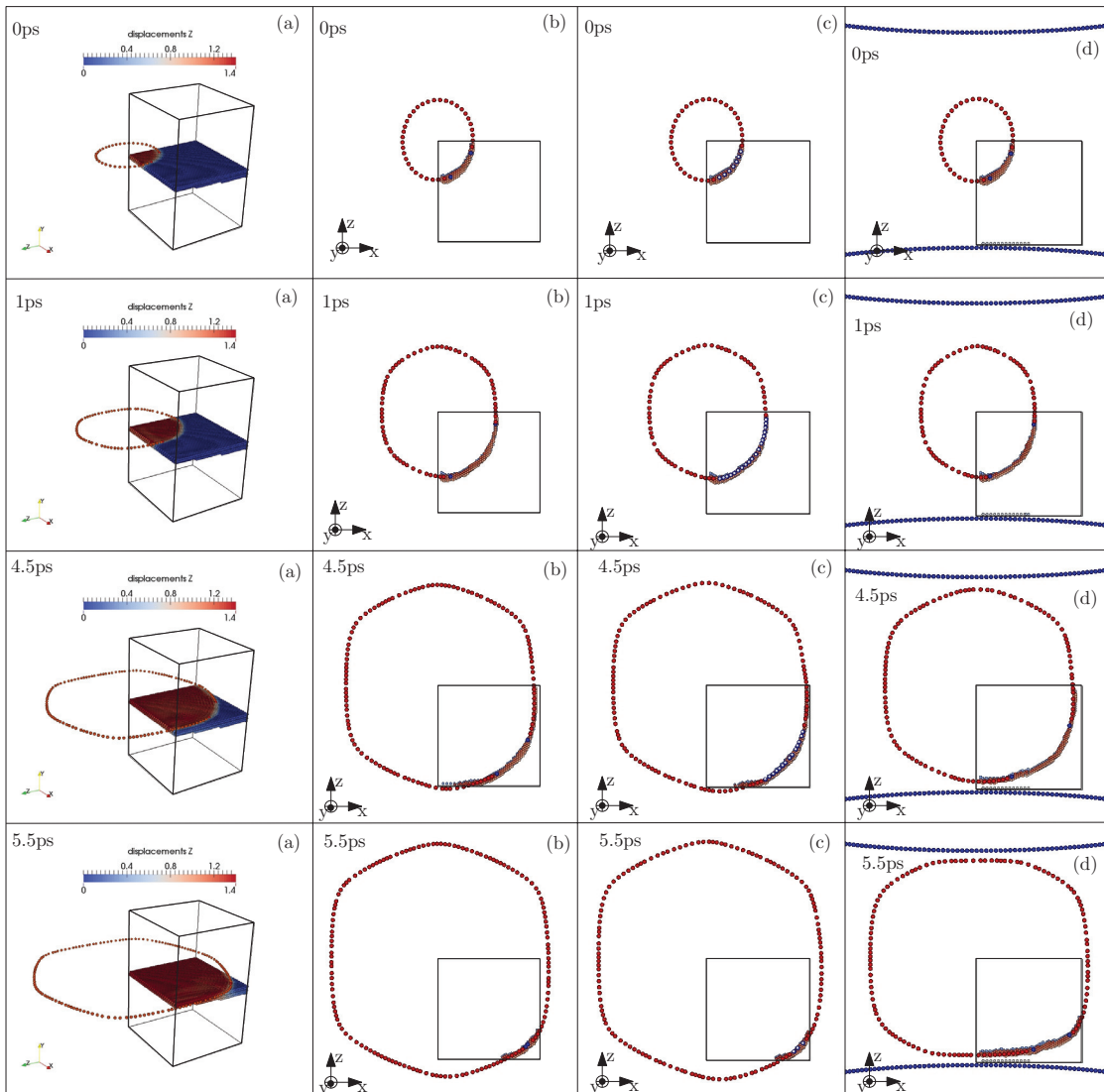


Figure 7.8 – Comparison of the hybrid dislocation loop motions at 0ps, 1ps, 4.5ps and 5.5ps. The DDD nodes are represented by the red circle markers, and the atomistic dislocations are described by the small circles. (a) Snapshots of the simulation with a straight line-connection strategy are shown in a perspective view. Only the atoms around the slip plane and the DDD nodes are shown. The colors applied on the atoms represent the displacement magnitude in the Burgers vector direction (z). (b) The same simulation (a) from a top view of the slip plane. Only the atoms violating centro-symmetry and the DDD nodes are shown. (b) Simulation with the discrete line consisting of the MD dislocation detection solution between the two constrained node. (c) Simulation with the hybrid dislocation loop and the two fixed DDD networks.

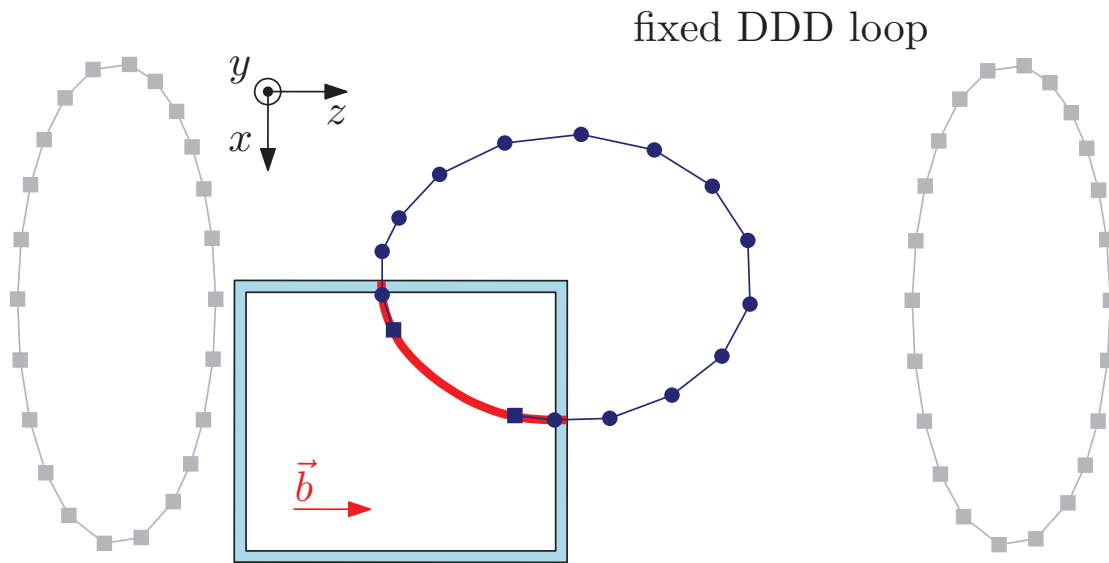


Figure 7.9 – A schematic modeling of a hybrid dislocation loop and two fixed dislocation loops. The Burgers vectors of these loops are same.

Interactions between Multiple Dislocations

In the previous sections, we studied the CADD3d method with a single dislocation, and validated it with two different, yet simple, dislocation shapes, the straight line and the loop. In this section, we will introduce more dislocations, in order to stress the coupling with regard to dislocations interaction. Consequently, a hybrid dislocation loop is first inserted at the center of the domain as shown in Figure 7.9. Then two fixed ellipsoidal discrete dislocation loops are set to surround the hybrid dislocation. Because the Burgers vectors of the fixed loops are identical to the one of the hybrid dislocation loop, all the loops repel each other. The interaction force between the DDD nodes is computed by DDD engine while the interaction between atoms and the fixed loops are enforced thanks to CADD3d. More precisely, when the displacement field of the pad atoms is evaluated, the contribution of the fixed DDD loops will be considered through the linear elasticity displacement field. Such a pad configuration will generate repelling forces acting on the MD part of the hybrid dislocation loop.

A shear loading of 400MPa is applied to drive the hybrid dislocation motion. The two DDD end nodes are connected by using a straight line since this simpler strategy was shown to be accurate enough in sub-Section 7.2.2. We synchronize the coupling boundary conditions every 50 steps ($t_{update} = 50\Delta t$) with the the core templates (cut-off radius $r_c = 10|\vec{b}|$).

Figure 7.8 (d) shows simulation snapshots at 0ps, 1ps, 4.5ps and 5.5ps from a top view of the slip plane. As the hybrid dislocation expands and approaches the fixed DDD loops, the repelling forces increase and the hybrid dislocation completely stops in front of the fixed loops. The displacements and velocities as a function of time are shown in Figure 7.10. We find that the two sub-parts of the hybrid dislocation travel as one single dislocation. Even the velocity

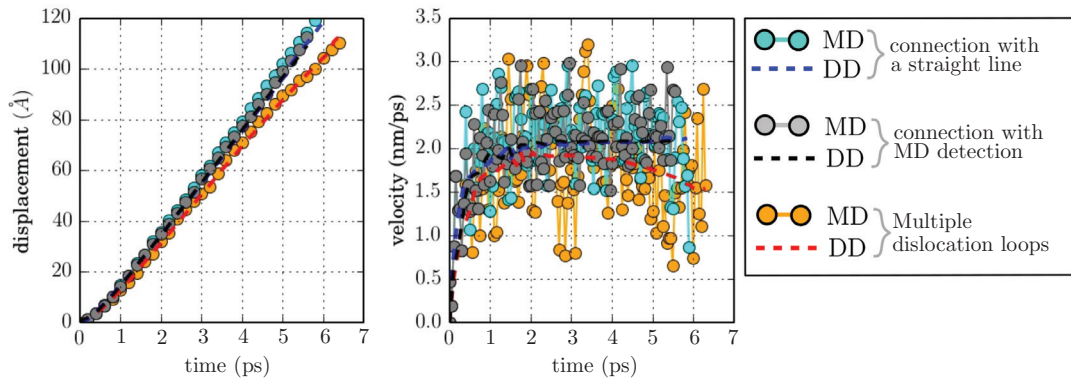


Figure 7.10 – Displacement and velocity evolutions of the dislocation loops with the three different simulation setting. The first two problems are the hybrid dislocation loops with the two different connection strategies. The third problem is the hybrid dislocation loop with the two fixed DDD networks.

profiles are similar which proves the quality of the CADD3d approach. The CADD3d method was shown to be valid also in the case where multiple dislocation interactions are considered.

Contraction of hybrid dislocation loop

The last test problem considers a hybrid dislocation loop under the shear loading 70MPa, which is smaller than the stress value maintaining static dislocation loop (370MPa). Such shear loading lets the hybrid dislocation loop contract under the action of self stresses. Figure 7.11 shows a schematic view of the expected hybrid dislocation loop dynamics. As the loop contracts, we observe that the curvature increases and the distance between the two core templates (shown with the red hatching) decreases. As discussed in Section 5.6, this situation does not fulfill the condition in which the core template approximation is applicable.

Figure 7.12 shows the displacement evolution of MD and DDD parts of the hybrid dislocation loop along the $x = -z$ axis. At the beginning of the simulation, the two sub-parts contract with the same speed, but they behave differently when the loop curvature increases. This test-problem result shows that, to provide a correct CADD3d-coupling prediction the assumption of low curvature must be satisfied.

Summary

In this chapter, we presented various 3d dislocation dynamic simulations using the proposed CADD3d method. The first considered problem introduced a hybrid straight dislocation, made partly with atoms and partly with discrete dislocation dynamics segments. The simulation was demonstrated to accurately model the dynamical evolution of a single

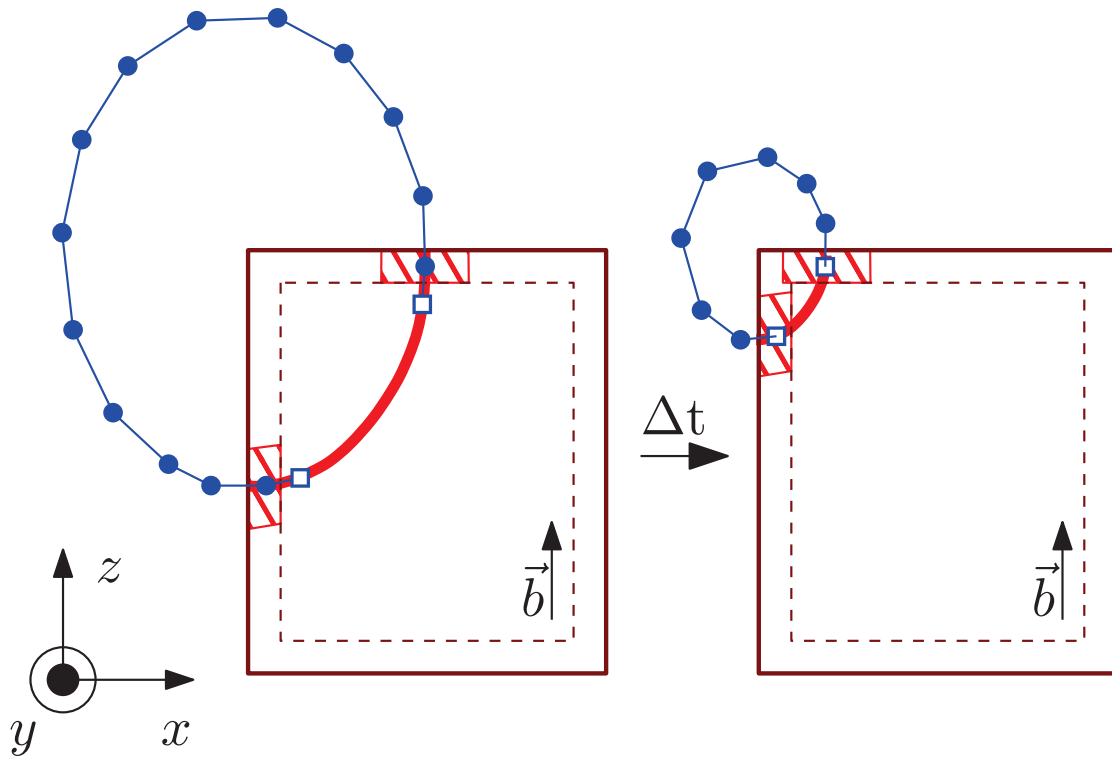


Figure 7.11 – Contraction of the hybrid dislocation loop. As the loop contracts, the curvature increases, and the spacing between the two core templates reduces.

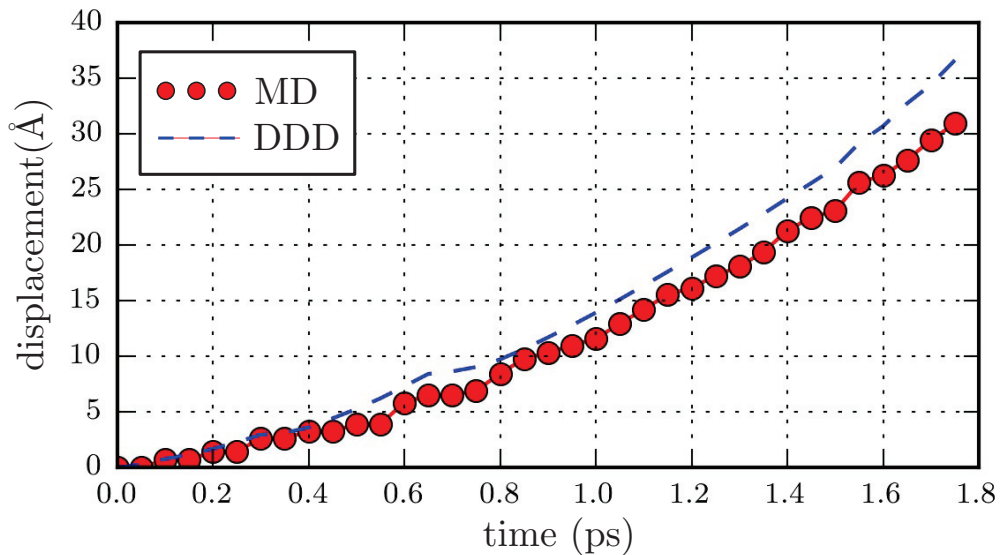


Figure 7.12 – Displacement evolution of the MD and DDD parts of the dislocation loop. As the loop contracts, the difference in behavior between the two sub-parts of the loop increases with time.

hybrid straight dislocation such that it behaves as one single dislocation. The sensitiveness of the coupling scheme has been analyzed with respect to three of the coupling parameters (core templates, mobility law and update step), and we showed that they have to be adjusted correctly in order to achieve accuracy. The second elected problem involved a hybrid dislocation loop. If compared to the first problem, a major difficulty arose from the geometry of the domain: the core structure needed at the coupling interface can be of multiple arbitrary character angles. Nevertheless CADD3d successfully preserved the curved dislocation loop. Furthermore, one have shown that the coupling also works as expected in the case where different dislocation loops interact through the coupling. Lastly, we have analyzed the limitation of the core template application by studying the contraction of the hybrid dislocation loop with a small shear loading. In consequence, we can conclude that the proposed CADD3d method is a valid approach for coupling MD with DDD domains, which contain dislocations with curved shapes and low curvatures in FCC aluminum.

8 Frank-Read Source Dynamics in Al and Al-5%Mg

After the successful validation of CADD3d shown in the previous chapter, we now apply our method on a material plasticity problem, where hardening effects are influenced by the intrinsic material structures at multi-scales. Let us quickly recall the original motivation of this thesis: for small specimens a size dependent strength is observed because plastic deformations are strongly governed by dislocation movements. To describe this effect, there are two important mechanisms: the interaction with dislocation/obstacle and the dislocation nucleation. These occur concurrently at the nano- and micro-scales. Thus to tackle such problems a CADD3d-like (multiscale) method is necessary. In this chapter, a problem dealing with these two dislocation processes will be studied thanks to CADD3d.

Frank-Read source in crystalline materials

A Frank-Read (FR) source is a defect that can emit multiple dislocations [Hirth and Lothe (1992); Banabic (2000)]. Such sources can explain how a constant plastic flow can be achieved. A FR source is a planar dislocation pinned between two points. The pinning constraint can be caused by interaction with particular crystal defects, such as impurities, precipitates or sessile dislocations [Hirth and Lothe (1992)]. Figure 8.1 (a) shows a FR source composed of two sessile dislocations (A and B). A top view is depicted in Figure 8.1 (b) (instant 1).

The evolution of such a FR source can be summarized as follows: under a shear load, the planar dislocation glides and bends (instant 2). As the bowing-out proceeds, two screw oriented parts (pointed as C1 and C2) with opposite signs appear behind and around the pinning points (instant 3). These screw parts of opposite signs contact and annihilate one another (instant 4). Finally, a closed dislocation loop and a new dislocation segment (A and B) emerge. The created dislocation loop can travel (instant 5) in the crystal, while the remaining dislocation between A and B may form another dislocation loop with the same process we have described.

In general, a FR source interacts with any other defects. Figure 8.2 shows an experimental

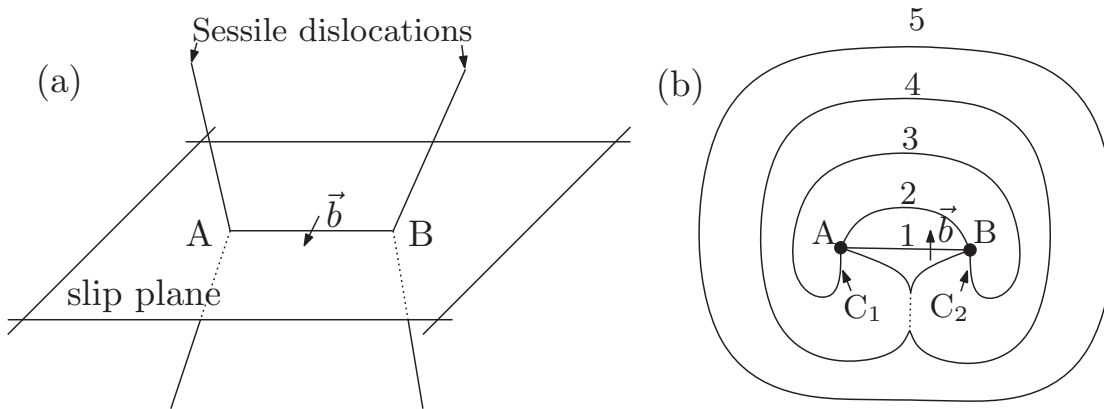


Figure 8.1 – (a) Configuration of a Frank-Read source composing to two sessile dislocations A and B. The segment between A and B is a dislocation on the glide plane. (b) A nucleation process of a dislocation loop from the Frank-Read source.

observation of a FR source in an Al-Mg alloy [Amelinckx (1964)] within a grain of characteristic size $\sim 5\mu m$. As can be seen on the figure, other defects may exist around the FR source (substitutions, interstitial, voids and dislocations). As said in Chapter 2, such defects may yield short or long-range stress fields and can consequently influence the FR source evolution. For example, dislocations can be stopped by obstacles as discussed in sub-Section 2.2.3. Such impeded dislocations will induce a backstress which reduces the resolved stress acting on the FR source. Finally, the FR source may cease to nucleate dislocations if the resolved shear stress is completely compensated by the backstress. To maintain a constant plastic flow, dislocations have to be nucleated with a higher shear load. Macroscopically, such mechanism are perceived as strain hardening (also called work-hardening) effect.

Figure 8.2 reveals that we need to consider defects in numerical studies addressing plasticity. However, in all previous numerical studies of FR sources [Maurice et al. (2003); Shimokawa and Kitada (2014); Bulatov and Cai (2006); Verdier et al. (1998)], it was not possible to evaluate quantitatively the strain hardening effect, even though they were considering the simpler defect free case. Indeed, the grain sizes can vary from 10nm (small grains) to $10\mu m$ (large grains) [Geipel and Banhart (1996); Amelinckx (1964)] while the nucleation process remains local. Again, this requires a multiscale treatment. With the CADD3d method, we can handle both nucleation and long range interaction, also when zero-dimensional defects are included. In the following section, we detail a simulation setup to address FR sources in aluminum (Al) and aluminum-5%magnesium (Al-5%Mg).

A Double Frank-Read Source in CADD3d

To analyze the hardening effect due to substitutions, we wish to compare a pure aluminum and an aluminum-5%magnesium materials. The considered domain is shown in Figure 8.3. We insert a pair of FR sources with the following procedure: first, one atomistic

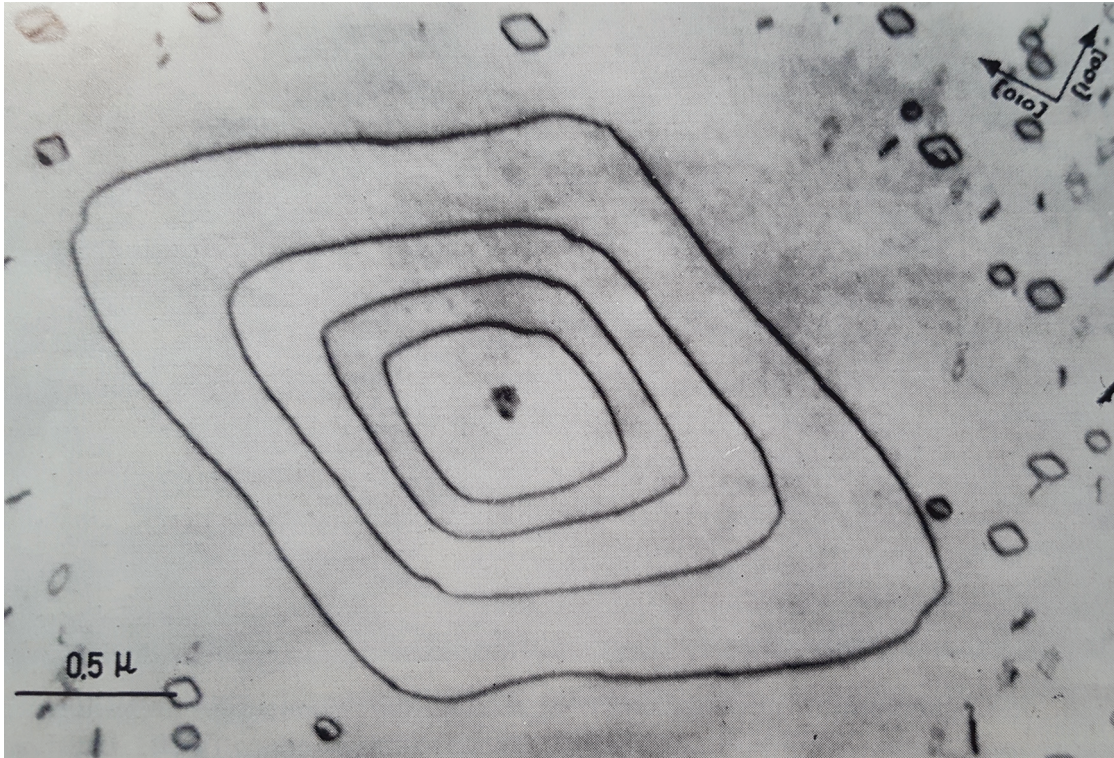


Figure 8.2 – An experimental observation of a Frank-Read source and nucleated dislocation loops in an Al-Mg alloy. Figure from [Amelinckx (1964)].

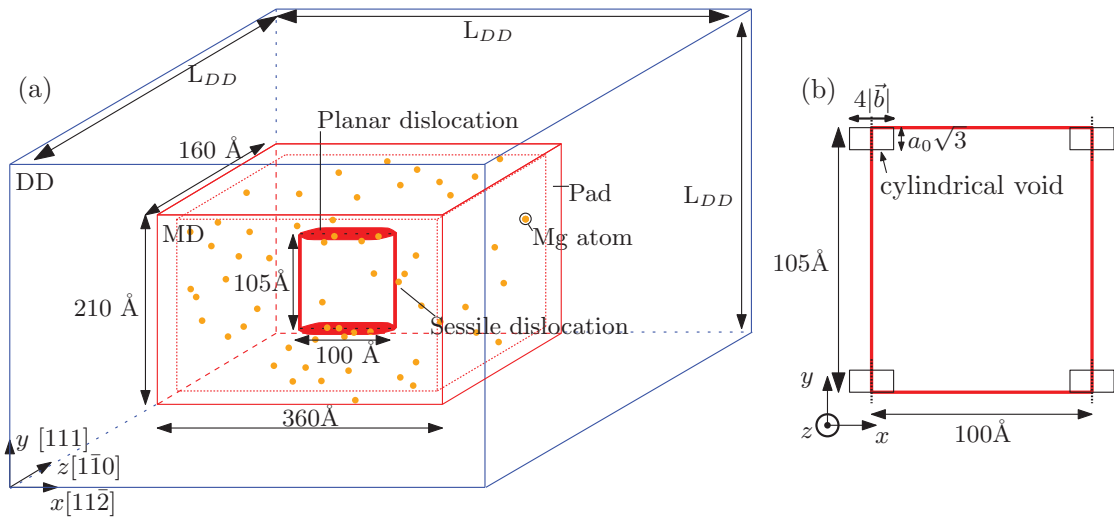


Figure 8.3 – (a) A double Frank-Read source modeling in the CADD3d domain in a perspective view. The MD domain boundary is shown with the red solid lines, and the DDD boundary is indicated in the blue solid lines. The atomistic FR source consists of the two planar dislocations connected with the two sessile dislocations. 5% of the MD atoms are defined as the Mg substitution. (b) At each end of the planar dislocations, a cylindrical void is created to prevent gliding motions of the sessile dislocations.

rectangular layer located in the middle of the MD domain is removed (see Figure 8.3 (b)). It is known that a FR source in a FCC material is not stable [Maurice et al. (2003); Weinberger and Tucker (2012); Shimokawa and Kitada (2014); Xu et al. (2016)]. More precisely, as the planar dislocation expands, the sessile dislocations, which are supposed to remain straight, may glide as well. To maintain the FR source in the chosen slip plane, we introduce two voids at the sides of the rectangle by removing the atoms in two cylinders with radii $R=2|\vec{b}|$ and heights $H=a_0\sqrt{3}$ (a_0 lattice constant) as suggested by Shimokawa and Kitada [Shimokawa and Kitada (2014)]. Finally we relax the MD box to obtain the double FR source, actually made of two planar dislocations connected by two sessile dislocations as shown in Figure 8.3 (a).

Then, we couple the relaxed MD domain with the DDD domain. As shown in Figure 8.3 (a), the pad region is defined to surround the MD box with a thickness of 7\AA . Furthermore, to describe dislocations piling-up against a grain boundary, the mobilities of DDD nodes are set to be zero when they cross the out-most boundary. For the hardening study, three different DDD domains $L_{DD} = \{0.1\mu\text{m}, 0.3\mu\text{m}, 0.5\mu\text{m}\}$ are considered. It is worth to mention that to correctly mimic the grain boundary effect, a free boundary condition should be considered. To support such a boundary condition, image dislocations and their force fields have to be calculated, which are not accounted in the following. For the present problem, we employ a different family of potentials for aluminum and alloy materials. To adapt these potentials for CADD3d, the required building blocks are constructed in the following section.

Core Templates, Peierls Stress and Mobility Law of Dislocations in Al and Al-5%Mg

As discussed in Chapter 7, the core template, mobility law and update step t_{update} have to be adjusted correctly to obtain accurate CADD3d simulation results. Since the first two components depend on the material properties, these can be evaluated in offline MD simulations. In what follows, we employ the Ercolessi-Adams EAM potential [Ercolessi and Adams (1994)] for the pure aluminum and the Liu-Adams EAM potential [Liu and Adams (1998)] for the Al-5%Mg. We have to use the Ercolessi-Adams potential instead of the previously employed Mendelev one [Mendelev et al. (2008)] since there are no alloy potentials available in the literature where Al-Al interactions are computed with Mendelev based forces.

To obtain the core template, dislocation core structures with several character angles are computed similarly to what was described in Chapter 5. However, in the considered alloy the dislocation core structure will depend on the local stress variations induced by the substitutions (Mg). To find core structures for the homogenized alloy, we employ another EAM potential [Varvenne et al. (2016)] which considers the interactions between Al and 5%Mg atoms in an average sense. More precisely, the homogenized potential was purposely built to describe 0K Al-5%Mg material properties (such as cohesive energy and bulk modulus [Noehring and Curtin (2016)]). By following the procedure given in Chapter 5, we obtain dislocation core structures for eight character angles ($\theta = 0^\circ, 19.107^\circ, 30^\circ, 40.893^\circ, 49.107^\circ, 60^\circ, 70.893^\circ$ and

8.3. Core Templates, Peierls Stress and Mobility Law of Dislocations in Al and Al-5%Mg

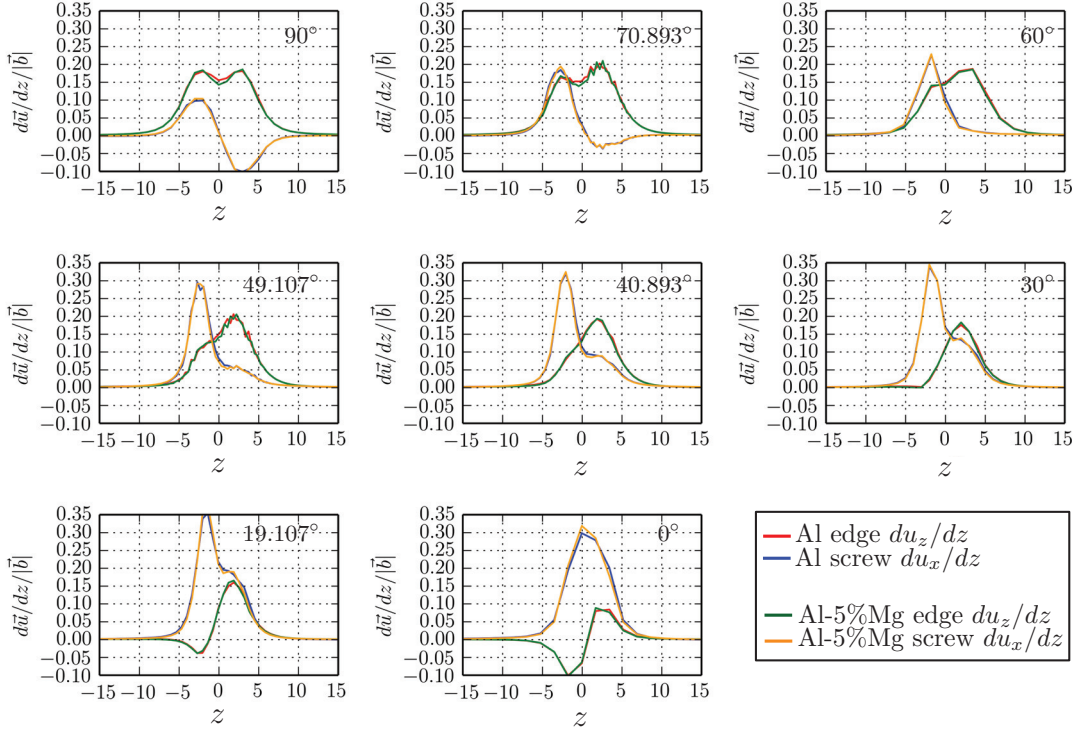


Figure 8.4 – The strains du_z/dz (edge direction), du_x/dz (screw direction) over the gliding direction z . The results derived from the aluminum are shown with the red and blue solid lines, and the calculations obtained from the homogenized alloy are indicated in the green and orange solid lines.

90°). These results are presented in Figure 8.4 with the disregistry functions [Bulatov and Cai (2006); Cho et al. (2015)], where the aluminum is denoted with red and blue solid lines, while the homogenized alloy is denoted with green and yellow solid lines. For each character angle, there are edge and screw components of the displacements because of the dissociation into two (Shockley) partial dislocations [Hirth and Lothe (1992)]. We can observe that these two materials give similar core structures for all the computed character angles with only small (localized) differences. From these calculations, the core templates are generated as was demonstrated in Section 5.6.

Also, Peierls stresses are measured for the considered materials by following the process given in Section 5.5. The obtained results are shown in Figure 8.5. As discussed in Section 5.5, the Peierls stresses vary largely with the character angles, which eventually depend on the core structures. Furthermore, the comparison of the two materials shows that the dislocations in the alloy need higher stresses to glide than in Al.

The second building block is the mobility law. To collect the dislocation mobilities, we carried out a set of MD simulations with the same strategy as depicted in Chapter 6.

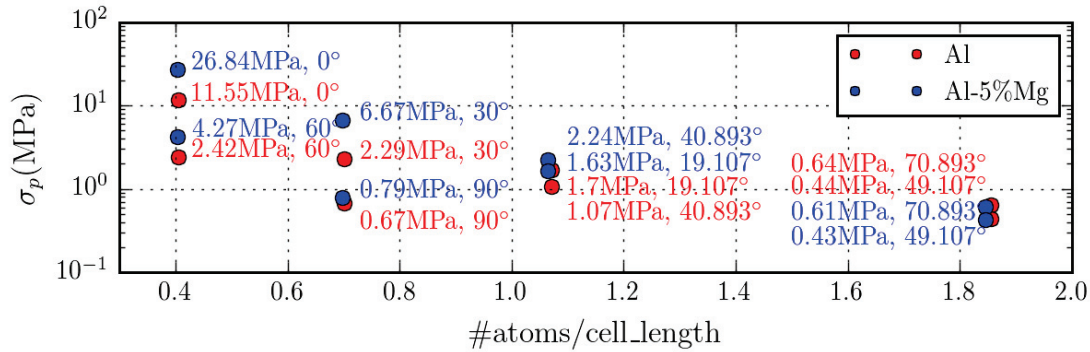


Figure 8.5 – Variations of Peierls stresses for several character angles in Al and Al-5%Mg with respect to the density of atoms in the gliding direction. The corresponding Peierls stress value and the character angle are denoted next to each marker.

We conducted these for several character angles ($0^\circ \leq \theta \leq 90^\circ$) and shear stresses ($50\text{MPa} \leq \sigma \leq 1000\text{MPa}$) with the two material potentials (Al and Al-5%Mg). Those simulations are carried out at around 0K enforced by the Langevin thermostats as described in Chapter 6. To account for distributions of the substitutions, we perform the MD simulations with ten different crystal systems where the magnesium atoms are spread out randomly. The average dislocation mobilities are presented in Figure 8.6 where the blue circles indicate the alloy case, while the red circles denote the mobilities in Al. The alloy case includes the error bar representing the deviations of the obtained mobilities with the ten different crystal systems. Comparing the two materials shows that dislocations in the alloy have lower mobilities at low shear stresses, which reveals higher phonon-based viscous forces. For larger shear stresses, the dislocations mobilities are more alike. The mobility laws are constructed by fitting the Eshelby-Olmsted equation as discussed in Chapter 6. The fitted results are shown with the solid lines in Figure 8.6.

Definition of Pad Domain

The FR source modeled will nucleate several dislocation loops. These will accumulate displacement steps which needs a special treatment for the pad atoms. In order to explain it, let us consider a single FR source instead of the double one. Figure 8.7 (a) shows the evolution of the MD box configuration (from a top view of the slip plane) after two dislocation loops (blue circles) have passed through the pad region. The top and bottom parts of the MD domain are displaced in opposite directions of the Burgers vector \vec{b} by half the Burgers distance each time a dislocation loop escapes from the MD box. Thus, the respective distance is the magnitude of the Burgers vector multiplied by the number of loops n . Accordingly, the pad region will show steps to accommodate for plastic displacements. It is visible that some of the free atoms will be exposed to the DDD domain once the total plastic displacement $n|\vec{b}|$ becomes larger than the pad length. Such atoms are not coupled and will feel influences of the free surfaces.

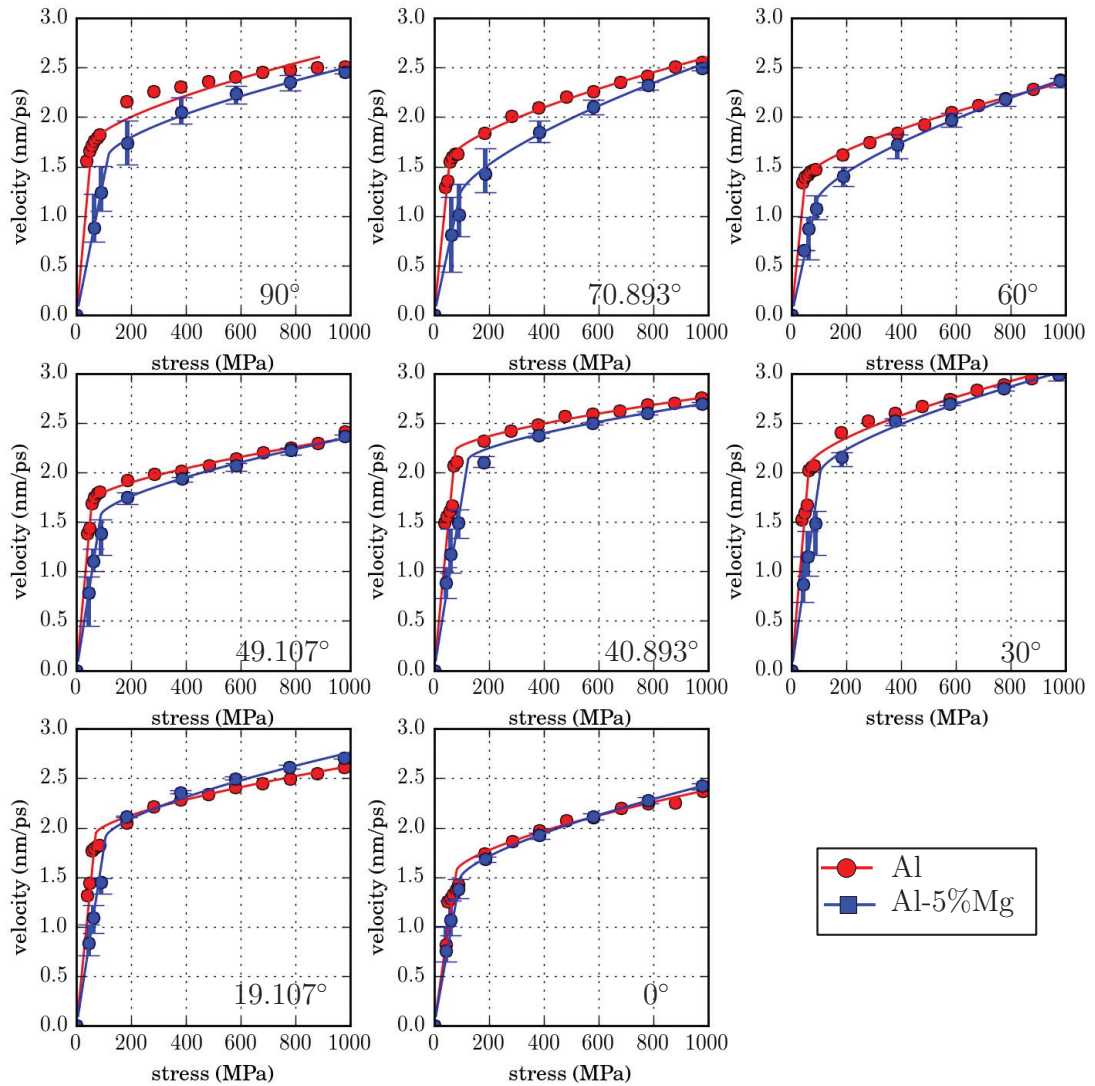


Figure 8.6 – Dislocation mobilities of several character angles in Al and Al-5%Mg. The aluminum results are depicted in the red circle-lines, and the alloy outcomes are shown with the blue lines. Continuous lines are fitted using the Eshelby-Olmsted equation.

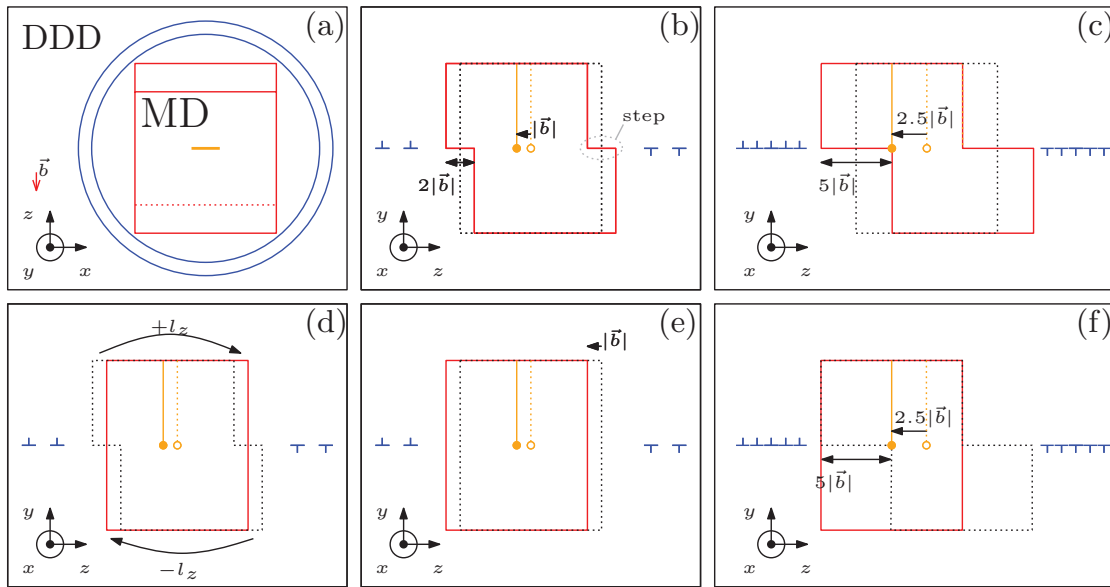


Figure 8.7 – Schematic of the evolution of the MD box during the evolution of a single Frank-Read source. (a) The MD and DDD domains are shown from a top view of the slip plane. The two DDD dislocation loops (blue circles) have been emitted previously from the FR source (orange line) in the MD region. (b) Front view of the MD domain. The step is due to the two dislocation loops that previously crossed the interface. (c) The FR source displaced sufficiently to contact the pad atoms. (d) The atom re-insertion scheme action during the FR source evolution. (e) Re-definition of the MD box to center the FR source. (f) Continuous FR evolution as the result of the (d) re-insertion and (e) re-definition schemes in CADD3d.

To avoid such uncontrolled situation, the pad region has to be updated to include the steps as shown in Figure 8.7 (b). However, even with this update, the FR source cannot maintain a continuous evolution because as shown in Figure 8.7 (c) the FR source will get close and contact with the pad (constrained) atoms.

To maintain a continuous FR source evolution, we have to carefully arrange atoms such that the FR source stays in the MD region without the steps. This scheme can be achieved through the following procedure:

- First, as shown in Figure 8.7 (d), the pad atoms have to be selected according to their current positions in the region surrounding the MD domain (shown with the red solid line).
- Second, the atoms moving out of the MD box must be removed from the simulation box. On the contrary, new atoms should be created at places where the displacement field would otherwise create an empty region.
- Third, as shown in Figure 8.7 (e) the MD atoms and the pad region need to be translated such that the FR source stays at the center of the MD domain.

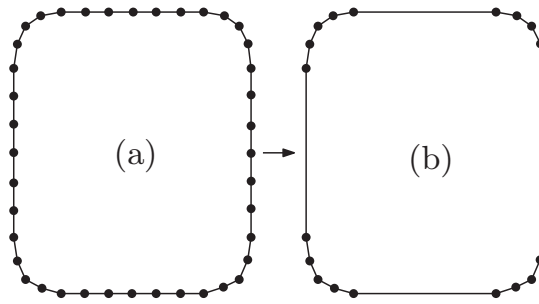


Figure 8.8 – Simplification of the DDD dislocation network. (a) The original dislocation loop. (b) Segments within low curvature regions merged into longer straight segments.

Consequently, as shown in Figure 8.7 (f) a continuous dislocation emission can be realized.

For the present problem, due to the symmetrical MD domain, the second (deleting and creating shown in 8.7 (d)) scheme can be simply achieved by employing the PBC strategy with the pad length, which is thick enough to avoid communications between the two opposite sides. The third scheme (translation shown in Figure 8.7 (e)) must be carried out based on analysis of slip systems and dislocation structures. For the moment, we avoid this last component by employing a MD domain, which is large enough to circumvent the contact of the FR source with the pad atoms.

Dislocation Coarsening

We expect the FR source to emit multiple dislocation loops which eventually will pile-up against the DDD boundary. Then, the computational cost will be mainly demanded for the update of the reciprocal boundary conditions. More precisely, for the CADD3d coupling scheme, we have to evaluate the (linear elasticity) displacements for every pad atoms by considering the entire DDD dislocation network¹, this operation scales with the total number of DDD segments and thus can become expensive.

As shown in Chapter 6, when a dislocation loop travels long distances in Al, an initially curved (ellipsoidal) dislocation loop transforms into an octagon with distinct facets. Such a geometry can be represented, with no loss of information, with only a few straight segments. Figure 8.8 (a) shows such a DDD dislocation loop, and a similar loop with less DDD nodes has been constructed by removing the segments with low curvatures as shown in Figure 8.8 (b). By applying this coarsening strategy, the computational time of the coupling scheme can be significantly reduced.

Consequently, in CADD3d, a coarsening strategy is implemented such that simplified DDD networks are considered when the displacement of the pad atoms need to be computed.

¹MD dislocation structures can also be considered (e.g. core template application) if necessary as described in sub-Section 7.1.1

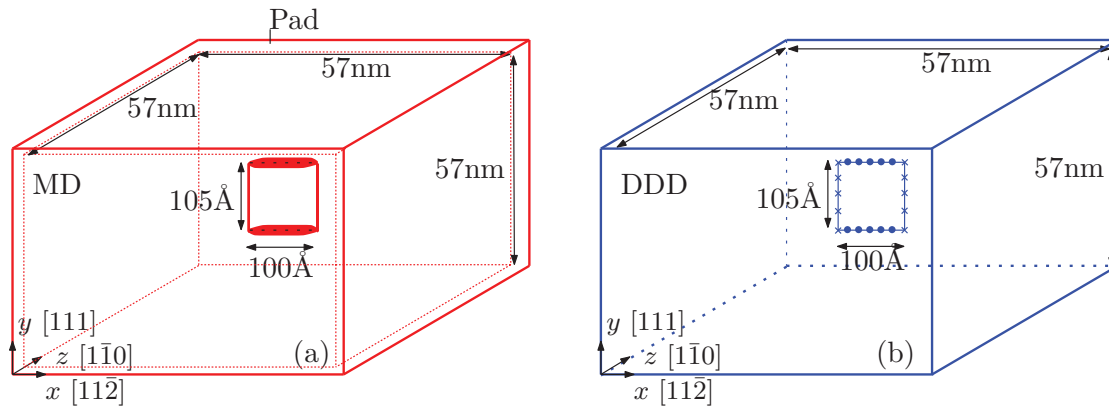


Figure 8.9 – Modeling of a single Frank-Read source with (a) MD and (b) DDD.

The computational efficiency of this strategy will be discussed in Section 8.7.3.

Dislocation Nucleation from Frank-Read Source

In this section, we study the FR source using not only CADD3d but also single scale methods with MD or DDD only. The considered models are shown in Figure 8.9. By comparing these simulation results with each other, a necessity of MD for dislocation nucleation will be highlighted. Such necessity will again confirm the fundamental reason for the development of the CADD3d method.

To compare these simulations with one another, the pure MD simulation needs the same boundary conditions (infinite boundary conditions) to be applied on the DDD or the CADD3d domains. To enforce such boundary conditions, the modified CADD3d scheme can be applied on the boundary of the MD domain as follows: first, we define the constraint atoms in the region surrounding the MD domain (like pad in CADD3d) as shown in Figure 8.9 (a). The positions of those atoms are updated with the displacement field produced by the entire dislocation network (steps ⑥ and ⑦ of CADD3d algorithm). As demonstrated in sub-Section 4.2.3, by removing an insertion zone (MD+DDD), dislocations at the MD boundary will naturally be stopped such that the displacements of the dislocations are effectively constrained. Overall, such method is assumed to be comparable to the impenetrable DDD boundary employed for the other cases.

Let us compare the simulation results calculated under the shear load 700MPa shown in Figure 8.10. For better visibility, only the dislocations in the bottom parts are shown. We can observe the snapshots of the simulations, which are shown from a top view of the slip plane, at 5ps, 10ps, 17.5ps, 20ps, 25.5ps and 50ps. Figure 8.10 (a) shows the pure MD simulation result, and Figure 8.10 (b) denotes the pure DDD result. Figures 8.10 (c) and (d) show the CADD3d simulation results with two different MD domain sizes ($L_{MD} = 160\text{\AA}$ and $L_{MD} = 320\text{\AA}$). Respectively, the MD, and DDD boundaries are shown with the red and blue solid lines, and

atomistic and discrete dislocations are depicted with the red (small) and blue (large) spheres. The results can be summarized as follows:

- By comparing the full MD and the DDD simulation results (Figure 8.10 (a) and (b)), we observe that the MD method emits less dislocations than the DDD method.
- Because the details of the FR source mechanics are considered with the MD region $L_{MD} = 160\text{\AA}$ (Figure 8.10 (a) and (c)), CADD3d allows to emit the correct number of dislocation loops. Furthermore, the global FR source evolution is matching better the pure MD simulation than the pure DDD one.
- The dislocation pile-up widths are different in the pure MD and in the DDD domains. Specifically, the MD dislocations are piled-up with a width of $\sim 25\text{\AA}$, while the DDD dislocations (in CADD3d) are stacked at $\sim 10\text{\AA}$. We believe that this discrepancy occurs because of a mismatch in the calculation of the interaction forces acting on dislocations.

This last point needs to be precised: we speculate that the displacement field calculated by the Barnett's approach is insufficient. Because the anisotropy of Al is low, the isotropy prediction of Barnett et al. [Barnett (1985)] has been employed in every simulations shown in this thesis. However, the results presented on Figure 8.10 call for a more sophisticated anisotropic displacement field. Despite such limitations, we use in the next section the actual CADD3d method to study qualitatively the hardening effects produced by a FR source in an aluminum alloy.

Strain Hardening Effects with Frank-Read Source

A Frank-Read Source in Al-5%Mg Alloy

Like in the previous section, a quasi-static load is applied to generate the FR source evolution. The coupling operations are performed every 50 time steps ($t_{update} = 50\Delta t$).

Figure 8.11 shows snapshots of the FR source evolution ($\sigma = 1000\text{MPa}$ and $L_{DD} = 0.5\mu\text{m}$) at 20ps and 140ps. In Figure 8.11 (a), the MD and DDD domain boundaries are represented by the red and blue solid lines, respectively. The MD atoms and the DDD nodes are colored by their Y coordinates. As expected, we see that multiple DDD dislocation loops are emitted from the FR source, and are piled-up against the DDD boundary. In Figure 8.11 (b), a close-up view of the MD domain is shown, where the magnesium atoms are the blurry gray spheres. Hybrid dislocation loops are attached to the sessile dislocations. As expected, the two sub-parts of the hybrid dislocations are correctly coupled through the coupling interface, and behave as single dislocation structures.

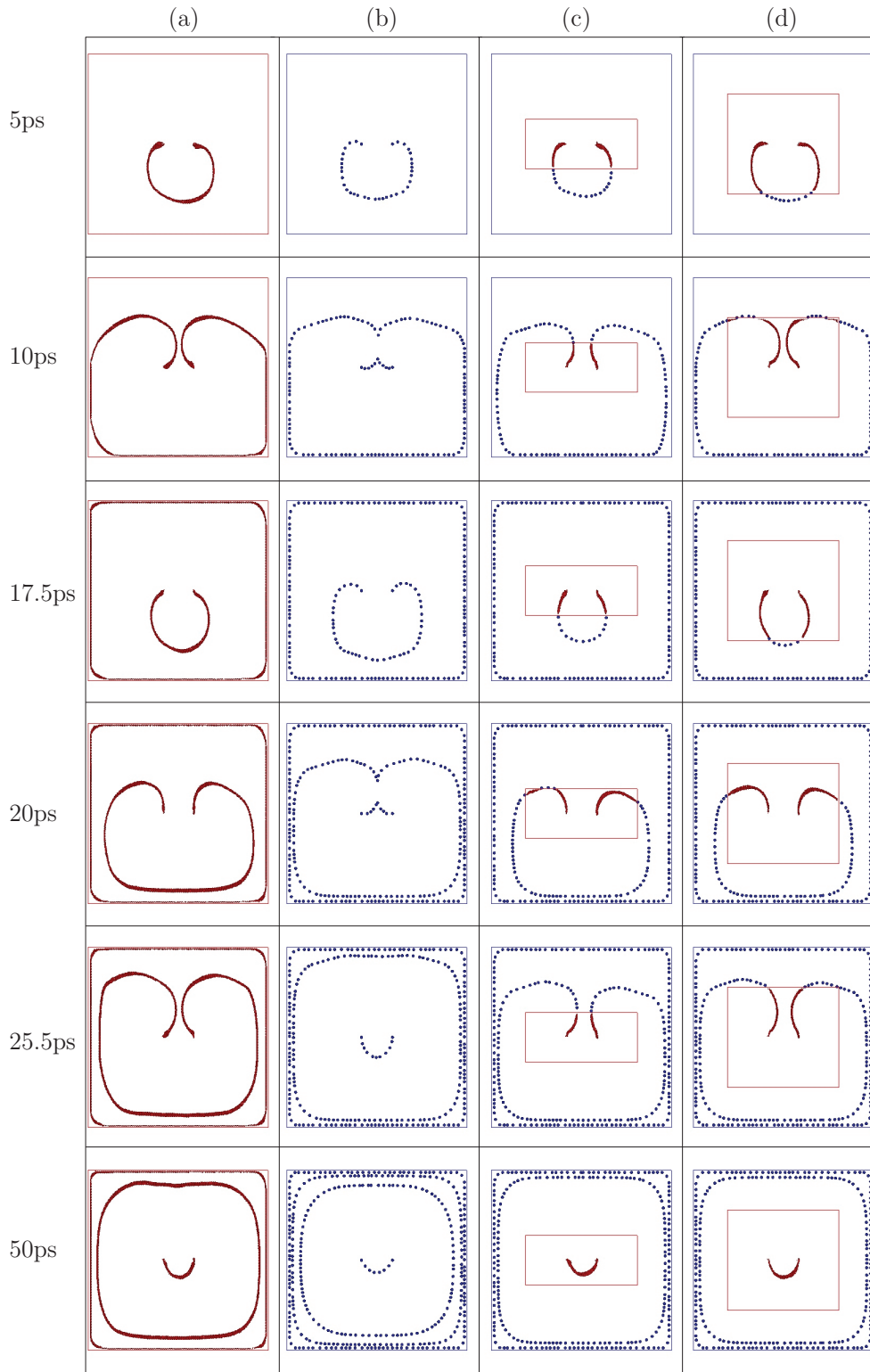


Figure 8.10 – Snapshots of the simulations at 5ps, 10ps, 17.5ps, 20ps, 25.5ps and 50ps. The MD and DDD domain boundaries are shown with the red and blue solid lines, respectively. The MD atoms are depicted by the small red spheres, and the DDD nodes are plotted by the large blue spheres. (a) and (b): single scale MD and DDD simulations, respectively. (c) and (d): the CADD3d coupling simulations with the two different MD-box sizes.

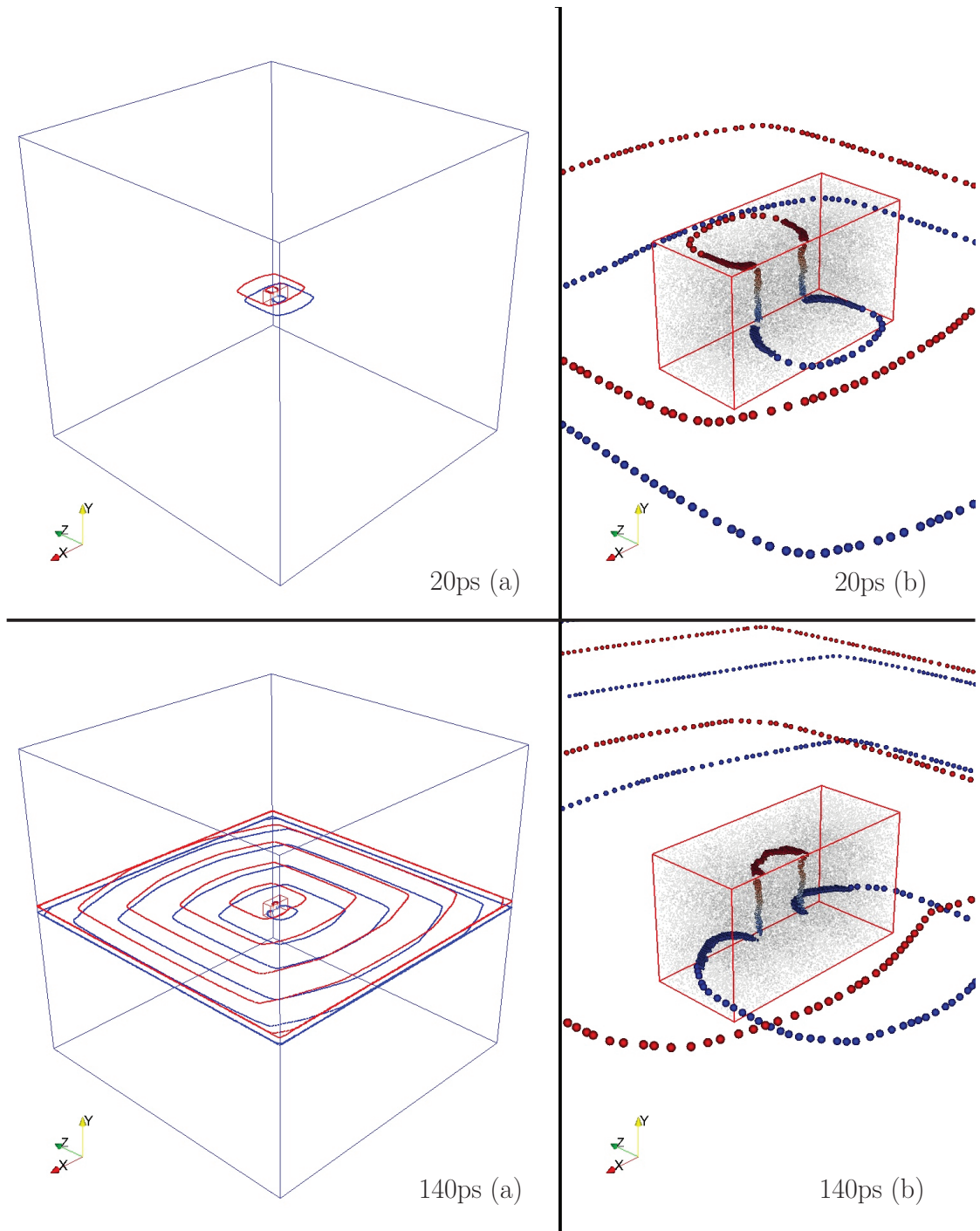


Figure 8.11 – (a) Multiple dislocation loops nucleated from the atomistic FR source are shown with a perspective view. The MD box (red line) is located in the middle and the DDD boundary ($0.5\mu\text{m}$) is shown with the blue lines. (b) A zoom of the MD domain. The MD atoms and DDD nodes are colored by their Y coordinates. The magnesium atoms are shown with small and transparent gray spheres.

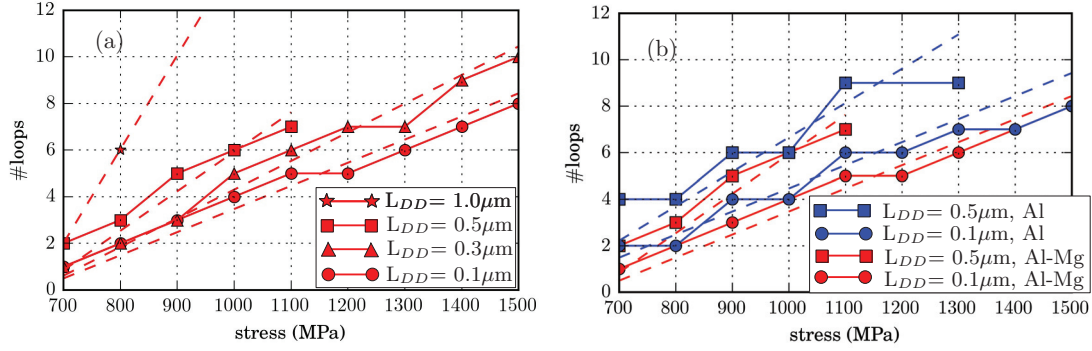


Figure 8.12 – Variations of numbers of the nucleated dislocation loops with different grain sizes and the material types. (a) Grain hardening effect: small grains yield fewer dislocation loops. (b) Solid solution hardening effect: the alloy emits less dislocation loops than for the aluminum.

Hardening Effects

Let us discuss the observed strain hardening effects. As expected, all the CADD3d simulations show that the FR sources cease to nucleate new dislocations when many other dislocation loops are piled-up at the DDD boundaries. The final number of piled-up dislocations for a given applied stress and a grain size is shown in Figure 8.12. We can observe the grain boundary hardening effect in Figure 8.12 (a): for any shear stress, the number of piled-up dislocations decreases if the DDD domain size decreases. In Figure 8.12 (b), we can see the solid solution hardening effect: the FR source in the alloy emits less dislocations than in the aluminum. In fact, some cases yield an odd number of piled-up dislocation loops due to the asymmetrical FR evolution as shown in Figure 8.11 (b) at 140ps. Such a non-asymmetrical evolution occurs because of the imbalance force field acting on the top and bottom FR sources, and this force field is more likely to appear with the substitutions. Therefore, in Figure 8.12 (b) we observe that the FR sources in the alloy yield more odd numbers of the dislocation loops than when in the aluminum.

Recently, Srinath & Curtin [Chakravarthy and Curtin (2010)] proposed an analytic model describing the dislocation piling-up for two dimensional systems. The dislocation density $n(x)$ obtained from this model can be written as follows:

$$n(x) = \begin{cases} \frac{-\sigma_{res}}{i\pi} \sqrt{\frac{(x-x_{0l})(x-x_{0r})}{(x-L_l)(x-L_r)}}, & \text{if } L_l \leq x \leq x_{0l}, x_{0r} \leq x \leq L_r \\ 0, & \text{otherwise} \end{cases} \quad (8.1)$$

with σ_{res} the resolved shear stress applied on the FR-source, x_{0l} and x_{0r} the hardening parameters, L_l and L_r the spatial dimensions of the domain. We used this model to fit the obtained simulation results by changing the hardening parameter $x_0 = x_{0l} = x_{0r}$ with the conditions $L = L_l = L_r$. More precisely, by integrating the density $n(x)$ over half the domain ($L/2$ being one side of the source) with the fitted parameter x_0 , the expected number of emitted disloca-

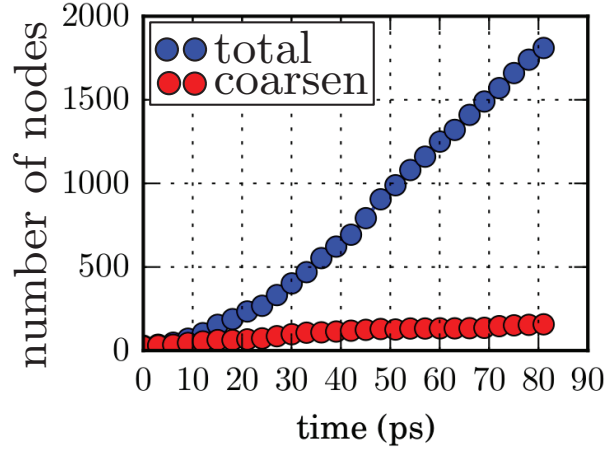


Figure 8.13 – Evolution of a total number of the DDD nodes is shown by the blue circles. The considered DDD points after the coarsening strategy for the coupling is shown with the red circles. In this example, the coarsening strategy reduces the number of the DDD points considered by 88% at most.

tion loops can be calculated. The fitting result is shown with dashed lines in Figure 8.12 for each domain size. We observe that this analytic model can predict the CADD3d simulation results, and finally these observations allow us to claim that the CADD3d method has the potential to evaluate the hardening effects occurring by means of multiple scale interactions. We emphasize that to predict a quantitative hardening effect, the spurious forces (certainly due to the employed isotropic displacement field) will have to be corrected.

Coupling Performances

Figure 8.13 shows the evolution of the number of DDD nodes during the FR source dynamics (shown in Figure 8.11). As the dislocation loop expands, the number of DDD nodes increases significantly. As discussed in Section 8.5, to reduce the expensive coupling computation due to such a large number of DDD nodes, a coarsening strategy needs to be applied. The real number of DDD nodes considered to evaluate the linear elasticity solution is shown with the red circles in Figure 8.13. The proposed coarsening strategy reduces considerably the number of DDD nodes, which are considered during the coupling, and consequently reduces the computational cost of the coupling.

Let us discuss the computational efficiency of the multiscale approach if compared to the single scale MD method. Table 8.1 compares the times for full MD and for CADD3d needed to solve problem discussed in Section 8.6. We find that the number of degrees of freedom (i.e. number of atoms \times 3) is reduced by 84% and 68% by employing CADD3d with the MD domains $L_{MD} = 160\text{\AA}$ and $L_{MD} = 320\text{\AA}$ respectively. The CPU times for such simulations decreased by 80% and 64%, respectively. Therefore, we estimate that 4% of the CPU time is consumed in coupling overhead (communications).

Chapter 8. Frank-Read Source Dynamics in Al and Al-5%Mg

	Full MD	CADD3d ($L_{MD} = 160\text{\AA}$)	CADD3d ($L_{MD} = 320\text{\AA}$)
#D.O.F (million) in MD	13.5	2.19	4.35
CPU time/step (s)	7.8	1.6	2.8

Table 8.1 – Comparison between the full MD and CADD3d performances for the pre-validation problem given in Section 8.6. We only compare the degrees of freedom employed in the MD domains are compared between the full MD and CADD3d simulations. For CADD3d, the averaged CPU time includes all the calculation times (for MD, DDD and CADD3d coupling).

Note that these performance data have been evaluated with the small CADD3d domain ($L = 57\text{nm}$). Therefore, we can expect more significant computational gains if we perform CADD3d simulations with domains larger than $L = 57\text{nm}$. In consequence, the main objective of any multiscale concurrent coupling - being the decrease of the computational cost - is fulfilled by our approach.

Summary

In this chapter, the CADD3d method was employed to study the FR source with the two hardening effects: solid solution and grain boundary strengthening. To that end, the successive generation of the dislocations was enabled by double Frank-Read sources in pure Al and Al-5%Mg. Two coupling components (core templates and mobility law) have been adjusted to this case. Comparably to what was done in Chapter 5, the Peierls stresses have been measured. The pad atoms have been defined carefully with the two strategies (the Eulerian definition and the deleting/creating of the pad atoms) in order to realize the continuous FR source evolution. By comparing the FR sources calculated with the single scale methods (MD and DDD) and CADD3d, we have demonstrated that a correct dislocation nucleation process can be realized even with a small MD sub-domain. Based on those observations and components, we studied two hardening effects with the CADD3d method, and observed qualitative hardening effects: fewer dislocation loops are emitted within an Al-5%Mg alloy or with small grain sizes. Lastly, we could show that the CADD3d method satisfies the main objective of multiscale modeling by significantly decreasing the required CPU time.

9 Concluding Remarks and Outlook

Summary

In this thesis, the author developed, implemented and studied the coupled simulation method for 3d dislocation dynamics at nano- and micro-scales (CADD3d). The challenges of the CADD3d development have been identified by pointing the differences between CADD2d (two-dimensional CADD) and CADD3d features: dislocation networks, which are nucleated from the MD domain, may partly belong to the MD domain, and partially to the DDD domain as they approach the DDD zone. Such hybrid dislocations need to travel seamlessly over the two domains without any spurious forces. To achieve such behaviors, two features were introduced in the CADD3d method. First, when the pure MD dislocation approaches the DDD domain, CADD3d introduces new DDD nodes such that the MD dislocation can be continuously changed into the hybrid dislocations. Second, during the traveling of hybrid dislocations, CADD3d periodically matches the boundary conditions of the MD and DDD descriptions of the hybrid dislocations (i.e. the reciprocal boundary condition). The proposed coupling scheme has been implemented within a parallel computing framework including molecular dynamics (MD) and discrete dislocation dynamics (DDD) engines. Two key components were necessary: 1) the correction of the linear-elasticity displacement field in the regions close to dislocation cores and 2) an accurate mobility law for discrete dislocations, and the both were computed by using offline MD simulations.

For the first component, dislocation core structures were studied by modeling straight dislocations with arbitrary mixed angles in MD. Moreover, a variational Peierls-Nabarro method was extended to include arbitrary dislocation characters to provide secondary model to study these core structures. Both methods showed comparable core structures and stacking fault widths for all the considered mixed dislocations. Additionally, the MD formalism allowed to measure Peierls stresses, showing that the core structure significantly influences the minimum stresses required to initiate the motion of the dislocations. Finally, to utilize the obtained results in CADD3d simulations, the atomistic data have been meshed in order to provide interpolation capabilities. This is the *core template* which is the first building block of CADD3d.

Chapter 9. Concluding Remarks and Outlook

Second, the dislocations mobilities for several temperatures and character angles were studied by employing atomistic simulations. The obtained results were successfully fitted to the Eshelby-Olmsted model, and the fitted constants show good agreements with other published works. To mention an important detail, a critical velocity parameter predicted by the analytic models is correlated to the material dispersive nature. We could revisit the interpretation of this critical velocity by considering character angles that were not studied previously. Finally, the obtained mobility curves were condensed in an angle-and-temperature-dependent mobility law usable by a DDD engine, which forms the second building block of CADD3d.

To validate the CADD3d method, various hybrid dislocation dynamics problems have been studied. The first one considered is a hybrid straight dislocation with an arbitrary character angle. Under a wide range of shear stresses, the two representations in the hybrid dislocation are shown to travel as one single straight dislocation. The sensitivity of the coupling scheme has been studied with respect to the core template, to the mobility law and to the update frequency. The results showed that these components have to be adjusted correctly to allow consistent coupling results. The second test problem is an expansion of hybrid dislocation loop with a finite shear loading. The curved geometry of the dislocation is treated well, and the correct dynamics have been achieved such that the MD and DDD sub-parts of the hybrid dislocation loop expand as one single object. Furthermore, we have studied the coupling problem where multiple dislocation loops interact through the coupling interface. Again, a consistent dislocation dynamics evolution was demonstrated. Lastly, by studying the contraction of a hybrid dislocation loop with a small shear load, the limits of application of the CADD3d coupling scheme could be analyzed.

Finally, the dynamical evolution of a Frank-Read source in a pure/alloy aluminum crystal was studied with CADD3d. Strain hardening effects, which require a multiscale approach at nano- to micro-scales, have been qualitatively simulated. Again we had to prepare the two main building components (core templates and mobility law) for aluminum and aluminum-5% magnesium materials with offline MD runs. Compared to the pure aluminum, random distribution of the alloy atoms should be taken into account when dislocation core structures, stacking fault widths and dislocation mobilities are measured. The Frank-Read source evolution was calculated by using not only CADD3d but also single scale methods (MD or DDD) with the aim to identify the net effect of the coupling. The comparison of these simulations highlighted that an atomistic representation is necessary to get an accurate Frank-Read source evolution. This confirms the need of the MD system for studying dislocation nucleation. When compared to the full MD-single-scaled calculation, the CADD3d produces the similar result with the CPU time significantly reduced. Based on these two observations, finally the CADD3d method showed two hardening effects: fewer dislocation loops are emitted within the alloy or with smaller grain sizes (solid solution hardening and grain boundary strengthening).

Outlook

CADD3d method has been developed in this thesis. While the available tool has been successfully applied on a plasticity problem, several simplifications of the models or of the set-up were necessary. These simplifications call for improvements of the existing tool, which in turn open the path for more complex material plasticity problems and new advances in material engineering.

The first improvement would be to introduce a more sophisticated anisotropic displacement field [Hirth and Lothe (1992); Emmanuel (2009); Shishvan and Van der Giessen (2013)]. In Chapter 8, we observed ghost force effects due to the insufficiently accurate displacement field created by the dislocation segments, and which was applied on the coupling interface. This improvement will solve the ghost force effects as well as it will open a new development of CADD3d towards dislocation dynamics for BCC materials.

In the current version of CADD3d, only one MD domain is employed. In this framework, several limitations regarding the modeling of dislocation-nucleation sources exist. For example, dislocation sources should be concentrically located in one single MD domain. As such, problems where several dislocation sources are randomly distributed cannot be studied. Another limitation is that only dislocation-nucleation sources of small size can be considered. For example, in Chapter 8, we have modeled the $10\text{nm} \times 10\text{nm}$ Frank-Read source. This is a rather quite small FR source when compared to experimentally observed ones ($10\text{nm} \sim 10\mu\text{m}$ [Geipel and Banhart (1996); Amelinckx (1964)]). Due to its small size, we consequently had to apply a high shear stresses ($\sim 800\text{MPa}$ at the minimum) to nucleate dislocation loops. However, in real materials, such high stresses cannot be sustained because other plasticity mechanisms would play a role, such as grain boundary sliding [Schiotz et al. (1998); Jang and Greer (2011)], at lower stresses than 800MPa .

To resolve such limitations, multiple MD domains should be employed in CADD3d. For example, Figure 9.1 shows the modeling of a Frank-Read source, which is made larger while preserving the number of degrees of freedom. The MD domains are used around the sessile dislocations, where an atomistic representation is required according to the discussion given in Section 8.6. In this framework, the length between the sessile dislocations L_{FR} can be chosen large such that small critical shear stresses are expected. It will allow to study the FR source evolution with shear stresses comparable to experimental conditions.

In view of more long-term goal, the implementation of the coupling between the DDD and FEA domains [Weinberger and Cai (2007); Fivel and Depres (2014)] is the next development step. The full version of CADD3d shown in Figure 4.3 can tackle material plasticity problems for which complex boundary conditions should be accounted, such as nano-indentations and compression of nano-pillars. According to [Weinberger and Cai (2007); Weinberger et al. (2009)], the DDD+FEM coupling scheme becomes computationally demanding as the DDD domain contains a large number of degrees of freedom. Therefore, a generic implementation including all the three coupling pieces as well as an efficient parallel computing environment

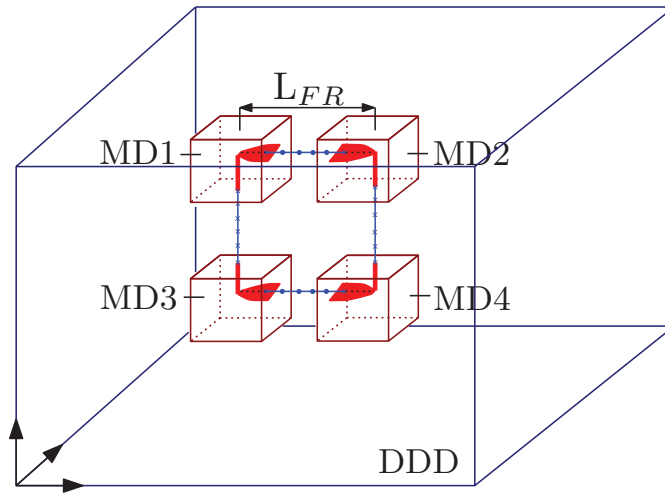


Figure 9.1 – Modeling of a double Frank-Read source with multiple MD sub-domains in CADD3d.

have to be realized.

Final Remark

This thesis developed and validated a novel multiscale method for 3d dislocation dynamics in FCC aluminum at nano- and micro-scales by coupling molecular dynamics and discrete dislocation dynamics. This method requires to know precisely the atomistic core structures and the mobility laws, which were obtained from offline MD simulations. Finally, this method showed qualitatively several strain hardening effects occurring at the nano- and micro-scales, which could not be studied previously with single scale methods.

Bibliography

- Akantu. An opensource object-oriented finite element library, 2007. URL <http://lsms.epfl.ch/akantu>.
- S Amelinckx. *The Direct Observation of Dislocations*. Number v. 6 in Solid state physics: Supplement. Academic Press, 1964. URL <https://books.google.ch/books?id=mOQ9AQAAIAAJ>.
- G Anciaux. *Simulation multi-échelles des solides par une approche couplée dynamique moléculaire/éléments finis. De la modélisation à la simulation haute performance*. PhD thesis, Université Sciences et Technologies - Bordeaux I, July 2007. URL <http://tel.archives-ouvertes.fr/tel-00263816>.
- G Anciaux, O Coulaud, and J Roman. High performance multiscale simulation of crack propagation. *2006 International Conference on Parallel Processing Workshops*, 00(undefin): 473–480, 2006. doi: [doi.ieeecomputersociety.org/10.1109/ICPPW.2006.39](https://doi.org/10.1109/ICPPW.2006.39).
- G Anciaux, SB Ramisetti, and JF Molinari. A finite temperature bridging domain method for MD-FE coupling and application to a contact problem. *Computer Methods in Applied Mechanics and Engineering*, 205–208:204–212, January 2012. ISSN 0045-7825. doi: [10.1016/j.cma.2011.01.012](https://doi.org/10.1016/j.cma.2011.01.012). URL <http://www.sciencedirect.com/science/article/pii/S0045782511000132>.
- J Angelo, N Moody, and M Baskes. Trapping of hydrogen to lattice defects in nickel. *Modelling and Simulation in Materials Science and Engineering*, 3(3):289, 1995. URL <http://stacks.iop.org/0965-0393/3/i=3/a=001>.
- A Arsenlis, W Cai, M Tang, M Rhee, R Opperstrup, G Hommes, TG Pierce, and VV Bulatov. Enabling strain hardening simulations with dislocation dynamics. *Modelling and Simulation in Materials Science and Engineering*, 15(6):553, 2007. URL <http://stacks.iop.org/0965-0393/15/i=6/a=001>.
- E Arzt. Size effects in materials due to microstructural and dimensional constraints: a comparative review. *Acta Materialia*, 46(16):5611 – 5626, 1998. ISSN 1359-6454. doi: [http://dx.doi.org/10.1016/S1359-6454\(98\)00231-6](http://dx.doi.org/10.1016/S1359-6454(98)00231-6). URL <http://www.sciencedirect.com/science/article/pii/S1359645498002316>.

Bibliography

- MF Ashby. The deformation of plastically non-homogeneous materials. *Philosophical Magazine*, 21(170):399–424, 1970. doi: 10.1080/14786437008238426. URL <http://dx.doi.org/10.1080/14786437008238426>.
- W Atkinson and N Cabrera. Motion of a frenkel-kontorowa dislocation in a one-dimensional crystal. *Phys. Rev.*, 138:A763–A766, May 1965. doi: 10.1103/PhysRev.138.A763. URL <http://link.aps.org/doi/10.1103/PhysRev.138.A763>.
- Y Bai, J Wang, D Fang, SS Chakravarthy, and WA Curtin. Mechanics for the world: Proceedings of the 23rd international congress of theoretical and applied mechanics, ic-tam2012 stress gradient plasticity: Concept and applications. *Procedia IUTAM*, 10:453–461, 2014. ISSN 2210-9838. doi: <http://dx.doi.org/10.1016/j.piutam.2014.01.040>. URL <http://www.sciencedirect.com/science/article/pii/S2210983814000418>.
- D Banabic. *Formability of Metallic Materials: Plastic Anisotropy, Formability Testing, Forming Limits*. Engineering Materials. Springer, 2000. ISBN 9783540679066.
- DM Barnett. The displacement field of a triangular dislocation loop. *Philosophical Magazine A*, 51(3):383–387, 1985. doi: 10.1080/01418618508237562. URL <http://dx.doi.org/10.1080/01418618508237562>.
- DM Barnett and RW Balluffi. The displacement field of a triangular dislocation loop - a correction with commentary. *Philosophical Magazine Letters*, 87(12):943–944, 2007. doi: 10.1080/09500830701601748. URL <http://dx.doi.org/10.1080/09500830701601748>.
- N Bhate, RJ Clifton, and R Phillips. Atomistic simulations of the motion of an edge dislocation in aluminum using the embedded atom method. *AIP Conference Proceedings*, 620(1):339–342, 2002. doi: <http://dx.doi.org/10.1063/1.1483548>. URL <http://scitation.aip.org/content/aip/proceeding/aipcp/10.1063/1.1483548>.
- TB Britton, FPE Dunne, and AJ Wilkinson. On the mechanistic basis of deformation at the microscale in hexagonal close-packed metals. *Proceedings of the Royal Society of London A: Mathematical, Physical and Engineering Sciences*, 471(2178), 2015. ISSN 1364-5021. doi: 10.1098/rspa.2014.0881. URL <http://rspa.royalsocietypublishing.org/content/471/2178/20140881>.
- JQ Broughton, FF Abraham, N Bernstein, and E Kaxiras. Concurrent coupling of length scales: Methodology and application. *Physical Review B*, 60(4):2391–2403, July 1999. doi: 10.1103/PhysRevB.60.2391. URL <http://link.aps.org/doi/10.1103/PhysRevB.60.2391>.
- VV Bulatov and W Cai. *Computer Simulations of Dislocations*. Oxford University Press, 2006. ISBN 9780198526148. URL <http://books.google.ch/books?id=4pyWHyZr7esC>.
- VV Bulatov and E Kaxiras. Semidiscrete variational peierls framework for dislocation core properties. *Phys. Rev. Lett.*, 78:4221–4224, Jun 1997. doi: 10.1103/PhysRevLett.78.4221. URL <http://link.aps.org/doi/10.1103/PhysRevLett.78.4221>.

- VV Bulatov, W Cai, J Fier, M Hiratani, G Hommes, T Pierce, M Tang, M Rhee, K Yates, and T Arsenlis. Scalable line dynamics in paradisi. [sc-conference.org/sc2004/schedule/pdfs/pap206.pdf](http://conference.org/sc2004/schedule/pdfs/pap206.pdf).
- JM Burgers. Geometrical considerations concerning the structural irregularities to be assumed in a crystal. *Proceedings of the Physical Society*, 52(1):23, 1940. URL <http://stacks.iop.org/0959-5309/52/i=1/a=304>.
- W Cai. *Atomistic and Mesoscale Modeling of Dislocation Mobility*. PhD thesis, Massachusetts Institute of Technology, 2001.
- W Cai and VV Bulatov. Mobility laws in dislocation dynamics simulations. *Materials Science and Engineering: A*, 387–389(0):277 – 281, 2004. ISSN 0921-5093. doi: 10.1016/j.msea.2003.12.085. URL <http://www.sciencedirect.com/science/article/pii/S0921509304006926>. 13th International Conference on the Strength of Materials.
- W Cai, VV Bulatov, J Chang, J Li, and S Yip. Dislocation core effects on mobility. In F.R.N. Nabarro and J. Hirth, editors, *Dislocations in solids*, volume 12. North-Holland, Amsterdam, 2004.
- W Cai, A Arsenlis, CR Weinberger, and VV Bulatov. A non-singular continuum theory of dislocations. *Journal of Mechanics Physics of Solids*, 54:561–587, March 2006. doi: 10.1016/j.jmps.2005.09.005.
- SS Chakravarty and WA Curtin. Effect of source and obstacle strengths on yield stress: A discrete dislocation study. *Journal of the Mechanics and Physics of Solids*, 58(5):625 – 635, 2010. ISSN 0022-5096. doi: <http://dx.doi.org/10.1016/j.jmps.2010.03.004>. URL <http://www.sciencedirect.com/science/article/pii/S0022509610000529>.
- SS Chakravarty and WA Curtin. Stress-gradient plasticity. *Proceedings of the National Academy of Sciences*, 108(38):15716–15720, 2011. doi: 10.1073/pnas.1107035108. URL <http://www.pnas.org/content/108/38/15716.abstract>.
- J Cho, T Junge, JF Molinari, and G Ancaux. Toward a 3d coupled atomistic and discrete dislocation dynamics simulation: dislocation core structures and peierls stresses with several character angles in fcc aluminum. *Advanced Modeling and Simulation in Engineering Sciences*, 2(1):1–17, 2015. ISSN 2213-7467. doi: 10.1186/s40323-015-0028-6. URL <http://dx.doi.org/10.1186/s40323-015-0028-6>.
- J Cho, JF Molinari, and G Ancaux. Mobility law of dislocations with several character angles and temperatures in FCC Aluminum. *International Journal of Plasticity*, 2016.
- MS Daw, SM Foiles, and MI Baskes. The embedded-atom method: a review of theory and applications. *Materials Science Reports*, 9(7):251 – 310, 1993. ISSN 0920-2307. doi: [http://dx.doi.org/10.1016/0920-2307\(93\)90001-U](http://dx.doi.org/10.1016/0920-2307(93)90001-U). URL <http://www.sciencedirect.com/science/article/pii/092023079390001U>.

Bibliography

- C Denoual. Modeling dislocation by coupling peierls–nabarro and element-free galerkin methods. *Computer Methods in Applied Mechanics and Engineering*, 196(13–16):1915 – 1923, 2007. ISSN 0045-7825. doi: <http://dx.doi.org/10.1016/j.cma.2006.10.007>. URL <http://www.sciencedirect.com/science/article/pii/S0045782506003458>.
- B Devincere and LP Kubin. Simulations of forest interactions and strain hardening in fcc crystals. *Modelling and Simulation in Materials Science and Engineering*, 2(3A):559, 1994. URL <http://stacks.iop.org/0965-0393/2/i=3A/a=010>.
- LM Dupuy, EB Tadmor, RE Miller, and R Phillips. Finite-Temperature Quasicontinuum: Molecular Dynamics without All the Atoms. *Physical Review Letters*, 95(6):060202, August 2005. doi: 10.1103/PhysRevLett.95.060202. URL <http://link.aps.org/doi/10.1103/PhysRevLett.95.060202>.
- C Emmanuel. Elastic energy of a straight dislocation and contribution from core tractions. *Philosophical Magazine*, 89(19):1565–1584, 2009. doi: 10.1080/14786430902976794. URL <http://dx.doi.org/10.1080/14786430902976794>.
- F Ercolessi and JB Adams. Interatomic potentials from first-principles calculations: the force-matching method. *EPL (Europhysics Letters)*, 26(8):583, 1994. URL <http://stacks.iop.org/0295-5075/26/i=8/a=005>.
- JD Eshelby. Supersonic dislocations and dislocations in dispersive media. *Proceedings of the Physical Society. Section B*, 69(10):1013, 1956. URL <http://stacks.iop.org/0370-1301/69/i=10/a=307>.
- AG Evans and JW Hutchinson. A critical assessment of theories of strain gradient plasticity. *Acta Materialia*, 57(5):1675 – 1688, 2009. ISSN 1359-6454. doi: <http://dx.doi.org/10.1016/j.actamat.2008.12.012>. URL <http://www.sciencedirect.com/science/article/pii/S1359645408008732>.
- M Fivel and C Depres. An easy implementation of displacement calculations in 3d discrete dislocation dynamics codes. *Philosophical Magazine*, 94(28):3206–3214, October 2014. ISSN 1478-6435. doi: 10.1080/14786435.2014.949326. URL <http://dx.doi.org/10.1080/14786435.2014.949326>.
- NA Fleck, Muller GM, Ashby MF, and Huchison JW. Strain gradient plasticity: Theory and experiment. *Acta Metallurgica et Materialia*, 42(2):475 – 487, 1994. ISSN 0956-7151. doi: [http://dx.doi.org/10.1016/0956-7151\(94\)90502-9](http://dx.doi.org/10.1016/0956-7151(94)90502-9). URL <http://www.sciencedirect.com/science/article/pii/0956715194905029>.
- N Flytzanis, V Celli, and A Nobile. Motion of two screw dislocations in a lattice. *Journal of Applied Physics*, 45(12):5176–5181, 1974. doi: <http://dx.doi.org/10.1063/1.1663212>. URL <http://scitation.aip.org/content/aip/journal/jap/45/12/10.1063/1.1663212>.
- D Frenkel and B Smit. *Understanding Molecular Simulation*. Academic Press, Inc., Orlando, FL, USA, 2nd edition, 2001. ISBN 0122673514.

- J Frenkel and T Kontorowa. On the theory of plastic deformation and twinning. *Physikalische Zeitschrift der Sowjetunion*, 13:1, 1938. ISSN 1011-0356. URL <http://tinyurl.sfx.mpg.de/u8t6>.
- H Gao, Y Huang, WD Nix, and JW Hutchinson. Mechanism-based strain gradient plasticity i.theory. *Journal of the Mechanics and Physics of Solids*, 47(6):1239 – 1263, 1999. ISSN 0022-5096. doi: [http://dx.doi.org/10.1016/S0022-5096\(98\)00103-3](http://dx.doi.org/10.1016/S0022-5096(98)00103-3). URL <http://www.sciencedirect.com/science/article/pii/S0022509698001033>.
- T Geipel and F Banhart. Temperature-dependence of the frank-read source in si. *Computational Materials Science*, 7(1):181 – 186, 1996. ISSN 0927-0256. doi: [http://dx.doi.org/10.1016/S0927-0256\(96\)00078-X](http://dx.doi.org/10.1016/S0927-0256(96)00078-X). URL <http://www.sciencedirect.com/science/article/pii/S092702569600078X>.
- JA Gorman, DS Wood, and T Vreeland. Mobility of dislocations in aluminum. *Journal of Applied Physics*, 40(2):833–841, 1969. doi: <http://dx.doi.org/10.1063/1.1657472>. URL <http://scitation.aip.org/content/aip/journal/jap/40/2/10.1063/1.1657472>.
- JR Greer and J.Th.M. Hosson. Plasticity in small-sized metallic systems: Intrinsic versus extrinsic size effect. *Progress in Materials Science*, 56(6):654 – 724, 2011. ISSN 0079-6425. doi: <http://dx.doi.org/10.1016/j.pmatsci.2011.01.005>. URL <http://www.sciencedirect.com/science/article/pii/S0079642511000065>. Festschrift Vaclav Vitek.
- JR Greer, CR Weinberger, and W Cai. Comparing the strength of fcc and bcc sub-micrometer pillars: Compression experiments and dislocation dynamics simulations. *Materials Science and Engineering: A*, 493(1–2):21–25, 2008. ISSN 0921-5093. doi: <http://dx.doi.org/10.1016/j.msea.2007.08.093>. URL <http://www.sciencedirect.com/science/article/pii/S0921509307019302>. Mechanical Behavior of Nanostructured Materials, a Symposium Held in Honor of Carl Koch at the TMS Annual Meeting 2007, Orlando, Florida.
- BD Hachmi and G Rateau. The Arlequin method as a flexible engineering design tool. *International Journal for Numerical Methods in Engineering*, 62 (11):1442–1462, 2005. URL <https://hal.archives-ouvertes.fr/hal-00018915>.
- SMH Haghghat, D Terentyev, and R Schaublin. Atomistic simulation of the influence of cr on the mobility of the edge dislocation in fe(cr) alloys. *Journal of Nuclear Materials*, 417(1–3): 1094 – 1097, 2011. ISSN 0022-3115. doi: <http://dx.doi.org/10.1016/j.jnucmat.2011.01.087>. URL <http://www.sciencedirect.com/science/article/pii/S002231151100119X>. Proceedings of ICFRM-14.
- EO Hall. The deformation and ageing of mild steel: Iii discussion of results. *Proceedings of the Physical Society. Section B*, 64(9):747, 1951. URL <http://stacks.iop.org/0370-1301/64/i=9/a=303>.
- J Hartford, BV Sydow, G Wahnstroem, and B Lundqvist. Peierls barriers and stresses for edge dislocations in Pd and Al calculated from first principles. *Phys. Rev. B*, 58:2487–2496, Aug 1998. doi: 10.1103/PhysRevB.58.2487. URL <http://link.aps.org/doi/10.1103/PhysRevB.58.2487>.

Bibliography

- A Hikata, RA Johnson, and C Elbaum. Interaction of dislocations with electrons and with phonons. *Phys. Rev. B*, 4:674–674, Jul 1971. doi: 10.1103/PhysRevB.4.674.4. URL <http://link.aps.org/doi/10.1103/PhysRevB.4.674.4>.
- JP Hirth and J Lothe. *Theory of Dislocations*. Krieger Publishing Company, 1992. ISBN 0894646176. URL http://www.amazon.com/Theory-Dislocations-John-Price-Hirth/dp/0894646176/ref=sr_1_1?s=books&ie=UTF8&qid=1293986464&sr=1-1.
- Y Huang. Mechanism-based strain gradient plasticity—II. Analysis. *Journal of the Mechanics and Physics of Solids*, 48(1):99–128, January 2000. ISSN 00225096. doi: 10.1016/S0022-5096(99)00022-8. URL [http://dx.doi.org/10.1016/S0022-5096\(99\)00022-8](http://dx.doi.org/10.1016/S0022-5096(99)00022-8).
- Y Huang, S Qu, KC Hwang, M Li, and H Gao. A conventional theory of mechanism-based strain gradient plasticity. *International Journal of Plasticity*, 20(4–5):753 – 782, 2004. ISSN 0749-6419. doi: <http://dx.doi.org/10.1016/j.ijplas.2003.08.002>. URL <http://www.sciencedirect.com/science/article/pii/S0749641903001244>.
- TJR Hughes. *The finite element method : linear static and dynamic finite element analysis*. Englewood Cliffs, N.J. Prentice-Hall International, 1987. ISBN 0-13-317025-X. URL <http://opac.inria.fr/record=b1086028>.
- D Hull and DJ Bacon. *Introduction to Dislocations (Fifth Edition)*. Butterworth-Heinemann, Oxford, fifth edition edition, 2011. ISBN 978-0-08-096672-4. doi: <http://dx.doi.org/10.1016/B978-0-08-096672-4.00019-0>. URL <http://www.sciencedirect.com/science/article/pii/B9780080966724000190>.
- A Hunter, IJ Beyerlein, TC Germann, and M Koslowski. Influence of the stacking fault energy surface on partial dislocations in FCC metals with a three-dimensional phase field dislocations dynamics model. *Phys. Rev. B*, 84:144108, Oct 2011. doi: 10.1103/PhysRevB.84.144108. URL <http://link.aps.org/doi/10.1103/PhysRevB.84.144108>.
- A Hunter, RF Zhang, IJ Beyerlein, TC Germann, and M Koslowski. Dependence of equilibrium stacking fault width in FCC metals on the γ -surface. *Modelling and Simulation in Materials Science and Engineering*, 21(2):025015, 2013. URL <http://stacks.iop.org/0965-0393/21/i=2/a=025015>.
- JW Hutchinson. Bounds and self-consistent estimates for creep of polycrystalline materials. *Proceedings of the Royal Society of London A: Mathematical, Physical and Engineering Sciences*, 348(1652):101–127, 1976. ISSN 0080-4630. doi: 10.1098/rspa.1976.0027. URL <http://rspa.royalsocietypublishing.org/content/348/1652/101>.
- S Ishioka. Steady Motion of a Dislocation in a Lattice. *Journal of the Physical Society of Japan*, 34:462, February 1973.
- D Jang and JR Greer. Size-induced weakening and grain boundary-assisted deformation in 60 nm grained ni nanopillars. *Scripta Materialia*, 64(1):77 – 80, 2011. ISSN 1359-6462. doi:

- <http://dx.doi.org/10.1016/j.scriptamat.2010.09.010>. URL <http://www.sciencedirect.com/science/article/pii/S1359646210006184>.
- T Junge. *Modelling Plasticity in Nanoscale Contact*. PhD thesis, ENAC, Lausanne, 2014.
- K Kang, VV Bulatov, and W Cai. Singular orientations and faceted motion of dislocations in body-centered cubic crystals. *Proceedings of the National Academy of Sciences*, 109(38): 15174–15178, 2012. doi: 10.1073/pnas.1206079109. URL <http://www.pnas.org/content/109/38/15174.abstract>.
- CL Kelchner, SJ Plimpton, and JC Hamilton. Dislocation nucleation and defect structure during surface indentation. *Phys. Rev. B*, 58:11085–11088, Nov 1998. doi: 10.1103/PhysRevB.58.11085. URL <http://link.aps.org/doi/10.1103/PhysRevB.58.11085>.
- JY Kim and JR Greer. Tensile and compressive behavior of gold and molybdenum single crystals at the nano-scale. *Acta Materialia*, 57(17):5245 – 5253, 2009. ISSN 1359-6454. doi: <http://dx.doi.org/10.1016/j.actamat.2009.07.027>.
- C Kittel. *Introduction to Solid State Physics*. John Wiley & Sons, Inc., New York, 6th edition, 1986.
- S Kohlhoff, P Gumbsch, and HF Fischmeister. Crack propagation in b.c.c. crystals studied with a combined finite-element and atomistic model. *Philosophical Magazine A*, 64(4):851–878, 1991. ISSN 0141-8610. doi: 10.1080/01418619108213953. URL <http://www.tandfonline.com/doi/abs/10.1080/01418619108213953>.
- S Kok, AJ Beaudoin, DA Tortorelli, and M Lebyodkin. A finite element model for the portevin–le chatelier effect based on polycrystal plasticity. *Modelling and Simulation in Materials Science and Engineering*, 10(6):745, 2002. URL <http://stacks.iop.org/0965-0393/10/i=6/a=309>.
- LP Kubin and G Canova. The modelling of dislocation patterns. *Scripta Metallurgica et Materialia*, 27(8):957 – 962, 1992. ISSN 0956-716X. doi: [http://dx.doi.org/10.1016/0956-716X\(92\)90456-O](http://dx.doi.org/10.1016/0956-716X(92)90456-O). URL <http://www.sciencedirect.com/science/article/pii/0956716X9290456O>.
- AY Kuksin, VV Stegailov, and AV Yanilkin. Molecular-dynamics simulation of edge-dislocation dynamics in aluminum. *Doklady Physics*, 53(6):287–291, 2008. ISSN 1028-3358. doi: 10.1134/S1028335808060013. URL <http://dx.doi.org/10.1134/S1028335808060013>.
- Lammps. A classical molecular dynamics code, 1995. URL <http://lammps.sandia.gov>.
- G Leibfried. Über den einfluß thermisch angeregter schallwellen auf die plastische deformation. *Zeitschrift für Physik*, 127(4):344–356, 1950. ISSN 0044-3328. doi: 10.1007/BF01329831. URL <http://dx.doi.org/10.1007/BF01329831>.
- LibMultiScale. <http://lsms.epfl.ch/libmultiscale>, 2006. URL <http://lsms.epfl.ch/libmultiscale>.

Bibliography

- WK Liu, EG Karpov, and HS Park. *Nano Mechanics and Materials*. John Wiley and Sons, Ltd, 2006. ISBN 9780470034101. doi: 10.1002/0470034106.biblio. URL <http://dx.doi.org/10.1002/0470034106.biblio>.
- XY Liu Liu and JB Adams. Grain-boundary segregation in al–10%mg alloys at hot working temperatures. *Acta Materialia*, 46(10):3467 – 3476, 1998. ISSN 1359-6454. doi: [http://dx.doi.org/10.1016/S1359-6454\(98\)00038-X](http://dx.doi.org/10.1016/S1359-6454(98)00038-X). URL <http://www.sciencedirect.com/science/article/pii/S135964549800038X>.
- BQ Luan, S Hyun, JF Molinari, N Bernstein, and MO Robbins. Multiscale modeling of two-dimensional contacts. *Physical Review E*, 74(4):046710, October 2006. doi: 10.1103/PhysRevE.74.046710. URL <http://link.aps.org/doi/10.1103/PhysRevE.74.046710>.
- J Marian and A Caro. Moving dislocations in disordered alloys: Connecting continuum and discrete models with atomistic simulations. *Phys. Rev. B*, 74:024113, Jul 2006. doi: 10.1103/PhysRevB.74.024113. URL <http://link.aps.org/doi/10.1103/PhysRevB.74.024113>.
- E Martínez and JP Hirth. Screw-dislocation constrictions in face-centered cubic crystals. *Phys. Rev. B*, 90:064102, Aug 2014. doi: 10.1103/PhysRevB.90.064102. URL <http://link.aps.org/doi/10.1103/PhysRevB.90.064102>.
- E Martínez, J Marian, A Arsenlis, M Victoria, and JM Perlado. Atomistically informed dislocation dynamics in FCC crystals. *Journal of the Mechanics and Physics of Solids*, 56(3): 869 – 895, 2008. ISSN 0022-5096. doi: <http://dx.doi.org/10.1016/j.jmps.2007.06.014>. URL <http://www.sciencedirect.com/science/article/pii/S0022509607001408>.
- N Mathew, RC Picu, and M Bloomfield. Concurrent coupling of atomistic and continuum models at finite temperature. *Computer Methods in Applied Mechanics and Engineering*, 200(5–8):765–773, January 2011. ISSN 0045-7825. doi: 10.1016/j.cma.2010.09.018. URL <http://www.sciencedirect.com/science/article/pii/S0045782510002793>.
- de K Maurice, C Wei, and VV Bulatov. Anomalous dislocation multiplication in fcc metals. *Phys. Rev. Lett.*, 91:025503, Jul 2003. doi: 10.1103/PhysRevLett.91.025503. URL <http://link.aps.org/doi/10.1103/PhysRevLett.91.025503>.
- MI Mendeleev, MJ Kramer, CA Becker, and M Asta. Analysis of semi-empirical interatomic potentials appropriate for simulation of crystalline and liquid al and cu. *Philosophical Magazine*, 88(12):1723–1750, 2008. doi: 10.1080/14786430802206482. URL <http://www.tandfonline.com/doi/abs/10.1080/14786430802206482>.
- RE Miller and EB Tadmor. The Quasicontinuum Method: Overview, applications and current directions. *Journal of Computer-Aided Materials Design*, 9(3):203–239, October 2002. ISSN 0928-1045, 1573-4900. doi: 10.1023/A:1026098010127. URL <http://link.springer.com/article/10.1023/A%3A1026098010127>.
- RE Miller, EB Tadmor, R Phillips, and M Ortiz. Quasicontinuum simulation of fracture at the atomic scale. *Modelling and Simulation in Materials Science and Engineering*, 6(5):607,

- September 1998. ISSN 0965-0393. doi: 10.1088/0965-0393/6/5/008. URL <http://iopscience.iop.org/0965-0393/6/5/008>.
- RE Miller, LE Shilkrot, and WA Curtin. A coupled atomistics and discrete dislocation plasticity simulation of nanoindentation into single crystal thin films. *Acta Materialia*, 52(2):271 – 284, 2004. ISSN 1359-6454. doi: <http://dx.doi.org/10.1016/j.actamat.2003.09.011>. URL <http://www.sciencedirect.com/science/article/pii/S135964540300541X>.
- RV Mises. Mechanik der festen körper im plastisch- deformablen zustand. *Nachrichten von der Gesellschaft der Wissenschaften zu Göttingen, Mathematisch-Physikalische Klasse*, 1913: 582–592, 1913. URL <http://eudml.org/doc/58894>.
- Y Mishin, D Farkas, M Mehl, and D Papaconstantopoulos. Interatomic potentials for monoatomic metals from experimental data and *ab initio* calculations. *Phys. Rev. B*, 59: 3393–3407, Feb 1999. doi: 10.1103/PhysRevB.59.3393. URL <http://link.aps.org/doi/10.1103/PhysRevB.59.3393>.
- MPI. A message passing interface, 1993.
- FRN Nabarro. Dislocations in a simple cubic lattice. *Proceedings of the Physical Society*, 59(2): 256, 1947. URL <http://stacks.iop.org/0959-5309/59/i=2/a=309>.
- AHW Ngan. A generalized peierls-nabarro model for nonplanar screw dislocation cores. *Journal of the Mechanics and Physics of Solids*, 45(6):903 – 921, 1997. ISSN 0022-5096. doi: 10.1016/S0022-5096(96)00125-1. URL <http://www.sciencedirect.com/science/article/pii/S0022509696001251>.
- WD Nix and H Gao. Indentation size effects in crystalline materials: A law for strain gradient plasticity. *Journal of the Mechanics and Physics of Solids*, 46(3):411–425, March 1998. ISSN 00225096. doi: 10.1016/s0022-5096(97)00086-0. URL [http://dx.doi.org/10.1016/s0022-5096\(97\)00086-0](http://dx.doi.org/10.1016/s0022-5096(97)00086-0).
- WG Noehring and WA Curtin. Thermodynamic properties of average-atom interatomic potentials for alloys. *Modelling and Simulation in Materials Science and Engineering*, 24(4): 045017, 2016. URL <http://stacks.iop.org/0965-0393/24/i=4/a=045017>.
- JF Nye. Some geometrical relations in dislocated crystals. *Acta Metallurgica*, 1(2):153 – 162, 1953. ISSN 0001-6160. doi: [http://dx.doi.org/10.1016/0001-6160\(53\)90054-6](http://dx.doi.org/10.1016/0001-6160(53)90054-6). URL <http://www.sciencedirect.com/science/article/pii/0001616053900546>.
- D Oh and R Johnson. Simple embedded atom method model for FCC and HCP metals. *Journal of Materials Research*, 3:471–478, 6 1988. ISSN 2044-5326. doi: 10.1557/JMR.1988.0471. URL http://journals.cambridge.org/article_S0884291400002697.
- D Olmsted, K Hardikar, and R Phillips. Lattice resistance and Peierls stress in finite size atomistic dislocation simulations. *Modelling and Simulation in Materials Science and Engineering*, 9(3):215, 2001. URL <http://stacks.iop.org/0965-0393/9/i=3/a=308>.

Bibliography

- D Olmsted, GH Louis, WA Curtin, and RH Clifton. Atomistic simulation of dislocation mobility in Al,Ni and Al/Mg alloys. *Modeling And Simulation in Materials Science and Engineering*, 13(3):371–388, 2005. doi: 10.10088/0965-0393/13/3/007.
- J Pan and JR Rice. Rate sensitivity of plastic flow and implications for yieldsurface vertices. *Int. J. Solids Structures*, pages 973–987, 1983.
- ParaDiS. A large scale dislocation dynamics simulation code, 2007. URL <http://paradis.stanford.edu/>.
- M Peach and JS Köhler. The Forces Exerted on Dislocations and the Stress Fields Produced by Them. *Physical Review*, 80:436–439, November 1950. doi: 10.1103/PhysRev.80.436.
- D Peirce, RJ Asaro, and A Needleman. An analysis of nonuniform and localized deformation in ductile single crystals. *Acta Metallurgica*, 30(6):1087 – 1119, 1982. ISSN 0001-6160. doi: [http://dx.doi.org/10.1016/0001-6160\(82\)90005-0](http://dx.doi.org/10.1016/0001-6160(82)90005-0). URL <http://www.sciencedirect.com/science/article/pii/0001616082900050>.
- S Plimpton. Fast parallel algorithms for short-range molecular dynamics. *Journal of Computational Physics*, 117(1):1 – 19, 1995. ISSN 0021-9991. doi: <http://dx.doi.org/10.1006/jcph.1995.1039>. URL <http://www.sciencedirect.com/science/article/pii/S002199918571039X>.
- FP Preparata and MI Shamos. *Computational Geometry - An Introduction*. Texts and Monographs in Computer Science. Springer, 1985. ISBN 978-1-4612-1098-6.
- SB Ramisetti, G Ancaux, and JF Molinari. Spatial filters for bridging molecular dynamics with finite elements at finite temperatures. *Computer Methods in Applied Mechanics and Engineering*, 253:28–38, January 2013. ISSN 0045-7825. doi: 10.1016/j.cma.2012.09.008. URL <http://www.sciencedirect.com/science/article/pii/S0045782512002903>.
- SB Ramisetti, G Ancaux, and JF Molinari. A concurrent atomistic and continuum coupling method with applications to thermo-mechanical problems. *International Journal for Numerical Methods in Engineering*, 97(10):707–738, 2014. ISSN 1097-0207. doi: 10.1002/nme.4606. URL <http://onlinelibrary.wiley.com/doi/10.1002/nme.4606/abstract>.
- S Ramos de Debiaggi and A Caro. Phonons radiated by moving dislocations in disordered alloys. *J. Phys. France*, 48(9):1499–1504, 1987. doi: 10.1051/jphys:019870048090149900. URL <http://dx.doi.org/10.1051/jphys:019870048090149900>.
- N Richart, G Ancaux, and JF Molinari. An optimized finite-element library akantu. 2010.
- F Roters, P Eisenlohr, L Hantcherli, DD Tjahjanto, TR Bieler, and D Raabe. Overview of constitutive laws, kinematics, homogenization and multiscale methods in crystal plasticity finite-element modeling: Theory, experiments, applications. *Acta Materialia*, 58(4):1152 – 1211, 2010. ISSN 1359-6454. doi: <http://dx.doi.org/10.1016/j.actamat.2009.10.058>.

- F Sansoz and JF Molinari. Mechanical behavior of Σ tilt grain boundaries in nanoscale Cu and Al: A quasicontinuum study. *Acta Materialia*, 53(7):1931–1944, April 2005. ISSN 1359-6454. doi: 10.1016/j.actamat.2005.01.007. URL <http://www.sciencedirect.com/science/article/pii/S1359645405000182>.
- J Schiotz, , DF Tolla, , and KW Jacobsen. Softening of nanocrystalline metals at very small grain sizes. *Nature*, 391(6667):561–563, Feb 1998. ISSN 0028-0836. doi: 10.1038/35328. URL <http://dx.doi.org/10.1038/35328>.
- T Schneider and E Stoll. Molecular-dynamics study of a three-dimensional one-component model for distortive phase transitions. *Phys. Rev. B*, 17:1302–1322, Feb 1978. doi: 10.1103/PhysRevB.17.1302. URL <http://link.aps.org/doi/10.1103/PhysRevB.17.1302>.
- G Schoeck. The core structure and peierls potential of dislocations in Al. *Materials Science and Engineering: A*, 558(0):162 – 169, 2012. ISSN 0921-5093. doi: 10.1016/j.msea.2012.07.106. URL <http://www.sciencedirect.com/science/article/pii/S0921509312010799>.
- J Segurado and J Lorca. Discrete dislocation dynamics analysis of the effect of lattice orientation on void growth in single crystals. *International Journal of Plasticity*, 26(6):806 – 819, 2010. ISSN 0749-6419. doi: <http://dx.doi.org/10.1016/j.ijplas.2009.10.009>. URL <http://www.sciencedirect.com/science/article/pii/S074964190900148X>.
- C Shen and Y Wang. Phase field model of dislocation networks. *Acta Materialia*, 51(9):2595 – 2610, 2003. ISSN 1359-6454. doi: [http://dx.doi.org/10.1016/S1359-6454\(03\)00058-2](http://dx.doi.org/10.1016/S1359-6454(03)00058-2). URL <http://www.sciencedirect.com/science/article/pii/S1359645403000582>.
- C Shen and Y Wang. Incorporation of γ -surface to phase field model of dislocations: simulating dislocation dissociation in fcc crystals. *Acta Materialia*, 52(3):683 – 691, 2004. ISSN 1359-6454. doi: <http://dx.doi.org/10.1016/j.actamat.2003.10.014>. URL <http://www.sciencedirect.com/science/article/pii/S1359645403006207>.
- VB Shenoy, RE Miller, EB Tadmor, R Phillips, and M Ortiz. Quasicontinuum Models of Interfacial Structure and Deformation. *Physical Review Letters*, 80(4):742–745, January 1998. doi: 10.1103/PhysRevLett.80.742. URL <http://link.aps.org/doi/10.1103/PhysRevLett.80.742>.
- VB Shenoy, RE Miller, EB Tadmor, D Rodney, R Phillips, and M Ortiz. An adaptive finite element approach to atomic-scale mechanics—the quasicontinuum method. *Journal of the Mechanics and Physics of Solids*, 47(3):611–642, March 1999. ISSN 0022-5096. doi: 10.1016/S0022-5096(98)00051-9. URL <http://www.sciencedirect.com/science/article/pii/S0022509698000519>.
- VB Shenoy, R Phillips, and EB Tadmor. Nucleation of dislocations beneath a plane strain indenter. *Journal of the Mechanics and Physics of Solids*, 48(4):649–673, April 2000. ISSN 0022-5096. doi: 10.1016/S0022-5096(99)00055-1. URL <http://www.sciencedirect.com/science/article/pii/S0022509699000551>.

Bibliography

- B Shiari, RE Miller, and WA Curtin. Coupled atomistic/discrete dislocation simulations of nanoindentation at finite temperature. *Journal of Engineering Materials and Technology-Transactions of the ASME*, 127(4):358–368, 2005. doi: 10.1115/1.1924561.
- LE Shilkrot, EM Ronald, and WA Curtin. Multiscale plasticity modeling: coupled atomistics and discrete dislocation mechanics. *Journal of the Mechanics and Physics of Solids*, 52(4): 755 – 787, 2004. ISSN 0022-5096. doi: <http://dx.doi.org/10.1016/j.jmps.2003.09.023>. URL <http://www.sciencedirect.com/science/article/pii/S0022509603001625>.
- T Shimokawa and S Kitada. Dislocation multiplication from the frank-read source in atomic models. *Materials Transactions*, 55(1):58–63, 2014. doi: 10.2320/matertrans.MA201319.
- I Shin and EA Carter. Possible origin of the discrepancy in Peierls stresses of FCC metals: First-principles simulations of dislocation mobility in aluminum. *Phys. Rev. B*, 88:064106, Aug 2013. doi: 10.1103/PhysRevB.88.064106. URL <http://link.aps.org/doi/10.1103/PhysRevB.88.064106>.
- SS Shishvan and E. Van der Giessen. Mode I crack analysis in single crystals with anisotropic discrete dislocation plasticity: I. formulation and crack growth. *Modelling and Simulation in Materials Science and Engineering*, 21(6):065006, 2013. URL <http://stacks.iop.org/0965-0393/21/i=6/a=065006>.
- JP Simmons, SI Rao, and DM Dimiduk. Atomistics simulations of structures and properties of $\frac{1}{2}$ (110) dislocations using three different embedded-atom method potentials fit to γ -TiAl. *Philosophical Magazine A*, 75(5):1299–1328, 1997. doi: 10.1080/01418619708209858. URL <http://dx.doi.org/10.1080/01418619708209858>.
- SG Srinivasan, XZ Liao, MI Baskes, RJ McCabe, YH Zhao, and YT Zhu. Compact and dissociated dislocations in aluminum: implications for deformation. *Phys. Rev. Lett.*, 94:125502, Mar 2005. doi: 10.1103/PhysRevLett.94.125502. URL <http://link.aps.org/doi/10.1103/PhysRevLett.94.125502>.
- A Stukowski and K Albe. Extracting dislocations and non-dislocation crystal defects from atomistic simulation data. *Modelling and Simulation in Materials Science and Engineering*, 18(8):085001, 2010. URL <http://stacks.iop.org/0965-0393/18/i=8/a=085001>.
- H Swygenhoven, P Derlet, and A Frøseth. Stacking fault energies and slip in nanocrystalline metals. *Nature Materials*, 3:399, 2004.
- EB Tadmor, M Ortiz, and R Phillips. Quasicontinuum analysis of defects in solids. *Philosophical Magazine A*, 73(6):1529–1563, 1996. ISSN 0141-8610. doi: 10.1080/01418619608243000. URL <http://www.tandfonline.com/doi/abs/10.1080/01418619608243000>.
- EB Tadmor, RE Miller, R Phillips, and M Ortiz. Nanoindentation and incipient plasticity. *Journal of Materials Research*, 14(06):2233–2250, 1999. doi: 10.1557/JMR.1999.0300.

- EB Tadmor, RS Elliott, JP Sethna, RE Miller, and CA Becker. Knowledgebase of Interatomic Models (KIM). <https://openkim.org>, 2011.
- J Till, G Anciaux, and JF Molinari. Dynamic stability of displacement-based atomistic/continuum coupling methods. *Journal of the Mechanics and Physics of Solids*, 80:103–120, July 2015. ISSN 0022-5096. doi: 10.1016/j.jmps.2015.04.004. URL <http://www.sciencedirect.com/science/article/pii/S002250961500071X>.
- E. Van der Giessen and A Needleman. Discrete dislocation plasticity - a simple planar model: a simple planar model. *Modelling and Simulation in Materials Science and Engineering*, 3(5):689 – 735, 1995. ISSN 0965-0393. doi: 10.1088/0965-0393/3/5/008. Journal SEP RW456 Model Simul. Mater. Sci. Eng.
- C Varvenne, A Luque, WG Nöehring, and WA Curtin. Average-atom interatomic potential for random alloys. *Phys. Rev. B*, 93:104201, Mar 2016. doi: 10.1103/PhysRevB.93.104201. URL <http://link.aps.org/doi/10.1103/PhysRevB.93.104201>.
- M Verdier, M Fivel, and I Groma. Mesoscopic scale simulation of dislocation dynamics in fcc metals: Principles and applications. *Modelling and Simulation in Materials Science and Engineering*, 6(6):755, 1998. URL <http://stacks.iop.org/0965-0393/6/i=6/a=007>.
- V Vitek. Intrinsic stacking faults in body-centred cubic crystals. *Philosophical Magazine*, 18(154):773–786, 1968. doi: 10.1080/14786436808227500. URL <http://www.tandfonline.com/doi/abs/10.1080/14786436808227500>.
- A Voter and S Chen. Accurate interatomic potentials for Ni, Al and Ni₃Al. *Proc. MRS Fall Symposium*, 82:175–80, 1987.
- T Vreeland and KM Jassby. Temperature dependent viscous drag in close-packed metals. *Materials Science and Engineering*, 7(2):95 – 102, 1971. ISSN 0025-5416. doi: [http://dx.doi.org/10.1016/0025-5416\(71\)90029-2](http://dx.doi.org/10.1016/0025-5416(71)90029-2). URL <http://www.sciencedirect.com/science/article/pii/0025541671900292>.
- GJ Wagner and WK Liu. Coupling of atomistic and continuum simulations using a bridging scale decomposition. *Journal of Computational Physics*, 190(1):249–274, September 2003. ISSN 0021-9991. doi: 10.1016/S0021-9991(03)00273-0. URL <http://www.sciencedirect.com/science/article/pii/S0021999103002730>.
- GJ Wagner, RE Jones, JA Templeton, and ML Parks. An atomistic-to-continuum coupling method for heat transfer in solids. *Computer Methods in Applied Mechanics and Engineering*, 197(41–42):3351–3365, 2008. ISSN 0045-7825. doi: 10.1016/j.cma.2008.02.004. URL <http://www.sciencedirect.com/science/article/pii/S0045782508000637>.
- J Wang, J Lian, JR Greer, WD Nix, and KS Kim. Size effect in contact compression of nano- and microscale pyramid structures. *Acta Materialia*, 54(15):3973–3982, 9 2006. ISSN 1359-6454. doi: 10.1016/j.actamat.2006.04.030.

Bibliography

- ZQ Wang and IJ Beyerlein. An atomistically-informed dislocation dynamics model for the plastic anisotropy and tension–compression asymmetry of bcc metals. *International Journal of Plasticity*, 27(10):1471 – 1484, 2011. ISSN 0749-6419. doi: <http://dx.doi.org/10.1016/j.ijplas.2010.08.011>. URL <http://www.sciencedirect.com/science/article/pii/S0749641910001166>. Conventional and Emerging Materials.
- CR Weinberger and W Cai. Computing image stress in an elastic cylinder. *Journal of the Mechanics and Physics of Solids*, 55(10):2027 – 2054, 2007. ISSN 0022-5096. doi: <http://dx.doi.org/10.1016/j.jmps.2007.03.007>. URL <http://www.sciencedirect.com/science/article/pii/S0022509607000567>.
- CR Weinberger and GJ Tucker. Atomistic simulations of dislocation pinning points in pure face-centered-cubic nanopillars. *Modelling and Simulation in Materials Science and Engineering*, 20(7):075001, 2012. URL <http://stacks.iop.org/0965-0393/20/i=7/a=075001>.
- CR Weinberger, S Aubry, SW Lee, WD Nix, and W Cai. Modelling dislocations in a free-standing thin film. *Modelling and Simulation in Materials Science and Engineering*, 17(7):075007, 2009. URL <http://stacks.iop.org/0965-0393/17/i=7/a=075007>.
- A Wolfenden. Multi-faulted dislocation loops in electron bombarded aluminium. *Micron* (1969), 4(3):295 – 305, 1972. ISSN 0047-7206. doi: [http://dx.doi.org/10.1016/0047-7206\(72\)90022-2](http://dx.doi.org/10.1016/0047-7206(72)90022-2). URL <http://www.sciencedirect.com/science/article/pii/0047720672900222>.
- S Xiao and W Yang. Temperature-related Cauchy–Born rule for multiscale modeling of crystalline solids. *Computational Materials Science*, 37(3):374–379, September 2006. ISSN 0927-0256. doi: 10.1016/j.commatsci.2005.09.007. URL <http://www.sciencedirect.com/science/article/pii/S0927025605003113>.
- SP Xiao and T Belytschko. A bridging domain method for coupling continua with molecular dynamics. *Computer Methods in Applied Mechanics and Engineering*, 193(17–20):1645–1669, May 2004. ISSN 0045-7825. doi: 10.1016/j.cma.2003.12.053. URL <http://www.sciencedirect.com/science/article/pii/S004578250400026X>.
- S Xu, L Xiong, Y Chen, and McDowell DL. An analysis of key characteristics of the frank-read source process in fcc metals. *Journal of the Mechanics and Physics of Solids*, 96:460 – 476, 2016. ISSN 0022-5096. doi: <http://dx.doi.org/10.1016/j.jmps.2016.08.002>. URL <http://www.sciencedirect.com/science/article/pii/S0022509616301016>.
- N Zaafarani, D Raabe, RN Singh, F Roters, and S Zaefferer. Three-dimensional investigation of the texture and microstructure below a nanoindent in a cu single crystal using 3d ebsd and crystal plasticity finite element simulations. *Acta Materialia*, 54(7):1863 – 1876, 2006. ISSN 1359-6454. doi: <http://dx.doi.org/10.1016/j.actamat.2005.12.014>. URL <http://www.sciencedirect.com/science/article/pii/S1359645406000292>.
- HM Zbib, TD Rubia, M Rhee, and JP Hirth. 3d dislocation dynamics: stress–strain behavior and hardening mechanisms in fcc and bcc metals. *Journal of Nuclear Materials*, 276(1–3):

154 – 165, 2000. ISSN 0022-3115. doi: [http://dx.doi.org/10.1016/S0022-3115\(99\)00175-0](http://dx.doi.org/10.1016/S0022-3115(99)00175-0).
URL <http://www.sciencedirect.com/science/article/pii/S0022311599001750>.

X Zhang, G Lu, and WA Curtin. Multiscale quantum/atomistic coupling using constrained density functional theory. *Phys. Rev. B*, 87:054113, Feb 2013. doi: 10.1103/PhysRevB.87.054113. URL <http://link.aps.org/doi/10.1103/PhysRevB.87.054113>.

J Zimmerman, H Gao, and F Abraham. Generalized stacking fault energies for embedded atom FCC metals. *Modelling and Simulation in Materials Science and Engineering*, 8(2):103, 2000. URL <http://stacks.iop.org/0965-0393/8/i=2/a=302>.

Mr. Jaehyun Cho

École Polytechnique Fédérale de Lausanne EPFL
Swiss Federal Institute of Technology in Lausanne

ENAC-IIC-LSMS (Bâtiment GC A2 504)
Station 18, CH-1015, Lausanne, Switzerland
Phone: +41 78 748 36 45
Email: jaehyun.cho@epfl.ch
Private Email: jaehyun.cho@hotmail.com
Skype ID: ray_cho84

Personal

Born on February 15, 1984

South Korea citizen

Educations

- Title and Period: Ph.D. candidate, 2012 - January, 2017
Program: Mechanics, Ecole Polytechnique Fédérale de Lausanne (EPFL)
Thesis: Coupled 3D dislocation modeling at nano- and micro-scales
- Title and Period: Master of Science, 2010 - 2012
Program: Computational mechanics of materials and structures, University of Stuttgart
Thesis: On the implementation of Isogeometric analysis in PANDAS
Rank and GPA: 3 out of 28 students, 1.5 / 4.0 (1.0 means 'Very Good')
- Title and Period: Bachelor of Engineering, 2002 - 2010
Program: Mechanical and system design engineering, Hongik University
Thesis: Pore closing in a ultra-thick slab by rolling-processes
Rank and GPA: 12 out of 280 students, 3.98 / 4.5 (4.5 means 'Very Good')

Research Assistants

- Period: March, 2017 - February, 2019 (An appointment is made in the title 'Postdoctoral researcher')
Laboratory: Computational Materials Science Group, Lawrence Livermore National Laboratory (LLNL)
Project: *Development of Discrete Dislocation Dynamics Method*
Supervisors: Dr. Robert Rudd (Computational Material Science Group Leader)
- Period: August, 2012 - January, 2017
Laboratory: Laboratory of computational solid mechanics, EPFL
Project: *3D multiscale modeling of dislocations dynamics with atomistic and discrete dislocation dynamics methods*
Supervisors: Dr. Guillaume Ancaux and Dr. Jean-François Molinari
Collaborator: Dr. William Curtin (Laboratory for Multiscale Mechanics Modeling, EPFL)

Period: February-June, 2012
 Laboratory: Virtual orthopedic lab, Orthopedics and motion systems department
 Fraunhofer Institute for Manufacturing Engineering and Automation
 Project: *Development of a graphical user-interface plug-in software in web-browsers*
 Supervisor: Dr. Oliver R"ohrle

 Period: September,2007-August,2009
 Laboratory: Process Design Lab, Hongik University
 Project: *Prediction of pore closings in ultra-thick slab using FEM*
 Supervisor: Dr. Jong-Jin Park

Teaching Assistants during Ph.D. program

Period: September-December of 2013, 2014 and 2015
 Subject: Continuum mechanics (Bachelor semester 3)

 Period: February-June of 2013, 2014 and 2015
 Subject: Numerical modeling of solids and structures (Bachelor semester 4)

 Period: September-December of 2012
 Subject: Linear algebra (Bachelor semester 1)

 Period: February-June of 2014
 Subject: Analysis 1 (Bachelor semester 1)

 Period: September-December of 2013
 Subject: Analysis 2 (Bachelor semester 2)

Publications

Authors: Jaehyun Cho, Till Junge, Jean-François Molinari and Guillaume Ancaux
 Title: *Toward a 3D coupled atomistic and discrete dislocation dynamics simulation: dislocation core structures and Peierls stresses with several character angles in FCC aluminum*
 Journal: *Advanced Modeling and Simulation in Engineering Sciences* (2015)

Authors: Jaehyun Cho, Jean-François Molinari and Guillaume Ancaux
 Title: *Mobility law of dislocations with several character angles and temperatures in FCC aluminum*
 Journal: *International Journal of Plasticity* (2016)

Authors: Jaehyun Cho, Jean-François Molinari, William Curtin and Guillaume Ancaux
 Title: *3d dislocation dynamics with coupled atomistic and discrete dislocation methods (progressing)*

Authors: Guillaume Ancaux, Till Junge, Jaehyun Cho, Max Hodapp, Moseley Philip Arthur, Jean-François Molinari and William Curtin
 Title: *Methodology: 3d coupled atomistic and discrete dislocation dynamics (progressing)*

Authors: Jaehyun Cho, Jean-François Molinari, William Curtin and Guillaume Ancaux
 Title: *Multiscale modeling of Frank-Read source in Al/Al-Mg at nano- and micro-scales (progressing)*

Conferences

- Authors: Jaehyun Cho, Guillaume Anciaux and Jean-François Molinari
Name and Location: European Congress on Computational Methods in Applied Sciences and Engineering 2016, Crete Island, Greece
Topic: Coupled 3D dislocation dynamics at nano- and micro-scales
- Authors: Jaehyun Cho, Guillaume Anciaux and Jean-François Molinari
Name and Location: Platform for Advanced Scientific Computing (PASC) 2016, Lausanne, Switzerland
Topic: Multiscale Modeling of Frank-Read source
- Authors: Jaehyun Cho, Guillaume Anciaux and Jean-François Molinari
Name and Location: Dislocations 2016, Purdue University, U.S.A
Topic: Coupled 3D dislocation dynamics at nano- and micro-scales

Scholarships

- Swiss National Science Foundation: August, 2012- Present (Project funding)
German Academic Exchange Service: April-September, 2010 (Excellent grades)
Hongik University: March-June, September-December, 2004, 2008, 2009, 2010 (Excellent grades)

Computing Skills

- Operating Systems: Linux (Debian-based), OS X, Microsoft Windows
Programming Languages: C and C++, Python, PHP, HTML, CSS, L^AT_EX
Engineering Softwares: MATLAB, MAPLE, ParaView
Analysis Programs: Lammps - molecular dynamics simulation code
ParaDiS - dislocation dynamics simulation code
LibMultiScale - multiscale coupling method from atomistic to continuum scales
PANDAS - FE package for strongly coupled multiphase materials
DEFORM - commercial FE package for metal forming
ANSYS - commercial FE package
CAD Software: CATIA, AutoCAD

Other Skills

- Languages: Korean and English
Personal interests: Drum-playing, Hiking and Snowboarding

20th December 2016, Lausanne
Jaehyun Cho